University of Alberta

OPTIMAL DESIGN OF HYBRID COMPOSITE

FLYWHEEL ROTORS FOR ENERGY STORAGE

by

Mynul Mohammad Shah Ⓒ

A thesis submitted to the Faculty of Graduate Studies and Research

in partial fulfillment of the requirements for the degree of

Master of Science

Department of Mechanical Engineering

Edmonton, Alberta

Fall 2008

ABSTRACT

Energy-storage flywheel rotors are preferably made from high-strength and low-density fiber-reinforced polymer composites. In this study the focus was on utility-grade energy storage flywheels. A 3-dimensional numerical model was developed for hybrid composite flywheel rotors. Employing finite element analysis, stresses induced by rotor rotation were calculated. Numerical results were validated using elasticity theory and data from the technical literature. Design optimization was performed in an effort to maximize energy storage capacity and minimize rotor cost. Material properties, fiber orientations, rotor geometry and angular velocity were parameters considered in the optimization process which aimed at either maximizing specific kinetic energy or kinetic energy per unit cost based on maximum stress failure theory. The primary objective was to reduce radial tensile stresses generated during rotor rotation. Different case studies were performed to demonstrate model capabilities. It was shown that the present approach facilitates the development of efficient and cost-effective flywheel rotors.

ACKNOWLEDGEMENTS

TABLE OF CONTENTS

LIST OF TABLES

LIST OF FIGURES

CHAPTER 1

INTRODUCTION

1.1. Background

Flywheels have been used in potter's wheels and spindle wheel whorls for thousands of years [Gowayed et al., 2002]. The concept of storing energy in a rotating disk dates back to 2400 BCE, the early Bronze Age, when Egyptians used rotating wheels to handcraft pottery [Hellmold, 2001]. During the industrial revolution James Watt contributed to the development of flywheels in steam engines. Another scientist, James Pickard, who was a contemporary to James Watt, developed a solution for transforming reciprocating to rotary motion by combining a crank and a flywheel. However, it was not until the 1970s that flywheels were used as energy storage devices for electrical applications. The energy stored in a flywheel is in the form of kinetic energy, which is proportional to the square of the rotational speed. Flywheel systems for energy storage can be found in certain vehicles (e.g. satellites, automotive); their use in utility-grade application (e.g. for frequency regulation in an electricity grid) is an emerging technology. In all these applications, flywheel rotors typically must rotate at relatively high speeds in order to have sufficient energy storage capacity and become cost-effective.

Over the last couple of decades, high performance flywheels have been developed with significant improvements, showing their potential as an energy storage system in a wide range of applications. With the energy crisis of the 1970s, many governments invested large sums in the development of flywheel energy storage technology, and many research programs began to develop new flywheel devices as alternative energy storage systems [Geneta, 1985]. During that timeframe, flywheels were not only explored and developed for electric vehicles, but also as devices to help electrical utilities manage power demand. Flywheel designs have particularly benefited from the use of advanced composite materials, which offer numerous advantages over metallic alloys, including weight reduction and increased strength. However, even though significant improvements in theoretical concepts and designs have been achieved, to date it remains a challenge to

design flywheel systems that are cost-competitive to other means of energy storage (e.g. batteries).

New approaches to flywheel rotor design were established by the development of high strength materials, in particular fiber-reinforced composites. Fiber reinforced composites are extensively used in many modern engineering applications such as lightweight, strong and rigid aircraft frames, composite drive shafts and suspension components, sports equipment, and pressure vessels. These materials are also used for high-speed flywheels with improved structural performance. The growing use of composite materials is attributed to their inherent ability for customization, enabling them to meet specific design objectives for given applications [Pelletier and Vel, 2006]. These allowed flywheels to reach higher rotational speeds and store more energy per unit mass [Gowayed et al., 2002]. These advancements enabled rotational speeds that make the energy stored in flywheels comparable to that in chemical batteries. Furthermore, composite flywheels represent an attractive alternative to chemical batteries for energy storage due to their comparable specific energy (energy per unit mass) and superior specific power (power per unit mass), charge/discharge behavior, temperature range, and cycle life [Arvin and Bakis, 2006]. Flywheels are also highly efficient and environmentally friendly energy storage systems. Little of the energy stored in a flywheel rotor is lost over time due to friction since modern flywheels are generally held in very low friction environments (i.e. by suspending the rotor in a magnetic field in a vacuum). Efficient mechanical-to-electrical energy conversion is performed through the motor/generator unit. These are driving factors contributing to the resurgence of flywheel technology, in particular for uninterruptible power supplies (UPS) and power conditioning units. The use of flywheels as modern energy storage technology is of great interest to researchers whose aim is to increase rotational speed and thus energy storage capacity. With the advent of advanced composite materials with high strength-to-weight ratios coupled with modern manufacturing techniques such as filament winding, it appears that high-strength filament-wound flywheels can fulfill a variety of energy storage requirements.

1.2. Overview of the Current Research Work / Scope and Organization of the Dissertation

1.2.1. Scope and Significance of Current Research Work

Continued research will further knowledge and understanding about the implementation of fiber reinforced polymer composites (FRPC) in flywheels for the reduction of high radial tensile stresses along the thickness of the flywheel during high speed rotation. It is predicted that improved economics and better understanding of using advanced composite materials in flywheel rotors will lead to increased usage, which will in turn further increase this field of research.

Finite element based design and optimization of composite flywheel rotors has been discussed in the technical literature to some extent. In this research work, design optimization of composite flywheel rotors was performed based on rotational speed, geometry and material composition of a hybrid composite rotor. Finite element analysis was used to calculate stress distributions induced by flywheel rotor rotation. The main thrust of this thesis was to develop a comprehensive approach and methodology to obtain optimized structures for a hybrid composite flywheel rotor. Specific optimal designs for such systems were demonstrated. In particular, the present work constitutes a comprehensive approach by making a numerical model, verifying it through analytical results and related research work, and finally optimizing this model to maximize specific kinetic energy (KE/M) or kinetic energy per unit cost (KE/*Cost*). The latter is considered a novel approach. The present study showed that optimum design using hybrid composite rims can significantly reduce stresses in the rotor, causing stored energy to be much higher than in the case of using each material alone. In addition, an investigation was conducted on the interference-fit or press-fit effect between flywheel rings to promote compressive radial stresses. These residual stresses may improve energy storage capacity during flywheel operation even further. Furthermore, an aluminum hub was incorporated with the rotor to provide a more realistic design and observe the effect on a complete flywheel rotor. From the resultant analysis it was found that although aluminum has generally adequate ultimate strength and elastic modulus, critical stresses may develop in an aluminum hub.

1.2.2. Outline of the Current Study

The present thesis is divided into six chapters that investigate various aspects of designing and optimizing a hybrid composite flywheel rotor.

In chapter 2 a review of the technical literature related to flywheel energy storage systems is given, including the current status of hybrid composite flywheel rotors, the contribution of fiber reinforced polymer composites to flywheel technology, and different test methods.

In Chapter 3, numerical modeling for single isotropic and orthotropic material flywheel rotors and their validation are described. Mathematical relationships for stress, strain, and displacement pertaining to flywheel rotors are presented. A numerical model for a hybrid material flywheel rotor was developed and compared to results presented in Wagner et al. (2007). In addition, the procedure and the effectiveness of using a press-fit or residual thermal stress effect in hybrid composite rims is described. Finally, a hub attached to the hybrid composite flywheel rims was investigated to assess the performance of a complete flywheel rotor.

In Chapter 4 an optimization model was developed for maximizing the performance of flywheel rotors based on equality and inequality constraints using the validated multi-material finite element model. Detailed descriptions of the optimization model for the flywheel rim, as well as the procedure used to solve the optimization problem by finite element analysis are discussed in this chapter.

In Chapter 5 results and discussions of different case studies are presented. Case studies for using different composite materials, applying a press fit effect, or using three material rings instead of two, were analyzed using the optimization routine. Effects of material cost, rim thickness and rotational speed with respect to the optimization process are also discussed in this chapter.

Conclusions and recommendations for future work on hybrid composite flywheel rotors are given in Chapter 6.

CHAPTER 2

LITERATURE REVIEW

Advanced flywheel systems are increasingly gaining attention as energy storage devices due to their attractive properties compared to chemical battery systems, i.e. comparable specific energy and superior specific power, charge/discharge behavior, efficiency, temperature range, and cycle life [Arvin and Bakis, 2006]. Extensive research work has been conducted in the area of composite material flywheel rotors by numerous researchers. To gain insight into this work a literature review was performed preceding the current investigation. The goal of the review was to provide a clear picture of composite flywheel rotor technology, and to identify areas requiring further development. The review was divided into the following subject areas: (1) an overview of flywheel energy storage systems, (2) fiber reinforced polymer composites in flywheel energy storage, (3) design approaches for reducing stresses created by rotor rotation, (4) rotor analysis methods including design optimization, (5) different rotor test methods and (6) material considerations for flywheel rotors.

2.1.   Overview of Flywheel Energy Systems

2.1.1.   Working Principle of Flywheel Energy Storage Systems

A flywheel is an inertial energy storage system in which energy is stored in a rotating mass. Generally speaking, the flywheel rotor is a rotating cylindrical body used as a storage device for kinetic energy. Although flywheels are most commonly used for moderating speed fluctuations in machinery (e.g. engines), it is well known that they can also be used as energy storage systems. By connecting the rotor to a motor/generator unit (see Fig. 2.1) electrical energy can be converted into mechanical energy and thus stored by the flywheel. The motor/generator unit operates as a motor to accelerate the flywheel to store energy, or as a generator to recover the energy stored in the flywheel. Schematics illustrating the primary components and the working principle of a flywheel energy storage system are shown in Figs. 2.1 and 2.2 respectively.
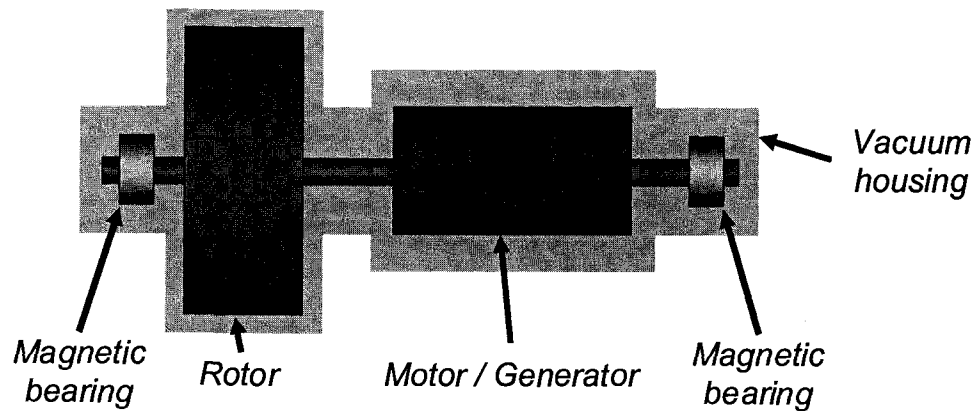
Figure 2.1: Schematic of flywheel energy storage systems.
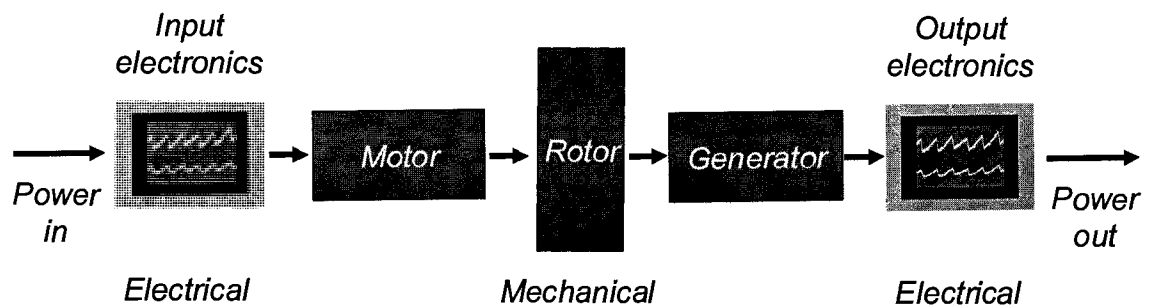
Figure 2.2: Energy flow in a flywheel energy storage system.

A flywheel energy storage system consists of five primary components. These components and their functions are [Pentadyne, 2007, Lazarewicz et al., 2006]:

- **Rotor:** A complete rotor assembly is composed of a hub and rim. The energy is stored by the spinning rotor in the form of kinetic energy. The rim is the main rotating mass of the rotor storing most of the energy. The hub connects the rim to a shaft.

- **Bearings:** The rotating flywheel shaft is supported by mechanical or magnetic bearings, which allow for low resistance to rotor rotation. As bearing friction constitutes energy loss, magnetic bearings are preferred over mechanical ones.

- **Motor/Generator Unit:** Electrical energy supplied to the motor accelerates the rotor, and the generator recovers electrical energy by decelerating the rotor. Torque

associated with rotor acceleration/deceleration is usually transferred between the rotor rim and the motor/generator unit via hub and shaft. Since power input and output events are typically separated in time, the motor and generator are usually combined into a single unit reducing weight and cost of the flywheel system [Hebner et al. 2002].

- **Vacuum Enclosure:** A low pressure environment (vacuum) is maintained by a pressure vessel enclosure which also acts as structural support for the flywheel assembly and bearing system. All rotating components operate inside the vacuum housing to reduce aerodynamic drag. It also serves as a safe containment in case catastrophic rotor failure results in high-energy ballistic debris.

- **Power Electronics:** Power electronics interface the motor/generator unit with the electrical power system. Their purpose is to convert input power into a suitable electrical signal for efficient operation of the motor/generator unit.

2.1.2.   Benefits and Applications of Flywheel Energy Storage

Flywheel energy storage systems, also known as flywheel batteries, have the potential to store significantly more energy per unit of mass than standard chemical batteries. This is important in situations where maximum energy storage is needed in the smallest available mass (e.g. space vehicles). In addition to high specific energy density, flywheel batteries offer other advantages over chemical batteries (see Table 2.1) for various applications including automobiles, satellites and stand-by power systems. In addition, flywheel batteries possess superior specific power. If flywheels are used in conjunction with magnetic bearings and advanced motor/generator systems, more than 90% of the energy stored in them can be retrieved, which constitutes a much better efficiency than conventional chemical batteries where less than 80% of the energy input can be reclaimed [Hebner et al., 2002]. The high energy storage efficiency of flywheel batteries translates into size and weight reductions, which are critical characteristics for vehicular applications.

There are numerous applications for the flywheel energy storage systems:

- **Transportation:** Flywheel systems can replace conventional chemical batteries for mobile applications such as for electric vehicles. For these applications, flywheel power systems offer specific advantages over chemical battery power systems, such as deep discharge capability, the ability to provide high pulses of power and rapid charging, a tolerance to a wide temperature operating range, a longer operational life and less weight [Hebner et al., 2002].

- **Uninterruptible Power Supply:** Flywheel power storage systems are suitable for electrical load leveling applications, such as an uninterruptible power supply. An UPS can be used to smoothly and effectively transition between a main power source and a backup generator when necessary [Hebner et al., 2002].

- **Space Satellites:** Space satellites need energy storage and attitude control. High speed flywheels can manage the energy storage while at the same time providing a gyroscopic effect for attitude control. Since a flywheel system can perform multiple functions, crucial weight reductions for satellites can be achieved [Bitterly (1998), Hebner et al., 2002].

Table 2.1: Comparison between lead-acid and flywheel batteries [Hebner et al., 2002].

	Lead-acid battery	Flywheel battery
Storage mechanism	Chemical	Mechanical
Life (Years in service)	3-5	>20
Technology	Proven	Promising
Temperature range	Limited	Less limited
Environmental concerns	Disposal issues	Slight
Relative size (equivalent power/energy)	Larger	Smallest
Practical time to hold a charge	Years	Hours

2.2. Fiber Reinforced Polymer Composites in Flywheel Energy Storage

2.2.1. Composite Materials

Composites are materials consisting of two or more constitutes [see e.g. Daniel and Ishai, 2006]. They are combined in such a way as to keep their individual physical phases, and neither become soluble in each other nor form a new chemical compound. Their mechanical performance and properties are designed to be superior to those of the constituent materials acting independently. One of the phases, called reinforcement, is usually discontinuous, stiffer, and stronger, whereas the less stiff and weaker phase is continuous and is called matrix. The properties of a composite material depend on the properties of the constituents, their geometry, and the distribution of the phases. Advanced composite materials refer to those composite materials developed and used primarily in the aerospace sector. However, advanced composites are now also increasingly found in industrial applications. Advanced composites usually consist of high performance fibers as reinforcing phases and polymers or metals as matrices. The fibers have high stiffness and strength. However, the key to realizing enhanced properties of fibers is to embed them in a surrounding matrix that acts as a support for the fibers, transfers applied loads to the fibers, and forms useful structural shapes. Examples are composites made from carbon or graphite fiber/epoxy, glass fiber/epoxy, boron fiber/aluminum, boron fiber/titanium, etc.

2.2.2. Composite Flywheels for Energy Storage

The kinetic energy stored in a flywheel rotor increases linearly with mass but quadratically with rotational speed. When a rotor rotates at a high angular speed, considerable centrifugal forces are created. As a result, high tensile stresses are generated in the rotor in the radial and circumferential directions. Both stress components vary along the radius of the rotor.

A relationship between material properties and the kinetic energy storable in a flywheel

rotor can be established as follows. For a fixed axis rotation, the energy stored in a thin rotating ring rotor is:

$$E_{kin} = \frac{1}{2} I \omega^2 \tag{2.1}$$

where I and ω are the rotor's moment of inertia and angular velocity respectively.

For approximating the critical speed of a flywheel rotor the free body diagram shown in Fig.2.3 was considered.
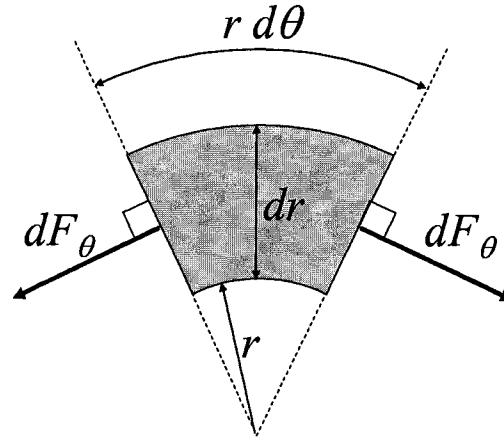
Figure 2.3: Free body diagram of a thin-ring rotating mass element.

Resultant force along the hoop and circumferential directions

$$\xrightarrow{+} \sum F_\theta = dF_\theta \cos\frac{d\theta}{2} - dF_\theta \cos\frac{d\theta}{2} = 0 \tag{2.2}$$

$$+ \uparrow \sum F_r = -2\, dF_\theta \sin\frac{d\theta}{2} = -dm\, a_r \tag{2.3}$$

where ΣF_θ and ΣF_r are force summations in the radial and circumferential directions; dm, $r\, d\theta$ and a_r are the mass, arc length and radial acceleration of the mass element located a radius r, respectively.

From Eq.(2.3) follows:

$$\Rightarrow 2\, dF_\theta \sin\frac{d\theta}{2} = dm\, \frac{V^2}{r} \tag{2.4}$$

with $dm = \rho(r\, d\theta)(dr)(b)$ \hfill (2.5)

where ρ, V and b are the mass element's density, velocity and the width.

Substituting Eq.(2.5) into Eq. (2.4), and noting that $V = r\omega$ and for $\theta \ll 1 \Rightarrow \sin d\theta/2 = d\theta/2$, the following expressions is obtained:

$$dF_\theta = \rho\, dr\, b\, r^2 \omega^2 \qquad (2.6)$$

The tensile stress in the circumferential direction is given by:

$$dF_\theta = \sigma_\theta\, b\, dr \qquad (2.7)$$

Hence, the stress in a thin-ring rotor is:

$$\sigma_\theta = \rho\omega^2 r^2 \qquad (2.8)$$

The maximum speed that a flywheel rotor can achieve is limited by the strength of the material from which it is made. The critical speed of the thin ring rotor can be approximate as:

$$\omega = \sqrt{\frac{\sigma_{ult}}{\rho\, r^2}} \qquad (2.9)$$

where σ_{ult} is the material ultimate strength.

Substituting Eq.(2.9) into Eq.(2.1), the specific energy stored in the rim is found:

$$\frac{E_{kin}}{M} = K\frac{\sigma_{ult}}{\rho} \qquad (2.10)$$

where K is a constant.

From Eq. (2.10), it can be seen that the maximum specific energy stored in the flywheel is only dependent on the specific strength of the material and is no longer related to the rotor mass. Since high specific energy is commonly the dominating design criteria for a flywheel the selection of suitable materials is crucial. Fiber reinforced polymer composites are attractive materials for flywheels because of their high strength and low density [Takahashi et al., 2002]. The use of composite materials in flywheel designs offers numerous advantages over metallic alloys, including reduced weight and increased strength. This is due in part to the high tensile strength of the fiber reinforcement phase.

2.3.   Radial Stress Reduction Techniques for Composite Flywheel Rotors

Due to centrifugal forces high tensile stresses in the radial and circumferential directions are generates during rotor rotation. Stresses are dominant in the circumferential direction during flywheel operation, and hence, composite flywheel rotors are usually filament-wound with fiber reinforcements oriented in that direction. Tensile stresses in the radial direction develop due to mismatch in rotor growth as well as Poisson effects. Since filament-wound composite rotors usually lack reinforcement in the radial direction, rotors are prone to fail by delamination prior to fiber breakage in the circumferential direction [Tzeng et al., 2005]. To maximize kinetic energy, most of researchers involved in flywheel design have focused their attention on reducing radial tensile stresses in rotating flywheel rotors. To reduce radial stresses most researchers suggested using multi-ring structures including rotor rings made from homogeneous materials, filament-wound hybrid materials, polar woven composites, and multiple direction fiber composites. For multi-ring flywheel rotors, the maximum radial stress in each ring is lower during rotation than in single ring rotors [Ranter et al., 2003].

In the case of a single ring rotor that is filament-wound from a singe type of material that is assembled with a metal hub by interference fit, high radial tensile stresses can be mitigated or even eliminated in the rim by maintaining radial compression up to a certain operating speed. Although it is possible to manufacture a thick single rim rotor there are operational disadvantages; not only does radial growth of the rim mismatch that of rotor components such as the hub, but such a design also results in suboptimal energy storage capacity since a large ratio of outside to inside radius causes limited radial tensile strength [Arvin and Bakis, 2006]. A better option is a multi-ring rim design consisting of individual rims of the same material assembled by mechanical press-fit, thermal shrink-fit and pressurized adhesion [Ranter et al., 2003]. If a rotor is assembled in such a manner, a compressive radial stress is generated, which helps to mitigate the development radial tensile stresses during operation. By pre-stressing filament-wound rotor rims, i.e. by inducing residual compressive radial stresses, specific energy and energy density of a flywheel rotor can generally be increased. Another method for inducing compressive

radial stresses in the rotor is to vary fiber strand tensioning during filament winding. In addition, residual thermal stresses induced during manufacturing need be considered during the rotor design process because these stresses can significantly influence radial tensile strength of the composite rotor. To achieve greater reduction of radial tensile stresses or maintenance of radial compressive stresses, multiple rings made from different fibers and/or resin materials can be used. It was shown that rotor performance improved by placing denser and softer materials (which expand easier in radial direction) near the inside radius of the rotor, and stiffer, lighter materials (which experience less radial displacement) on the outer radius of the rotor [Ha and Kim, 1999a].

Arvin and Bakis (2006) suggested another tailoring method called 'ballasting' for reducing radial tensile stresses and achieving a more uniform stress field in the rim. In this method, the allowable outer rotor radius or rotational speed, and in turn energy density are increased by increasing the ratio of circumferential Young's modulus to mass density, E_θ/ρ, from the inside to the outside radius of the flywheel rotor. This can be achieved by tailoring fiber winding angles or the types of fibers with respect to the radial position. If 'ballasting' is performed the low modulus region may even contain only resin with or without dense filler particles. In order to reduce the risk of tensile failure by radial stresses, materials with high strain to failure and reduced radial Young's modulus may be considered. However, the dynamic behavior of such radial compliant rotors is still a subject under investigation.

To eliminate the classical problem of circumferential crack propagation in filament-wound flywheel rotor rims Gowayed et al. (2002) proposed a design that contains reinforcing fibers in the circumferential as well as radial direction, which is termed Multi Direction Composites (MDC). By providing higher radial tensile strength this method allows for increased rotational speed and thus flywheel specific energy. Moreover, instead of a rigid metallic hub the proposed design includes a strain-matching composite box section hub to reduce the danger of cracking in the rim.

Another strategy for improving the speed of composite flywheels is to incorporate compliant elastic or elastomeric interlayers between rings. The aim of this method is to

diminish the transmission of radial stress between filament-wound composite rims, and thus relieve radial stresses [Ha et al., 1999b].

Besides traditional filament winding, rims may be manufactured as so-called polar woven composites to reduce radial and circumferential stresses and increase flywheel energy density [Huang, 1999]. In this method a rim is formed by a circular or spiral weave incorporating fibers in the radial and circumferential directions to balance the radial and circumferential strength of the rim. It is suggested to place a high concentration of radial fibers near the middle of the flywheel disk to withstand the highest spin stresses. The polar woven design was meant to provide high radial stiffness and strength while offering simpler fabrication and assembly than a multi-ring design. Nevertheless, tests exhibited failures in the resin-rich regions that bond layers together, and a potential for matrix cracking due to high stresses caused by fiber kinking. This suggests that further investigation is required regarding long-term effects associated with fiber kinking and layer bonding [Huang, 1999].

2.4. Analysis Method

In order to realistically evaluate various rotor concepts and to adequately define verification tests, accurate analysis methods are necessary. Analysis methods used for flywheel rotor design and verification cover a large part of the reviewed technical literature. Overall, it was observed that finite element analyses and analytical solutions produced equivalent results in terms of rotor stresses, strains, and displacements.

2.4.1. Flywheel Design and Optimization

Although the majority of researchers involved in flywheel design used finite element analysis, some also utilized elasticity theory. Ugural and Fenster (1995) derived expressions for stresses in the radial and circumferential directions and radial displacements of a rotating cylinder from the classical elasticity theory. Although the analysis only included isotropic materials it is indispensable in terms of the initial knowledge for the design of flywheel. Lekhnitskii (1968) provided more extensive work on analytical solutions for the composite rotors. In this work closed form solutions for

radial and circumferential stresses in rotating, single, and multi-ring composite rotors were presented. Arnold et al. (2002) developed an analytical model based on rotation, surface pressure tractions, temperature change, and interfacial misfit to perform elastic stress and displacement analysis for isotropic and anisotropic single and multiple-rim disks. Resulting analyses pointed out key design variables, and elucidated their influence on flywheel disks.

Some researchers also considered time-dependent properties in flywheel rotor design. Time-dependent properties may result in a significant change in stress and strain profiles in a rotating component over a period of time, which is critical in terms of machine performance and durability. An analytical method was developed by Tzeng (2003) for the viscoelastic behavior of a rotating laminated composite cylinder considering ply-by-ply variation of material properties, composite fiber orientations, temperature, and density gradients through the thickness of cylinders. Two concentric, equal thickness cylinders were modeled, i.e. an inner cylinder with a 76 mm (3 inch) inner radius and an outer cylinder with a 114 mm (4.5 inch) inner radius. Both cylinders were hoop-wound and constructed of a graphite/epoxy composite and subjected to a constant rotation of 50,000 RPM over a certain period of time. There was significant creeping with time, which caused radial displacements to increase. Simultaneously, radial stresses were found to decrease significantly due to stress relaxation. But, the viscoelastic response caused an increased hoop stress gradient (i.e. hoop stress decreased at the inner radius and increased at the outer radius). Results from this analytical analysis are significant from a design point of view, implying that creep in composite rotors due to long-term and cyclic loading must be considered. Based on these results, Tzeng (2003) suggested that testing methods must be developed to determine the amount of creep that occurs in actual rotors.

Saleeb et al. (2003) investigated time-dependency and anisotropy of a material on the basis of two specific flywheel designs, including preloading and multi-directional composites (MDC). By focusing on aspects such as geometric constraints, material constraints, loading types, and the fundamental character of the time-dependent response (i.e. reversible and irreversible), Saleeb et al. (2003) ascertained that both preloading and the MDC rotor design are significantly affected by time-dependent material behavior. A

conclusion of this study was that rotor balance may detrimentally be affected eventually reducing the flywheel's operating life.

2.4.1.1. Finite Element Analysis of Composite Flywheel Rotors

Finite element analysis is a computer-based numerical technique for evaluating the behavior of engineering structures. Finite element method (FEM) has widely been used for the calculation of deflections, stresses, strains, vibrations, buckling behaviors, and many other phenomena. It can also be used to study the structural response, progressive fracture, and defect/damage tolerance characteristics of components made from composite materials. The reason for using finite element analysis in composite flywheel modeling is that it allows for determining stress and strains in structures with complex geometrical features or material behavior.

Aziz et al. (2001) conducted two and three-dimensional finite element stress analysis for two flywheel rotor systems with solid and hollow hubs. In this analysis, FEM was complemented with nondestructive evaluation (NDE) for two flywheel rotor assemblies under combined centrifugal and press-fit loadings. Besides obtaining locations of peak radial and hoop stresses within flywheel rotors, radial stress distributions along the rotor's through-thickness direction were determined for several speeds. It was found that with increasing speed the location of peak radial stress moves from the rotor's outer radius towards its center caused by an offset effect between centrifugal load and compressive preloading induced during assembly. In terms of NDE, Computer Tomography (CT) was used to compare analysis and experimental results. CT scans can be used to inspect for delaminations, voids between layers, and resin rich areas [Ranter et al., 2003]. Aziz et al. (2001) determined two-dimensional radial stress distributions through numerical modeling for a rotor with a crack propagating in the circumferential direction. Experimental results showed that first cracking events in the rotor as detected by CT scans could be predicted with FEM provided that the material properties and residual loads were known.

2.4.1.2. Design Optimization for Hybrid Composite Flywheel Rotors

Design optimization is the engineering process that yields greatest part or assembly performance for one or more criteria. Over the past decade a particular focus of design optimization has been on minimizing weight, especially in aerospace applications. However, design optimization may employ wide range of objectives including minimizing cost, time to market, and risk [Pelletier and Vel, 2006]. A growing demand for fiber-reinforced composites in many engineering applications has driven broad research on optimal orientation of the reinforcement phase. Based on a modified generalized plain strain method, Ha et al. (2001) developed an optimization approach for stresses in rotating composite flywheel rotors by varying material properties and residual curing stresses. Through this approach, they found that material sequence and residual stress considerations are crucial for maximizing the total energy stored in a composite flywheel rotor.

Gowayed et al. (2002) performed structural flywheel rotor design analyses accounting for two and three-dimensional features of a multidirectional composite rotor, as well as non-axisymmetric loads. A large number of design parameters related to flywheel operation were involved such as flywheel geometry, material characteristics, material lay-up, and spatial stress distribution and values. Several optimization analyses were carried out. It was found that although FEM-based solutions were computationally more time intensive than closed form non-linear programming, solutions from FEM provided greater accuracy and amount of detail.

Eby et al. (1999) and Arvin and Bakis (2006) among other researchers, optimized flywheel rotors utilizing two advanced techniques for finding optimum solutions, i.e. Simulated Annealing (SA) and Genetic Algorithms (GA). Both techniques are stochastic search techniques that are robust and efficient at finding global optima in large complex search spaces. SA is based on an analogy between the optimization process and the physical annealing process in metals. In the annealing process definite crystalline structures form based on the lowest energy state of the system. This corresponds to the optimization process in which an optimum state if found through the minimum of a design parameter such as cost. In GA an analogy to biological systems is utilized, i.e. a

best solution is found through the combination and recombination of genes (mutations) in biological systems leading to evolution. For optimization problems the same notion can be employed. Through the variation of design parameters from evolution to evolution stage, the overall system will evolve toward a best solution.

2.5.   Test Methods for Composite Flywheel Rotors

There are different types of testing methodologies used to certify flywheel rotors for safe and reliable operation, including coupon testing, fatigue tests, hydro burst and spin testing.

Basic material characteristics of composite materials used in flywheel rotors are usually determined by coupon testing. Such tests are conducted to evaluate composite material behavior under static and cyclic load conditions, including transverse loading, and combined axial compression and torsion loading. Such tests are also suited to investigate composite material behavior for rotor operation in vacuum conditions [Ranter et al., 2003]. Employing hydro burst testing with thin filament-wound composites rings, hoop tensile and fatigue strength and stiffness can be determined [Ranter et al., 2003]. Spin testing plays a significant role in the development of advanced flywheels. The speed range in which a flywheel maintains its structural integrity, and information about failure modes can be obtained, which is essential for the verification of analysis results and design choices [Reddy and Street, 1979]. This test method also facilitates the assessment of radial displacements as well as rotor stability over the speed working range of the flywheel.

2.6.   Materials for Composite Flywheel Rotors

The material class known as fiber composites encompasses a wide variety of material types and forms. When selecting appropriate materials, it is important to focus on aspects pertaining to the fiber and matrix as well as the overall properties of the composite system. Although the fiber reinforcement is the main contributor to the strength of the composite, the choice of matrix material is also an important consideration. Material

selection criteria for composite flywheel rotors should be based on static properties as well as time-dependent properties such as creep and fatigue [Ranter et al., 2003].

The energy density of flywheels is strongly affected by material allowables in the circumferential and radial directions. Thus, for rotor designs, Grudkowski et al. (1995) stated that preference should be given to high strength and low density fibers. For burst and fatigue conditions they indicated that the specific strengths (i.e. strength per density) of materials such as carbon fiber material systems (e.g. T800/epoxy and AS4/epoxy) are highly attractive, especially when compared to S-glass/epoxy systems and metallic materials like steel.

2.7.   Concluding Remarks

A literature review was conducted to introduce the theoretical background of flywheel energy storage systems, and to highlight some related research work. This review pointed out the significance of using fiber reinforced polymeric composites in flywheel rotors. It further showed that radial stress reduction is crucial for obtaining high energy storage in composite flywheels. In addition, to date it still remains a challenge to design FES systems that are cost-competitive to other means of energy storage (e.g. chemical batteries). Despite this, no research work known to the author has dealt with flywheel optimization for minimizing cost or maximizing kinetic energy per unit cost. Comprehending the various approaches for radial stress reduction described in the technical literature was an important step towards the goal of this thesis project which is the development a design tool for maximizing specific kinetic energy and kinetic energy per unit cost in flywheel rotors.

CHAPTER 3

NUMERICAL MODELING OF COMPOSITE FLYWHEEL ROTORS

In this chapter the development and validation of a numerical model for flywheel rotors made from a single isotropic or orthotropic material (see Fig.3.1.1), or hybrid material systems, is described. Preceding model description and validation is a brief review of stress, strain, and displacement relationships applicable to rotor analysis, which underlie latter analytical solutions used to validate the numerical model. Furthermore, the modeling approach is complemented by enabling press-fit assembly for hybrid composite rotors; associated procedures and the effectiveness of a press-fit assembly are discussed accordingly. Finally, a hub was incorporated into the rotor model to investigate the performance of a complete flywheel rotor.
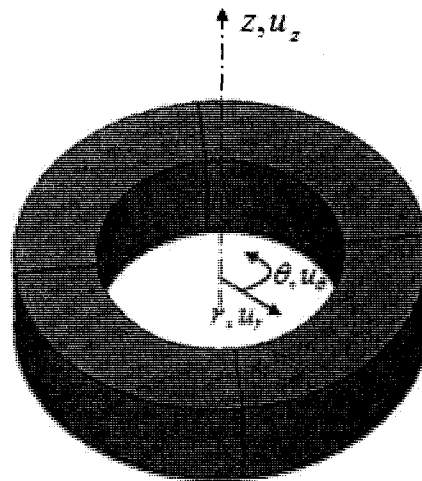
Figure 3.1.1: A typical single material flywheel rotor.

3.1.   Stress-Strain Relations for Rotor Analysis

Stress components and displacements for a stress element in cylindrical coordinates r, θ, z are illustrated in Fig.3.1.2. Corresponding 3-dimensional constitutive stress-strain relationships are given in Eqs.(3.1.1) to (3.1.6), where components of normal and shear

stress are $\sigma_{rr}, \sigma_{\theta\theta}, \sigma_{zz}$ and $\tau_{r\theta}, \tau_{rz}, \tau_{\theta z}$; normal and shear strains are $\varepsilon_{rr}, \varepsilon_{\theta\theta}, \varepsilon_{zz}$ and $\gamma_{\theta z}, \gamma_{rz}, \gamma_{r\theta}$; υ, E, and G are Poisson's ratio, Young's modulus and shear modulus for an isotropic material, respectively.

$$\varepsilon_{rr} = \frac{\sigma_{rr}}{E} - \upsilon\frac{\sigma_{\theta\theta}}{E} - \upsilon\frac{\sigma_{zz}}{E} \qquad (3.1.1)$$

$$\varepsilon_{\theta\theta} = -\upsilon\frac{\sigma_{rr}}{E} + \frac{\sigma_{\theta\theta}}{E} - \upsilon\frac{\sigma_{zz}}{E} \qquad (3.1.2)$$

$$\varepsilon_{zz} = -\upsilon\frac{\sigma_{rr}}{E} - \upsilon\frac{\sigma_{\theta\theta}}{E} + \frac{\sigma_{zz}}{E} \qquad (3.1.3)$$

$$\gamma_{r\theta} = \varepsilon_{r\theta} + \varepsilon_{\theta r} = 2\varepsilon_{r\theta} = \frac{\tau_{r\theta}}{G} = \frac{2(1+\upsilon)\tau_{r\theta}}{E} \qquad (3.1.4)$$

$$\gamma_{rz} = \varepsilon_{rz} + \varepsilon_{zr} = 2\varepsilon_{rz} = \frac{\tau_{rz}}{G} = \frac{2(1+\upsilon)\tau_{rz}}{E} \qquad (3.1.5)$$

$$\gamma_{\theta z} = \varepsilon_{\theta z} + \varepsilon_{z\theta} = 2\varepsilon_{\theta z} = \frac{\tau_{\theta z}}{G} = \frac{2(1+\upsilon)\tau_{\theta z}}{E} \qquad (3.1.6)$$
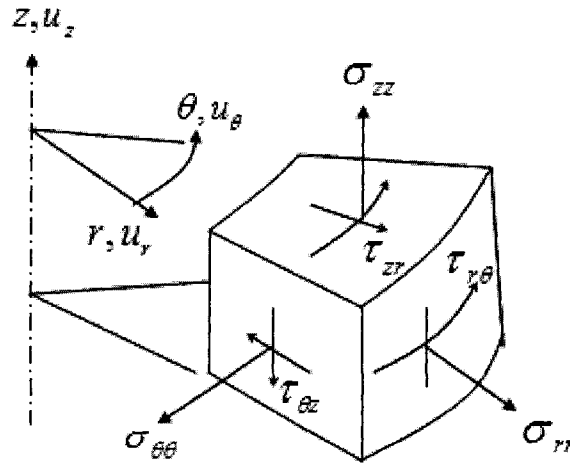
Figure 3.1.2: Stresses and displacements for a stress element in cylindrical coordinates.

Equations (3.1.1) to (3.1.6) are expressed in matrix form as follows:

$$
\begin{Bmatrix} \varepsilon_{rr} \\ \varepsilon_{\theta\theta} \\ \varepsilon_{zz} \\ \gamma_{r\theta} \\ \gamma_{rz} \\ \gamma_{\theta z} \end{Bmatrix} = \frac{1}{E}
\begin{bmatrix}
1 & -\upsilon & -\upsilon & 0 & 0 & 0 \\
-\upsilon & 1 & -\upsilon & 0 & 0 & 0 \\
-\upsilon & -\upsilon & 1 & 0 & 0 & 0 \\
0 & 0 & 0 & 2(1+\upsilon) & 0 & 0 \\
0 & 0 & 0 & 0 & 2(1+\upsilon) & 0 \\
0 & 0 & 0 & 0 & 0 & 2(1+\upsilon)
\end{bmatrix}
\begin{Bmatrix} \sigma_{rr} \\ \sigma_{\theta\theta} \\ \sigma_{zz} \\ \tau_{r\theta} \\ \tau_{rz} \\ \tau_{\theta z} \end{Bmatrix}
\qquad (3.1.7)
$$

The inverse relationship of Eq.(3.1.7) is given by:

$$
\begin{Bmatrix} \sigma_{rr} \\ \sigma_{\theta\theta} \\ \sigma_{zz} \\ \tau_{r\theta} \\ \tau_{rz} \\ \tau_{\theta z} \end{Bmatrix} = \frac{E}{(1+\upsilon)(1-2\upsilon)}
\begin{bmatrix}
1-\upsilon & \upsilon & \upsilon & 0 & 0 & 0 \\
\upsilon & 1-\upsilon & \upsilon & 0 & 0 & 0 \\
\upsilon & \upsilon & 1-\upsilon & 0 & 0 & 0 \\
0 & 0 & 0 & \frac{1}{2}-\upsilon & 0 & 0 \\
0 & 0 & 0 & 0 & \frac{1}{2}-\upsilon & 0 \\
0 & 0 & 0 & 0 & 0 & \frac{1}{2}-\upsilon
\end{bmatrix}
\begin{Bmatrix} \varepsilon_{rr} \\ \varepsilon_{\theta\theta} \\ \varepsilon_{zz} \\ \gamma_{r\theta} \\ \gamma_{rz} \\ \gamma_{\theta z} \end{Bmatrix}
\qquad (3.1.8)
$$

3.2.   Strain-Displacement Relations for Rotor Analysis

Let $u_r = u_r(r,\theta,z)$, $u_\theta = u_\theta(r,\theta,z)$ and $u_z = u_z(r,\theta,z)$ be   the   displacement components of an arbitrary material point in the r, θ and z directions, respectively. Normal and shear components of the deformation rate in cylindrical coordinates are $\varepsilon_{rr}, \varepsilon_{\theta\theta}, \varepsilon_{zz}$ and $\gamma_{\theta z}, \gamma_{rz}, \gamma_{r\theta}$, respectively. In the case of small deformations, corresponding strain-deformation relationships are given by the following expressions:

$$
\varepsilon_{rr} = \frac{\partial u_r}{\partial r}, \quad \varepsilon_{\theta\theta} = \frac{1}{r}\frac{\partial u_\theta}{\partial \theta} + \frac{u_r}{r}, \quad \varepsilon_{zz} = \frac{\partial u_z}{\partial z}
\qquad (3.2.1\text{a-c})
$$

$$
\gamma_{\theta z} = \frac{\partial u_\theta}{\partial z} + \frac{1}{r}\frac{\partial u_z}{\partial \theta}
\qquad (3.2.2)
$$

$$
\gamma_{rz} = \frac{\partial u_z}{\partial r} + \frac{\partial u_r}{\partial z}
\qquad (3.2.3)
$$

$$
\gamma_{r\theta} = \frac{1}{r}\frac{\partial u_r}{\partial \theta} + \frac{\partial u_\theta}{\partial r} - \frac{u_\theta}{r}
\qquad (3.2.4)
$$

3.3.   Finite Element Modeling

The Finite Element Method (FEM) is a powerful numerical analysis technique for obtaining approximate solutions to a wide variety of engineering problems. Since analytical solutions are difficult to obtain for many engineering problems, finite element analysis provides a cost-effective solution with acceptable results.

The finite element formulation of the problem yields a system of simultaneous algebraic equations for the solution, rather than requiring the solution of differential equations in analytical problems. Formulating the finite element solution begins with discretizing the structure into smaller elements. Discretization is the process of modeling a body by dividing it into an equivalent system of smaller bodies or units (i.e. finite elements). Elements are typically interconnected at points common to two or more elements (nodal point or nodes) [Logan, 1993]. Various element types are available that are characterized by element geometry, the number of elements, number of degrees of freedom per node and the type of interpolation functions used to approximate deformations across the element domain. An element type is selected based on the physical makeup of the body, and its ability to closely resemble the actual behavior of the structure.

In FEM, instead of solving the problem for the entire body in one operation, equations are formulated for each finite element and combined to obtain a solution for the entire body. Typically, to formulate structural problems the concepts of strain energy and minimum potential energy are used, and the solution refers to determining the displacements at each node and the stresses within each element that make up the structure being subjected to applied loads.

By using FEM, numerous variables can be examined and scenarios explored in order to limit the range of practical variables for physical testing. The numerical model can further be used to complement physical testing by modeling stresses, strains, and support reactions to aid the understanding of physical tests. The finite element model presented later in this chapter allows for the exploration of different parameters pertaining to the performance of flywheel rotors under inertia loading conditions. In any case, to use FEM proficiently and competently a thorough understanding of techniques for modeling a structure, boundary conditions, and limitations of the procedure is crucial.

3.3.1.   Nodal and Element Relations for Displacement and Strain

In finite element modeling, strain-displacement relations for a particular element type are found based on shape functions that interpolate element deformations between its nodal points.
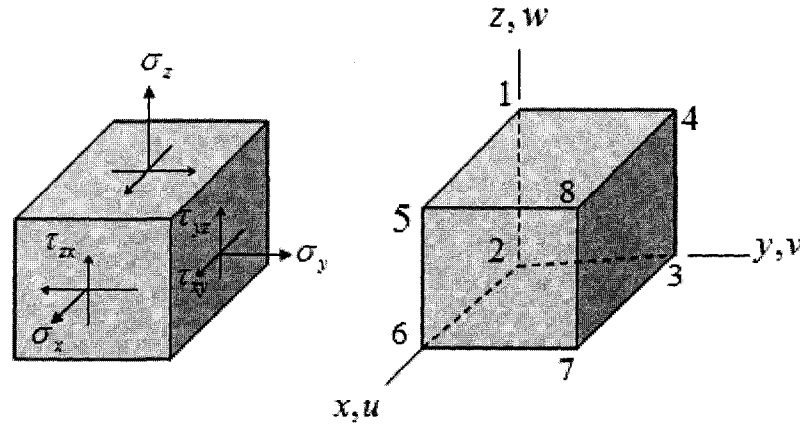
Figure 3.3.1: Element showing 3-dimensional state of stress (left-hand-side),

and 8-node hexahedron finite element (right-hand-side).

In case of a 3-dimensional 8-node solid element (shown in Fig.3.3.1) displacements are found in the following way. Displacements u within an element are interpolated according to the nodal degree of freedom by $u = N d$, where N is the shape function matrix, i.e.

$$
\begin{Bmatrix} u \\ v \\ w \end{Bmatrix} = \begin{bmatrix} N_1 & 0 & 0 & N_2 & 0 & 0 & \dots \\ 0 & N_1 & 0 & 0 & N_2 & 0 & \dots \\ 0 & 0 & N_1 & 0 & 0 & N_2 & \dots \end{bmatrix} \begin{Bmatrix} u_1 \\ v_1 \\ w_1 \\ u_2 \\ v_2 \\ w_2 \\ \vdots \\ . \end{Bmatrix} \tag{3.3.1}
$$

An element stiffness matrix k is derived as follows: Substitution of $u = N d$ into the appropriate strain-displacement relationship yields the strain-displacement matrix B,

given by $B = \partial N$, which in turn enters the integrand of the formula for the element stiffness matrix k. For 3-dimensional solids these equations are [Cook, 1995]:

$$\underset{6\times1}{\varepsilon} = \underset{6\times3n}{B}\ \underset{3n\times1}{d} \tag{3.3.2}$$

$$\underset{3n\times3n}{k} = \iiint B^T\ \underset{6\times6}{E}\ B\ dxdydz \tag{3.3.3}$$

Consequently, the element strain for 3-dimensional stress states is given by:

$$
\begin{bmatrix} \varepsilon_x \\ \varepsilon_y \\ \varepsilon_z \\ \gamma_{xy} \\ \gamma_{yz} \\ \gamma_{zx} \end{bmatrix} =
\begin{bmatrix}
\dfrac{\partial u}{\partial x} \\[2mm]
\dfrac{\partial v}{\partial y} \\[2mm]
\dfrac{\partial w}{\partial z} \\[2mm]
\dfrac{\partial u}{\partial y} + \dfrac{\partial v}{\partial x} \\[2mm]
\dfrac{\partial v}{\partial z} + \dfrac{\partial w}{\partial y} \\[2mm]
\dfrac{\partial w}{\partial x} + \dfrac{\partial u}{\partial z}
\end{bmatrix} =
$$

$$
\begin{bmatrix}
\dfrac{\partial N_1}{\partial x} & 0 & 0 & \dfrac{\partial N_2}{\partial x} & 0 & 0 & \dfrac{\partial N_3}{\partial x} & 0 & 0 & \cdots \\[2mm]
0 & \dfrac{\partial N_1}{\partial y} & 0 & 0 & \dfrac{\partial N_2}{\partial y} & 0 & 0 & \dfrac{\partial N_3}{\partial y} & 0 & \cdots \\[2mm]
0 & 0 & \dfrac{\partial N_1}{\partial z} & 0 & 0 & \dfrac{\partial N_1}{\partial z} & 0 & 0 & \dfrac{\partial N_1}{\partial z} & \cdots \\[2mm]
\dfrac{\partial N_1}{\partial y} & \dfrac{\partial N_1}{\partial x} & 0 & \dfrac{\partial N_2}{\partial y} & \dfrac{\partial N_2}{\partial x} & 0 & \dfrac{\partial N_3}{\partial y} & \dfrac{\partial N_3}{\partial x} & 0 & \cdots \\[2mm]
0 & \dfrac{\partial N_1}{\partial z} & \dfrac{\partial N_1}{\partial y} & 0 & \dfrac{\partial N_2}{\partial z} & \dfrac{\partial N_2}{\partial y} & 0 & \dfrac{\partial N_3}{\partial z} & \dfrac{\partial N_3}{\partial y} & \cdots \\[2mm]
\dfrac{\partial N_1}{\partial z} & 0 & \dfrac{\partial N_1}{\partial x} & \dfrac{\partial N_2}{\partial z} & 0 & \dfrac{\partial N_2}{\partial x} & \dfrac{\partial N_3}{\partial z} & 0 & \dfrac{\partial N_3}{\partial z} & \cdots
\end{bmatrix}
\begin{bmatrix} u_1 \\ v_1 \\ w_1 \\ u_2 \\ v_2 \\ w_2 \\ \vdots \end{bmatrix} \tag{3.3.4}
$$

3.3.2.   Numerical Modeling for Single Isotropic Flywheel Rotors

Modeling is the simulation of a physical structure or physical process by means of analytical or numerical constructs. Finite element modeling requires that the physical action of the problem is understood well enough to choose suitable kinds of elements and that enough of them are present to adequately represent the physical action [Cook, 1995]. The selection of the most appropriate element type for a particular problem is one of the major tasks during FEM design [Logan, 1993]. A flywheel rotor model should be such that the physical shape and discretization structure allows for a numerical solution that closely predicts the physical behavior of the actual flywheel rotor. Previous studies found in the technical literature showed that the most significant part of the flywheel rotor is the rotor rim. Hence, present flywheel modeling and optimization efforts initially considered only the rim for investigating rotor stresses and methods for reducing them. Nevertheless, later in this chapter a complete flywheel rotor model including an aluminum hub is described which permits the performance analysis of a complete flywheel rotor.

3.3.3.1.   Description of the Model

A 3-dimensional finite element model was developed using solid elements for the composite flywheel rotor. Although a 3-dimensional model requires decisively more computational resources, it was used for several reasons. The finite element software used in this study, ANSYS, offers the possibility to employ layered solid elements with distinct layer orientations for representing fiber-reinforced composite materials. Hence, material properties do not need to be homogenized in the rotor through-thickness direction. As mentioned previously, a goal of this study was to develop a finite element model of a complete flywheel rotor that closely resembles the physical behavior of an actual flywheel rotor. To accomplish this, a hub was incorporated into the model developed for design optimization. Since hub structures frequently have non-axisymmetric geometries (i.e. featuring bores), it was decided against using a simpler 2-dimensional (axisymmetric) model. To reduce computational time in the 3-dimensional model, symmetric conditions were applied to reduce the model size, making it possible to

use only a small section of the rotor instead of the entire rotor assembly. For the analyses presented in the present chapter, only a 45^0-section model was employed.

3.3.3.2. Model Geometry for a Single-Material Rotor

On the left-hand-side of Fig.3.3.2 a schematic of a single-material flywheel rotor is shown. Due to the symmetric nature of loading, it was chosen to model only a one-eighth section of the full rotor using appropriate boundary conditions, see the right-hand-side of Fig. 3.3.2.
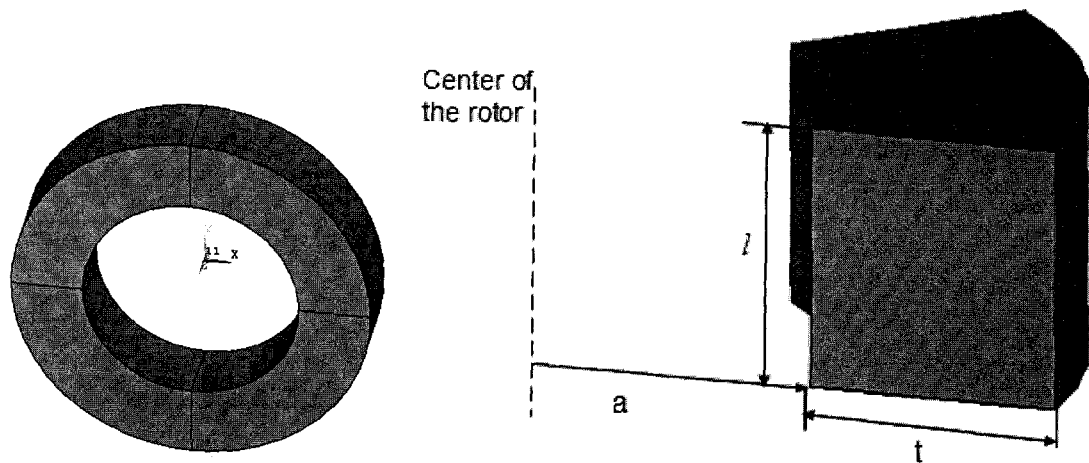
Figure 3.3.2: Single-material flywheel rotor (left-hand-side),

and 1/8 rotor section with cylindrical coordinates (right-hand-side).

Due to the cylindrical shape, the flywheel rotor was modeled in cylindrical coordinates. In the ANSYS graphics display the geometry is always shown in Cartesian coordinates. Cylindrical coordinates are activated using an ANSYS command. In that way, Cartesian-X refers to cylindrical R (radial), Cartesian-Y refers to cylindrical θ (hoop) and Cartesian-Z refers to cylindrical Z (Axial) (as shown in Fig.3.3.3). Across the technical literature this coordinate notation is identical. For the single-material rim as shown in Fig.3.3.2, the thickness of the rim is t, the inner and outer radius of the rim are a and $a + t$, and the height of the rotor in the axial direction is l.
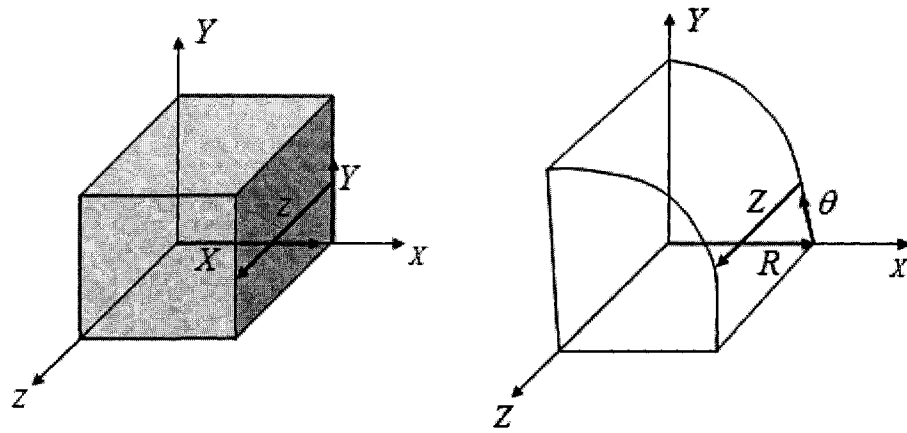
Figure 3.3.3: Cartesian (left-hand-side) and cylindrical (right-hand-side) global coordinates.

3.3.3.3. Element Selection for the Isotropic Model

As mentioned previously, element selection is a rather important task and it should be done as to achieve a model that is as close as possible to the original structure. For isotropic, single-material models of the flywheel rotor, element type SOLID45 was used, which is a 3-dimensional structural solid element with 8-nodes with three degrees of freedom per node [ANSYS]. Note that SOLID45 is similar SOLID46, which is the layer version of this element type used for subsequent modeling of orthotropic material rotors. At this stage of the study, a single-material, isotropic flywheel rotor was modeled and subjected to inertia loadings, to enable a comparison of model data to corresponding results from elasticity theory.

3.3.3.4. Meshing of the Flywheel Rotor for a Single Material Ring

Meshing is an integral part of any finite element analysis process. The mesh influences accuracy, convergence and speed of the solution. As suitable rotor model must provide an adequate mesh resolution for each component of the structure. Elements must be compact and regularly shaped. Too finely meshing would cause unnecessary computational

overheads during program runs, whereas too coarse of a mesh may produce intolerable approximation errors.

The ANSYS software package allows for two meshing types. Free meshing imposes little restriction on element shapes and the pattern of element arrangement. Mapped meshing is restricted in terms of the element shape and the pattern of the mesh. A mapped mesh typically has a regular pattern with obvious rows of elements. In free meshing quadrilateral and triangular elements may be employed, while in mapped meshing only hexahedron elements are used.

For the single rim model, an inner and outer diameter of the rim of 24 cm and 48 cm was selected respectively. The rim height was 12 cm. Since the rotor geometry is regular shaped, mapped meshing with 10 element divisions along the boundary lines was specified. Consequently, 1000 elements with balanced aspect ratios were generated for the 1/8 section of the flywheel rotor, see Fig.3.3.4. Note that a sensitivity analysis was also performed to find an adequate mesh density for proper representation of inertia effect while maintaining reasonable computing effort (see Section 3.3.3.8).
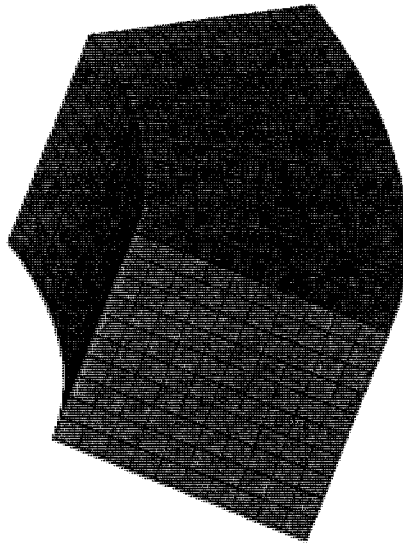
Figure 3.3.4: Coarse meshing of 45°-section single-material flywheel rotor model.

3.3.3.5. Loading and Displacement Boundary Conditions

Inertia loading is the main type of loading for flywheel rotors that typically generate high stresses in the radial and circumferential directions of the rotor. In the finite element

modeling environment, inertial loading due to fixed axis rotation is independent of the finite element mesh. This allows for mesh modifications and conducting mesh sensitivity studies without having to modify and reapply loadings for each model variation. In ANSYS, inertia loads in the model are automatically transferred by the program to the finite elements at the beginning of the solution procedure. In this model, rotational velocity was applied with respect to the Z-axis, see Fig.3.3.6.

Prior to solving the finite element model, proper displacement boundary conditions were set in order to fulfill the symmetry conditions. As mentioned previously, symmetry conditions were applied to reduce the size of the model without loss of accuracy. These constraints in terms of u_r, u_θ and u_z were:

$$u_\theta(r,\theta,z) = 0 \quad \text{for} \quad a \leq r \leq a+t, \ \theta = 0° \quad \text{(Symmetry constraint)}$$

$$u_\theta(r,\theta,z) = 0 \quad \text{for} \quad a \leq r \leq a+t, \ \theta = 45° \quad \text{(Symmetry constraint)}$$

$$u_z(r,\theta,z) = 0 \quad \text{for} \quad r = a, \ \theta = 0° \quad \text{(Rigid body motion constraint)}$$
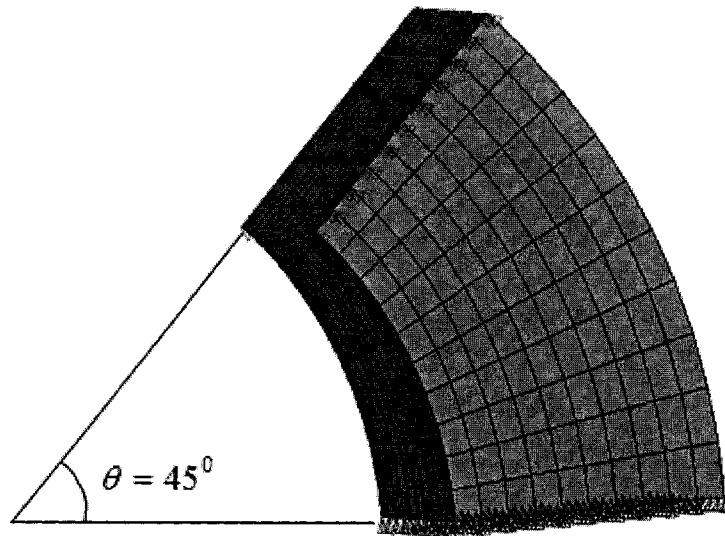
Figure 3.3.6: 45°-section of rotor model showing displacement boundary conditions.

3.3.3.6. Material Properties

Material properties used in this study for single-material rotor models (aluminum, carbon/epoxy composite) and a two-material hybrid rotor model with carbon/epoxy and E-glass/epoxy rims are summarized in Table 3.3.1.

Table 3.3.1: Properties for carbon/epoxy, glass/epoxy and aluminum [Daniel and Ishai, 2006].

Property	Carbon/epoxy unidirectional (AS4/3501-6)	E-Glass/epoxy unidirectional	Aluminum
Density, ρ, g/cm^3	1.60	1.97	2.7
Longitudinal modulus, E_1, GPa	147	41	71.7
Transverse modulus, E_2, GPa	10.3	10.4	
Major in-plane Poisson's ratio, υ_{12}	0.27	0.28	0.34
Out-of-plane Poisson's ratio, υ_{23}	0.54	0.50	
Out-of-plane Poisson's ratio, υ_{13}	0.27	0.28	
In-plane shear modulus, G_{12}, GPa	7	4.3	26.8
Out-of-plane shear mod. , G_{23}, GPa	3.7	3.5	
Out-of-plane shear mod., G_{13}, GPa	7	4.3	
Longitudinal tensile strength, σ_1^T, MPa	2280	1140	
Transverse tensile strength, σ_2^T, MPa	57	39	
Longitudinal compressive strength, σ_1^C, MPa	1725	620	
Transverse compressive strength, σ_2^C, MPa	228	128	

3.3.3.7. Results for Isotropic Single-Material Rotor Rim

Shown on the left- and right-hand-side of Fig.3.3.7 are circumferential and radial rotor stresses, respectively, that were obtained from the numerical model for a rotational speed of 10,000 RPM. Stress data were taken along the thickness-direction from the rotor mid-plane. The maximum radial stress was 18.2 MPa, and radial stress was approximately zero at the inner and outer surface of the rotor rim due to free surface effects. The maximum hoop stress of 151 MPa was found at the inner surface of the flywheel rotor; hoop stress diminished from the inner to outer radius of the rotor. Contour plots for full radial and circumferential stress, circumferential strain and radial displacement are shown in Figs.3.3.8 to 3.3.10.
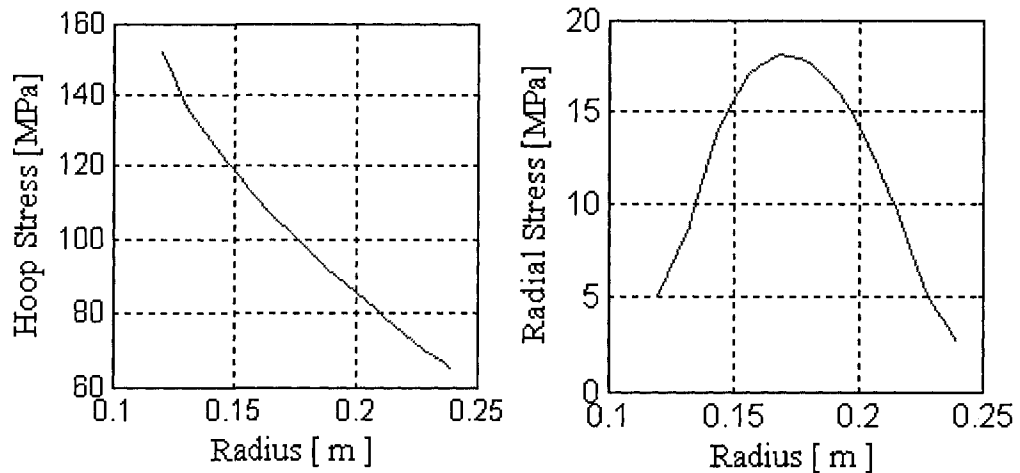
Figure 3.3.7: Mid-plane hoop stress (left-hand-side) and radial stress profile (right-hand-side) for aluminum rotor model with rotational speed of 10,000 RPM (45°-section with 1000 elements).

```
.253E+07        .601E+07        .948E+07        .130E+08        .164E+08
     .427E+07        .774E+07        .112E+08        .147E+08        .182E+08
```
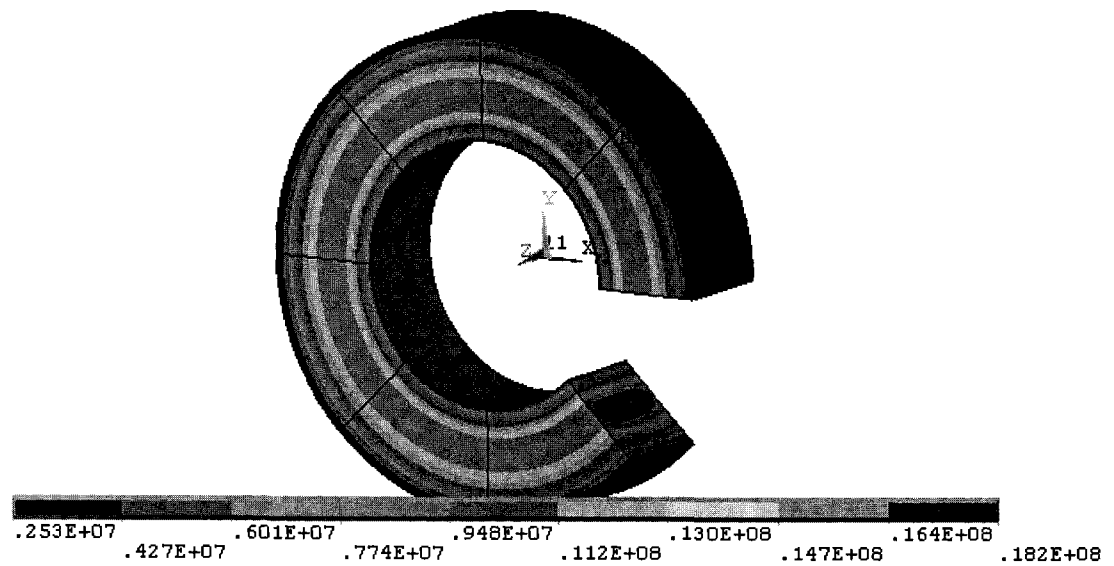
Figure 3.3.8: Radial stress field (Units: Pa) for aluminum rotor model with rotational speed of 10,000 RPM (expanded view of 45°-section with 1000 elements).


```
.634E+08        .831E+08        .103E+09        .122E+09        .142E+09
     .732E+08        .929E+08        .113E+09        .132E+09        .152E+09
```
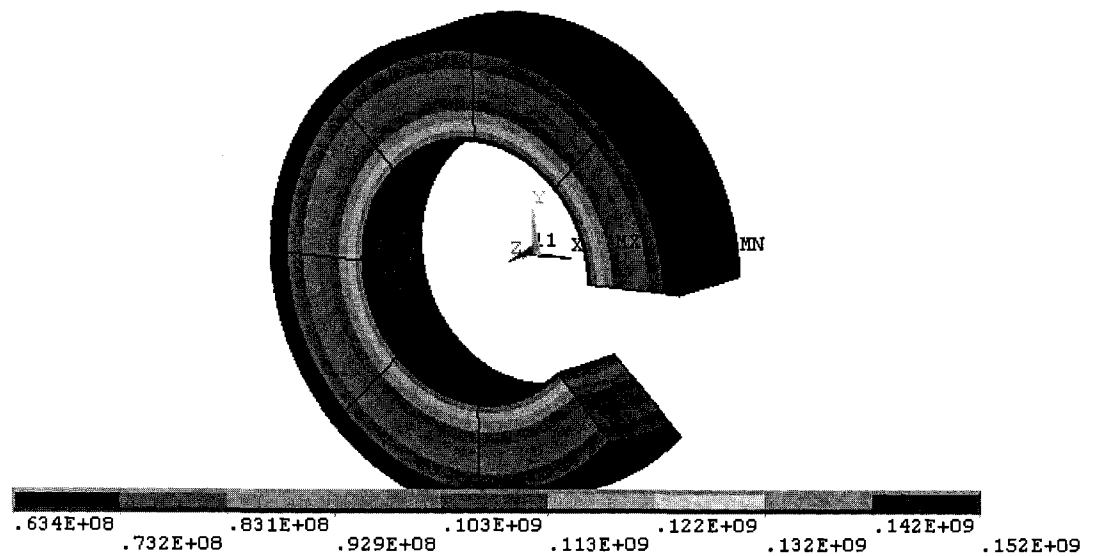
Figure 3.3.9: Circumferential stress field (Units: Pa) for aluminum rotor model with rotational speed of 10,000 RPM (expanded view of 45°-section with 1000 elements).

```
.869E-03          .00114          .001411          .001683          .001954
       .001004          .001276          .001547          .001819          .00209
```
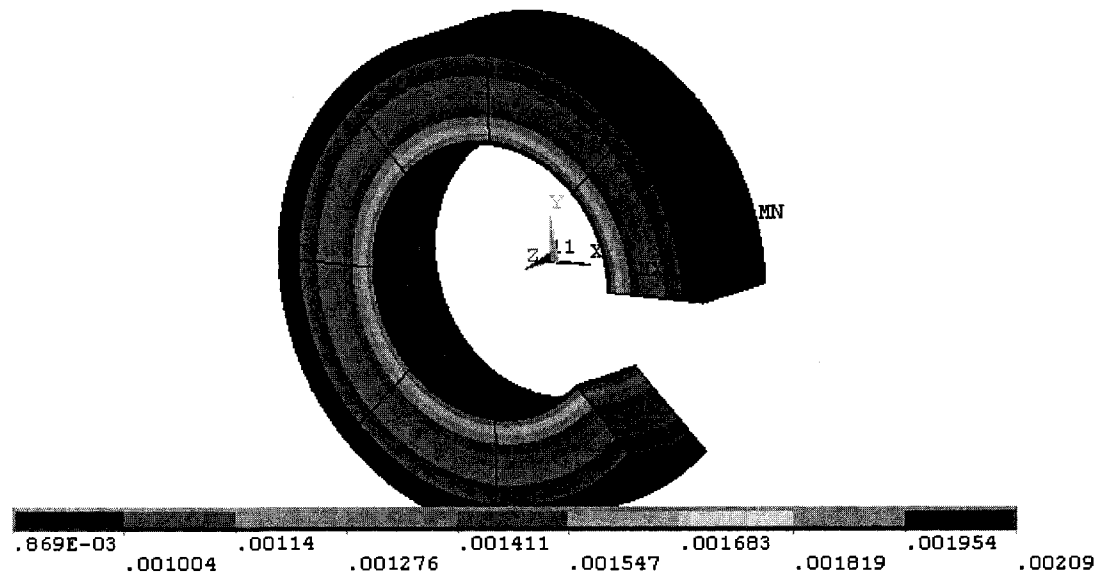
Figure 3.3.10: Circumferential strains (Units: mm/mm) for aluminum rotor model with rotational speed of 10,000 RPM (expanded view of 45°-section with 1000 elements).


```
.209E-03          .219E-03          .228E-03          .238E-03          .247E-03
       .214E-03          .223E-03          .233E-03          .242E-03          .252E-03
```
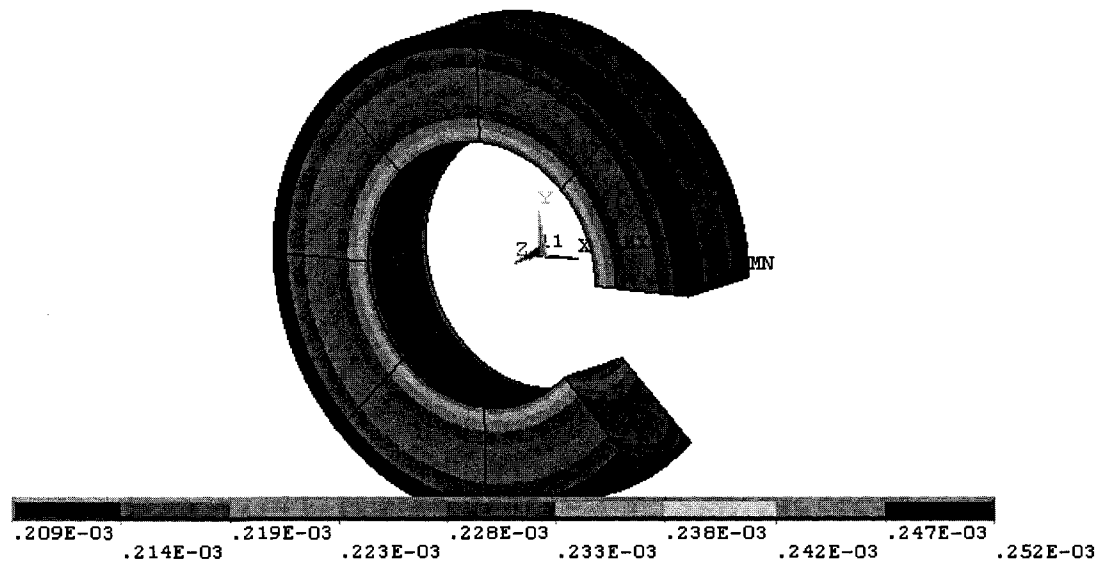
Figure 3.3.11: Radial displacement field (Units: m) for aluminum rotor model with rotational speed of 10,000 RPM (expanded view of 45°-section with 1000 elements).

3.3.3.8. Mesh Sensitivity Analysis for the Single-Rim Rotor Model

In order to investigate whether the finite element mesh was properly sized and consistent results were generated, a sensitivity analysis was performed. Appropriate mesh density of a finite element model is essential for the competent and precise use of FEM, in particular those involving complex structures or interactions. In model zones with small stress and deformation gradients, relatively large elements usually provide good accuracy, while in zones with strong variations much smaller elements are needed to accurately represent physical behavior. To avoid an ill-conditioned mesh, gradual transitions from large to small elements need to be implemented during the mesh refinement process.

A convergence test was conducted for the aluminum rotor model to determine a suitable number of elements. Based on the previous model, effects of refined meshing were analyzed to determine a mesh density that yields the acceptable results in the shortest computational time possible. Six different mesh sizes were investigated and mesh refinement continued until variations of maximum radial and circumferential stresses were less than 0.1 percent. It was found that radial stress was much more sensitive to mesh size than circumferential stresses, and it need more mesh refinement to achieve adequate convergence (see Fig. 3.1.12). The initially unrefined mesh consisting of 64 elements per 45°-section and the refined mesh contained 1,728 elements. Numerical data were again taken from the rotor mid-plane. Models with 216 and 1,728 elements are shown on the left- and right-hand-side of Fig.3.3.13 respectively.

3.3.4. Validation of Single-Material Rotor Model

A considerable portion of time and effort was devoted to the validation of the finite element model. Results were compared with the analytical results as well as data from other studies. This validation process is considered crucial since the credibility of further design studies depends entirely on the accuracy of the numerical code. In the subsequent section the validity of the finite element model for the isotropic single-material flywheel rotor with inertia loading was tested. Numerical results were compared with analytical results obtain from elasticity theory.
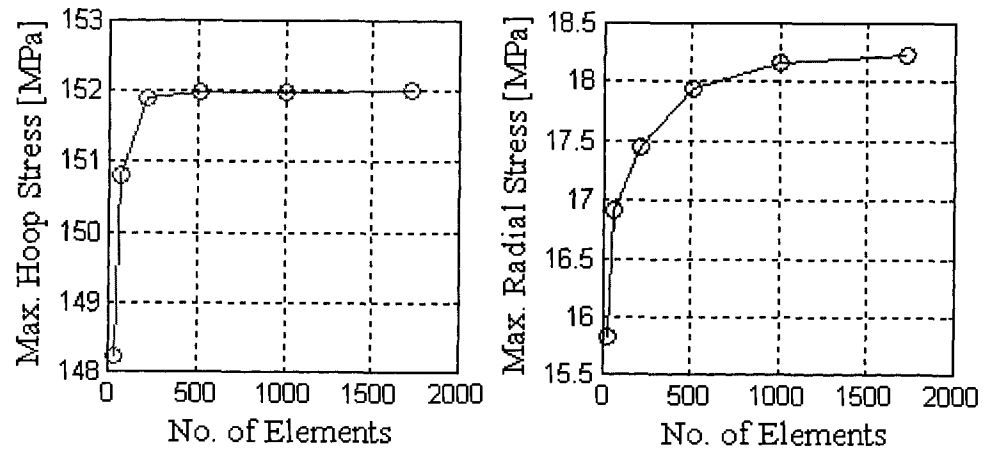
Figure 3.3.12: Variation of maximum hoop (left-hand-side) and radial stresses (right-hand-side) with respect to the number of elements in 45°-section under 10,000 RPM rotation.
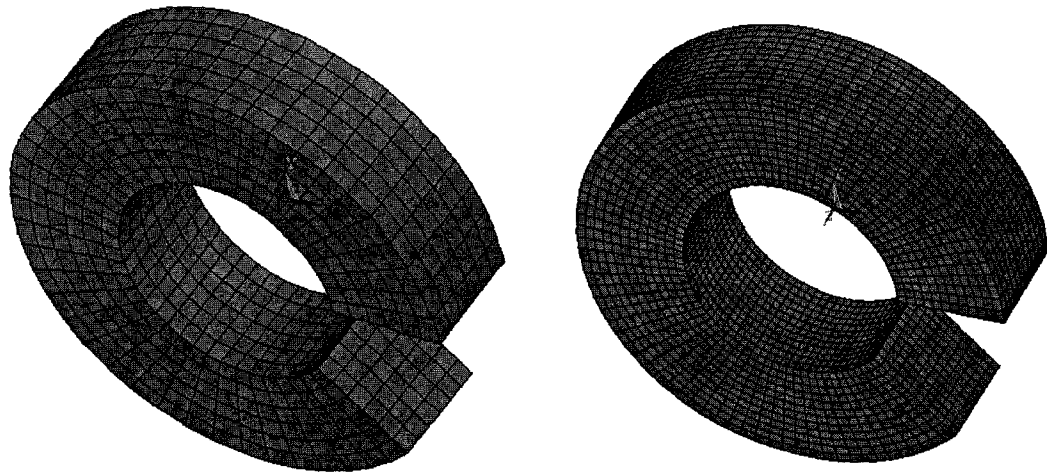
Figure 3.3.13.: Expanded view of coarsely meshed 45°-section model with 216 elements (left) and refined mesh with 1,728 elements (right).

3.3.4.1. Flywheel Rotor Stress Analysis

The stresses and deformations of a rotating disk having constant thickness and an inner radius a and outer radius b, can be obtained from 3-dimensional equilibrium equations for a continuum that are formulated based on the principle of conservation of linear

momentum (i.e. Newton's second law of motion). The equations are expressed in cylindrical coordinates as [Lekhnitskii, 1956]:

$$\frac{\partial \sigma_{rr}}{\partial r} + \frac{1}{r}\frac{\partial \tau_{r\theta}}{\partial \theta} + \frac{\partial \tau_{rz}}{\partial z} + \frac{\sigma_{rr}-\sigma_{\theta\theta}}{r} + F_r = 0 \qquad (3.3.5a)$$

$$\frac{\partial \tau_{r\theta}}{\partial r} + \frac{1}{r}\frac{\partial \tau_{\theta\theta}}{\partial \theta} + \frac{\partial \tau_{\theta z}}{\partial z} + \frac{2\tau_{r\theta}}{r} + F_\theta = 0 \qquad (3.3.5b)$$

$$\frac{\partial \tau_{rz}}{\partial r} + \frac{1}{r}\frac{\partial \tau_{\theta z}}{\partial \theta} + \frac{\partial \tau_{zz}}{\partial z} + \frac{\tau_{rz}}{r} + F_z = 0 \qquad (3.3.5c)$$

Stress components on planes normal to the cylindrical coordinates were previously shown in Fig.3.1.2. They are designated, correspondingly, σ_{rr}, $\sigma_{\theta\theta}$, σ_{zz}, $\tau_{r\theta}$, τ_{rz}, and $\tau_{\theta z}$. In the above equations, F_r, F_θ, F_z are body forces for a unit volume in the cylindrical coordinate directions.

Assuming that the thickness of the rotating disk is small in comparison to its radius, then the variation of radial and circumferential stresses over the thickness can be neglected and $\sigma_{zz} = 0$. Due to loading/geometric symmetry Eqs.(3.3.5a-c) reduce to [Ugral, 1994]:

$$\frac{\partial \sigma_{rr}}{\partial r} + \frac{\sigma_{rr}-\sigma_{\theta\theta}}{r} + \rho r \omega^2 = 0 \qquad (3.3.6)$$

Employing Hooke's law, the strains are given by:

$$\varepsilon_{rr} = \frac{du_r}{dr} = \frac{1}{E}[\sigma_{rr} - \upsilon\sigma_{\theta\theta}] \qquad (3.3.7a)$$

$$\varepsilon_{\theta\theta} = \frac{u_r}{r} = \frac{1}{E}[\sigma_{\theta\theta} - \upsilon\sigma_{rr}] \qquad (3.3.7b)$$

where ε_{rr} and $\varepsilon_{\theta\theta}$ are the strains in the radial and circumferential directions, u_r is the displacement in the radial direction, E is the elastic modulus and υ is the Poisson's ratio.

From Eqs.(3.3.7a-b) stress components $\sigma_{\theta\theta}$ and σ_{rr} are given by:

$$\sigma_{rr} = \frac{E}{1-\upsilon^2}\left[\frac{du_r}{dr} + \upsilon\frac{u_r}{r}\right] \qquad (3.3.8a)$$

$$\sigma_{\theta\theta} = \frac{E}{1-\upsilon^2}\left[\frac{u_r}{r} + \upsilon\frac{du_r}{dr}\right] \qquad (3.3.8b)$$

Substituting Eqs.(3.3.8a) into Eq. (3.3.6), the following expressions is obtained:

$$r^2 \frac{d^2 u_r}{dr^2} + r \frac{du_r}{dr} - u_r = -\frac{1-\upsilon^2}{E} \rho \omega^2 r^3 \tag{3.3.9}$$

Above equation is a non-homogeneous, second order linear ordinary differential equation. The general solution is found as:

$$u_r = c_1 r + \frac{c_2}{r} - \frac{\rho \omega^2 r^3 (1-\upsilon^2)}{8E} \tag{3.3.10}$$

where u_r constitutes the complementary plus particular solution.

From Eqs.(3.3.8a-b) follows:

$$\sigma_{rr} = \frac{E}{1-\upsilon^2} \left[\frac{-(3+\upsilon)(1-\upsilon^2)\rho \omega^2 r^2}{8E} + (1+\upsilon)c_1 - (1-\upsilon)\frac{c_2}{r^2} \right] \tag{3.3.11a}$$

$$\sigma_{\theta\theta} = \frac{E}{1-\upsilon^2} \left[\frac{-(1+3\upsilon)(1-\upsilon^2)\rho \omega^2 r^2}{8E} + (1+\upsilon)c_1 + (1-\upsilon)\frac{c_2}{r^2} \right] \tag{3.3.11b}$$

The radial and hoop stress distributions are calculated by using the following boundary conditions:

$$\sigma_{rr} = 0 \quad \text{at} \quad r = a \quad \text{and} \quad \sigma_{rr} = 0 \quad \text{at} \quad r = b$$

These conditions combined with Eqs.(3.3.11a-b) yield two equations for the two unknown constants c_1 and c_2,

$$0 = -\rho \omega^2 \frac{a^2}{E} \frac{(1-v^2)(3+v)}{8} + (1+v)c_1 - (1-v)\frac{c_2}{a^2} \tag{3.3.12a}$$

$$0 = -\rho \omega^2 \frac{b^2}{E} \frac{(1-v^2)(3+v)}{8} + (1+v)c_1 - (1-v)\frac{c_2}{b^2} \tag{3.3.12b}$$

From Eqs.(3.3.12a-b) follows:

$$c_1 = \rho \omega^2 \frac{(a^2+b^2)}{E} \frac{(1-v)(3+v)}{8} \tag{3.3.13a}$$

$$c_2 = \rho \omega^2 \left(\frac{a^2 b^2}{E} \right) \frac{(1+v)(3+v)}{8} \tag{3.3.13b}$$

The radial and circumferential stresses are therefore:

$$\sigma_{rr} = \frac{3+v}{8} \left(a^2 + b^2 - \frac{a^2 b^2}{r^2} - r^2 \right) \rho \omega^2 \tag{3.3.14a}$$

$$\sigma_{\theta\theta} = \frac{3+v}{8}\left(a^2 + b^2 + \frac{a^2b^2}{r^2} - \frac{1+3v}{3+v}r^2\right)\rho\omega^2 \qquad (3.3.14b)$$

All the previously mentioned, numerical solutions obtained from the developed finite element model were validated using analytical stress solutions. For a rotational speed of 10,000 RPM, radial and circumferential stresses in the rotor mid-plane along the thickness-direction obtained from numerical analysis were compared with the corresponding analytical results shown on the left- and right-hand-side of Fig.3.3.14. It can be observed that for both stress components, analytical and numerical results coincide. Small deviations were found only at the inner and the outer surfaces, which are to be expected due to free surface effect in finite element calculations (i.e. stresses are not calculated at the exact free surface but at integration points internal to the surface elements). Note that the quality of the agreement depended on mesh size, and only for the fine mesh sizes (1,728 elements) there was good agreement between the analytical and the numerical results.

Figure 3.3.14: Comparison of numerical and analytical results of radial (left) and circumferential stresses (right) for an aluminum rotor model with 1,728 elements at 10,000 RPM.

3.3.5.   Numerical Modeling for Orthotropic Single-Material Flywheel Rotors

Fiber-reinforced composite materials are usually orthotropic materials (see Fig.3.3.15). Orthotropic materials have mechanical properties that are different in three mutually perpendicular directions at a point within the body, and possess three mutually perpendicular planes of material symmetry. They have dissimilar elastic behavior in different directions. The design of a laminated composite includes selecting a material system or a group of material systems (hybrid composites) and determining the fiber orientation and stacking sequence for the laminate based on applied loads, as well as other design constraints such as cost, weight, dimensions. Thus the design of a composite component not only includes designing the shape and size, but also designing the material itself.

An important characteristic of a composite flywheel rotor is its layer configuration and fiber direction within each layer. The laminate lay-up for an orthotropic single material flywheel rim investigated in the present study consisted of 6 layers. Fibers in all layers were directed in the rotor circumferential direction.
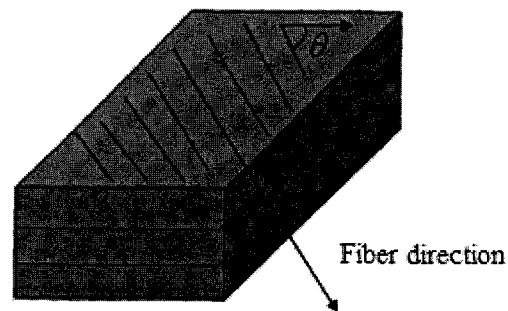
Figure 3.3.15: Schematic of a fiber-reinforced composite laminate.

3.3.5.1. Element Selection for Orthotropic Single-Material Rotor Models

For the orthotropic material case, the flywheel rotor was modeled using eight nodes, three degrees of freedom per node, a 3-dimensional structural layered solid element named Solid 46 [ANSYS]. The input for this element type allows for specification of thickness, fiber orientation and orthotropic material properties for sequence of each layer. The use of this element type implies certain assumptions with regard to the element lay-up. It assumes that there is perfect bonding between layers with no allowance for delamination or slippage between layers. Material orientations in this element are parallel to the element reference plane and any warp layer acts as if it is flat and parallel to the reference plane. Furthermore, since element stress directions correspond to the layer local coordinate directions it is possible to achieve the desired stress directions such as radial and circumferential stresses for a rotating flywheel rotor using this element type.

3.3.5.2. Meshing of the Orthotropic Single-Material Rotor Model

For the orthotropic single material flywheel rim, a similar geometric shape was used as in the isotropic cases (i.e. inner diameter of 24 cm, outer diameter of 48 cm, and rotor height of 12 cm). Also, meshing for the orthotropic material model was similar to the isotropic case except for added layer properties thickness and orientation. Ten element divisions were specified along the boundaries of the 45°-section model producing a mapped mesh. As a result, 1,000 elements were generated with 1.2 cm thickness each. Six layers were specified for each element, resulting in a layer thickness of 2 mm. All layers were oriented in circumferential direction paralleling element local coordinates. Material properties for carbon/epoxy were assigned for each layer. The mesh configuration including element layering and layer orientation for the orthotropic single-material rotor model is shown in the Figs. 3.3.17 to 3.3.19.
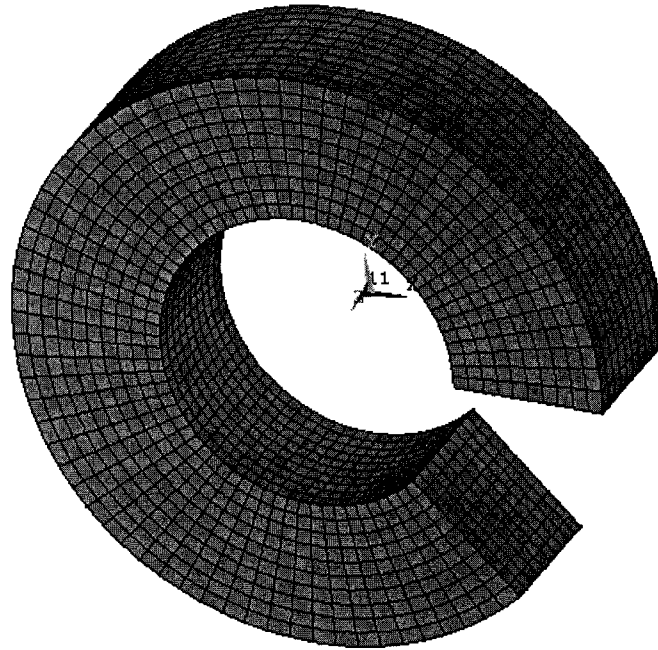
Figure 3.3.17: Meshing for orthotropic single-material flywheel rotor
modeled with 1000 elements.
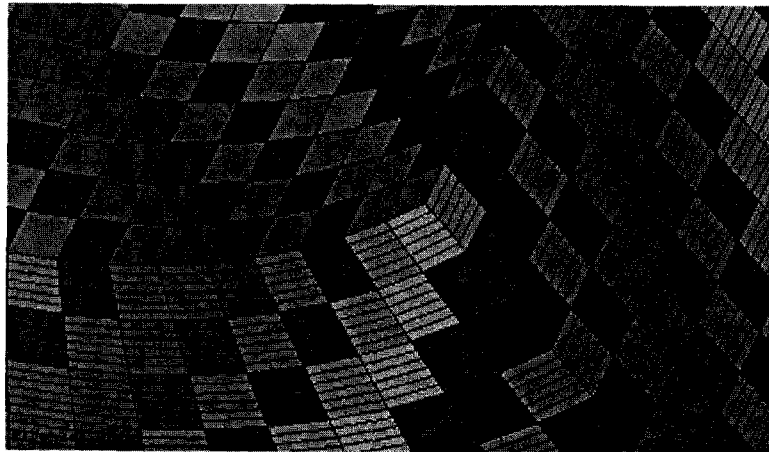
Figure 3.3.18: Close-up of meshing for orthotropic single-material flywheel rotor
showing layering of each element.

```
LAYER STACKING
ELEM      = 377
TYPE      =   1
REAL      =   1
LAYERS :
TOTAL     =   6
SHOWN  :
FROM   1 TO   6
```
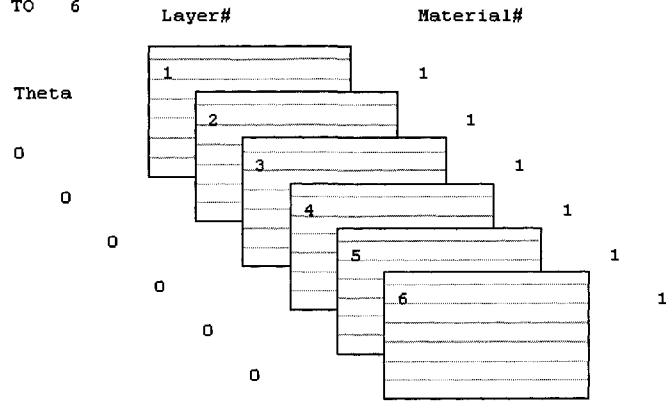
Figure 3.3.19: Sequence and orientation of layers in elements
for orthotropic single-material flywheel rotor.

3.3.5.3. Results for an Orthotropic Single-Material Flywheel Rim

For the orthotropic single-material flywheel rotor the same boundary conditions were applied as in the case of the isotropic single-material (aluminum) rotor. In the present case, however, a higher rotational speed of 20,000 RPM was applied. Circumferential and radial stresses in the rotor mid-plane in the through-thickness direction obtained from the numerical model are illustrated in Fig.3.3.20. Contour plots showing the circumferential stress, radial stress, circumferential strain and radial displacement fields are shown in Figs.3.3.21 to 3.3.24.

From the right-hand-side of Fig.3.3.20 it was found that the maximum radial stress was 26.65 MPa, which was approximately located in the centre of the rotor cross-section (i.e. 6 cm from the inner diameter). The left-hand-side of Fig.3.3.20 indicates that the maximum hoop stress was 245 MPa located at the inner rotor radius and 7.6 cm from the inner surface in the thickness direction. The hoop stress profile shown in Fig.3.3.20 was different from the profile obtained in the isotropic cases, i.e. for the orthotropic material more complex stress distributions develop that depend not only on the rotor geometry but are also strongly affected by the composite material systems. Nevertheless, fiber

composites are usually preferred for flywheel rotor since flywheel performance increases with increasing tensile strength and decreasing material density.
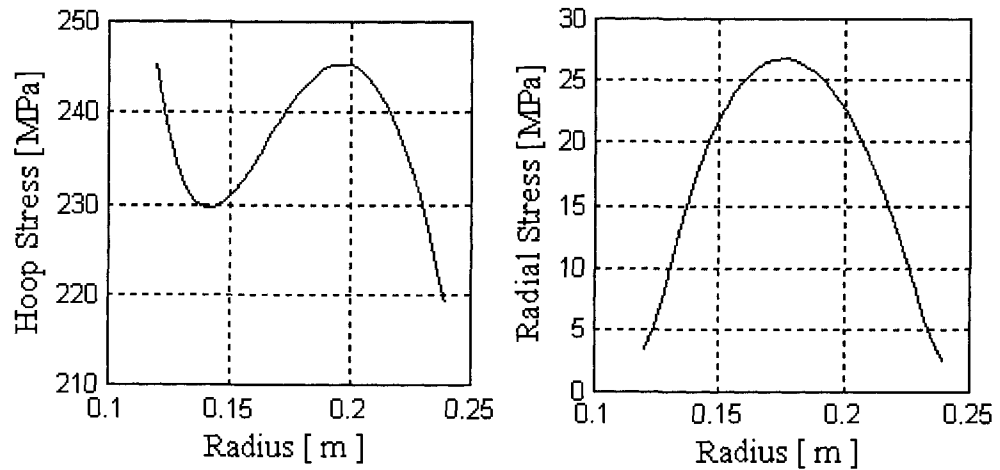
Figure 3.3.20: Mid-plane hoop (left) and radial stress profile (right) for a carbon/epoxy rotor model with rotational speed of 20,000 RPM (45°-section with 1000 elements).
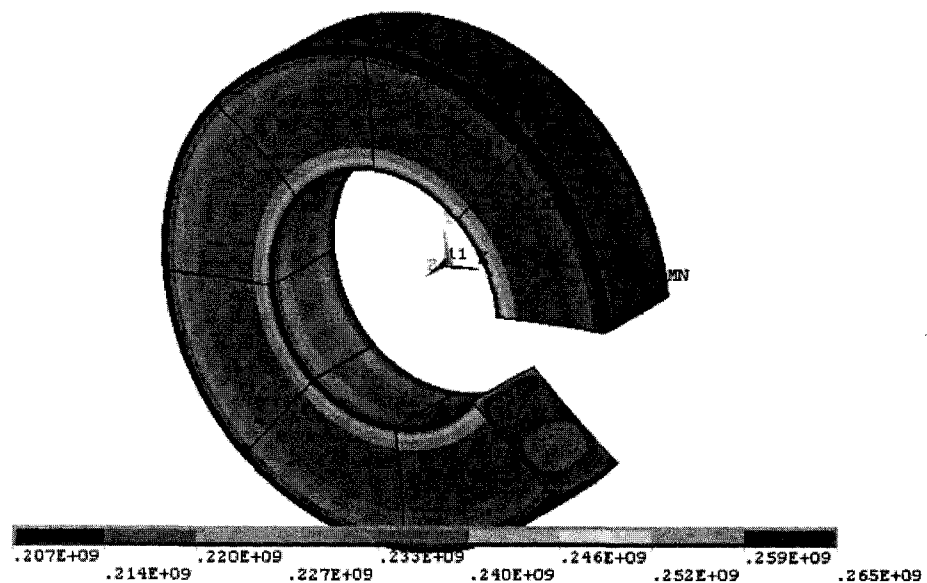
Figure 3.3.21: Circumferential stresses (Units: Pa) for a carbon/epoxy rotor model with rotational speed of 20,000 RPM (expanded view of 45°-section with 1000 elements).

.222E+07   .766E+07   .131E+08   .185E+08   .240E+08
        .494E+07   .104E+08   .158E+08   .213E+08   .267E+08

Figure 3.3.22: Radial stress field (Units: Pa) for a carbon/epoxy rotor model with rotational speed of 20,000 RPM (expanded view of 45°-section with 1000 elements).

.001405   .001492   .001579   .001666   .001753
        .001448   .001535   .001623   .00171   .001797
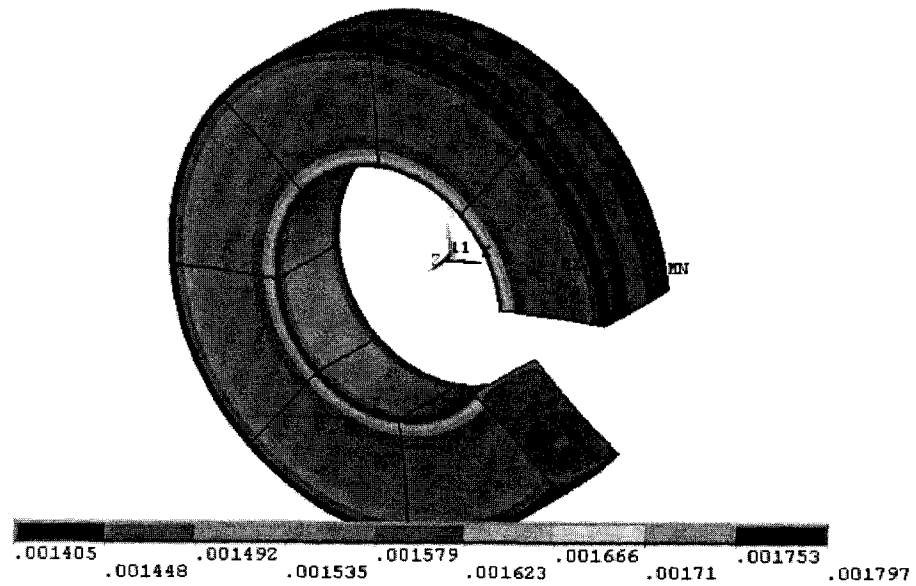
Figure 3.3.23: Hoop strains (Units: mm/mm) for a carbon/epoxy rotor model with rotational speed of 20,000 RPM (expanded view of 45°-section with 1000 elements).

```
.201E-03        .236E-03       .271E-03       .306E-03       .341E-03
      .218E-03       .253E-03       .289E-03       .324E-03       .359E-03
```

Figure 3.3.24: Radial displacement field (Units: m) for a carbon/epoxy rotor model with rotational speed of 20,000 RPM (expanded view of 45°-section with 1000 elements).

3.3.5.4. Model Validation for the Orthotropic Single-Material Flywheel Rotor

The stresses and displacements of composite rims made from an orthotropic material can also be determined from the equilibrium equations, i.e. Eqs.(3.3.5a-c) [Lekhnitskii, 1956]. The stress strain relation for a plane stress orthotropic condition is:

$$\begin{bmatrix} \varepsilon_{rr} \\ \varepsilon_{\theta\theta} \end{bmatrix} = \begin{bmatrix} \dfrac{1}{E_r} & -\dfrac{v_{\theta r}}{E_\theta} \\ -\dfrac{v_{r\theta}}{E_r} & \dfrac{1}{E_\theta} \end{bmatrix} \begin{bmatrix} \sigma_{rr} \\ \sigma_{\theta\theta} \end{bmatrix} \qquad (3.3.15)$$

where $\varepsilon_{rr}, \sigma_{rr}$ and $\varepsilon_{\theta\theta}, \sigma_{\theta\theta}$ are the strains and stresses in the radial and hoop directions, and E_r and E_θ are the radial and circumferential elastic moduli, respectively. Since only radial and hoop stresses were considered for the validation of the numerical model, expressions for shear stress and strain terms were omitted at this point.

The Poisson's ratio and the Young's modulus in the radial and hoop directions have the following relationship:

$$\frac{v_{\theta r}}{E_\theta} = \frac{v_{r\theta}}{E_r}$$

(3.3.16)

The stress components are obtained by rearranging Eq.(3.3.15), i.e.

$$\begin{bmatrix} \sigma_{rr} \\ \sigma_{\theta\theta} \end{bmatrix} = \begin{bmatrix} Q_{rr} & Q_{r\theta} \\ Q_{\theta r} & Q_{\theta\theta} \end{bmatrix} \begin{bmatrix} \varepsilon_{rr} \\ \varepsilon_{\theta\theta} \end{bmatrix}$$

(3.3.17)

where the Q-terms are given by:

$$Q_{rr} = \frac{E_r}{1 - v_{r\theta} v_{\theta r}}$$

(3.3.18a)

$$Q_{\theta\theta} = \frac{E_\theta}{1 - v_{r\theta} v_{\theta r}}$$

(3.3.18b)

$$Q_{r\theta} = Q_{\theta r} = \frac{v_{\theta r} E_r}{1 - v_{r\theta} v_{\theta r}} = \frac{v_{r\theta} E_\theta}{1 - v_{r\theta} v_{\theta r}}$$

(3.3.18c)

To obtain radial and hoop stresses the same boundary conditions as for the isotropic case were employed, i.e. $\sigma_{rr} = 0$ at $r = a$, and $\sigma_{rr} = 0$ at $r = b$, where a and b are the inner and outer radius of the rotor.

From the above the following solution for a rotating orthotropic material rim is found [Lekhnitskii, 1956]:

$$\sigma_{rr} = -\frac{(3 + v_{\theta r})}{9 - k^2} \rho\omega^2 b^2 \left[\left(\frac{r}{b}\right)^2 - \frac{1 - \left(\frac{a}{b}\right)^{k+3}}{1 - \left(\frac{a}{b}\right)^{2k}} \left(\frac{r}{b}\right)^{k-1} - \frac{1 - \left(\frac{a}{b}\right)^{-k+3}}{1 - \left(\frac{a}{b}\right)^{-2k}} \left(\frac{r}{b}\right)^{-k-1} \right]$$

(3.3.19)

$$\sigma_{\theta\theta} = -\frac{(3 + v_{\theta r})}{9 - k^2} \rho\omega^2 b^2 \left[\left(\frac{r}{b}\right)^2 \frac{k^2 + 3v_{\theta r}}{3 + v_{\theta r}} - k\frac{1 - \left(\frac{a}{b}\right)^{k+3}}{1 - \left(\frac{a}{b}\right)^{2k}} \left(\frac{r}{b}\right)^{k-1} - k\frac{1 - \left(\frac{a}{b}\right)^{-k+3}}{1 - \left(\frac{a}{b}\right)^{-2k}} \left(\frac{r}{b}\right)^{-k-1} \right]$$

(3.3.20)

where $k = \sqrt{\frac{E_\theta}{E_r}}$.

Stress data from the analytical solution were compared for radial and circumferential stresses with the numerical results. As shown in Fig.3.3.25, values from numerical investigation qualitatively agree well with analytical results; the maximum difference between analytical and numerical data was 8% and 1% for radial and circumferential stresses respectively.
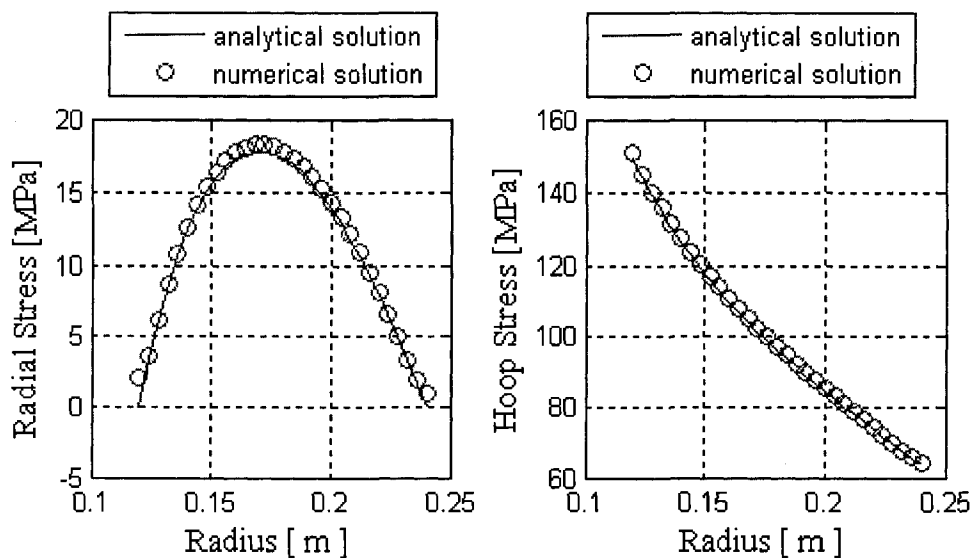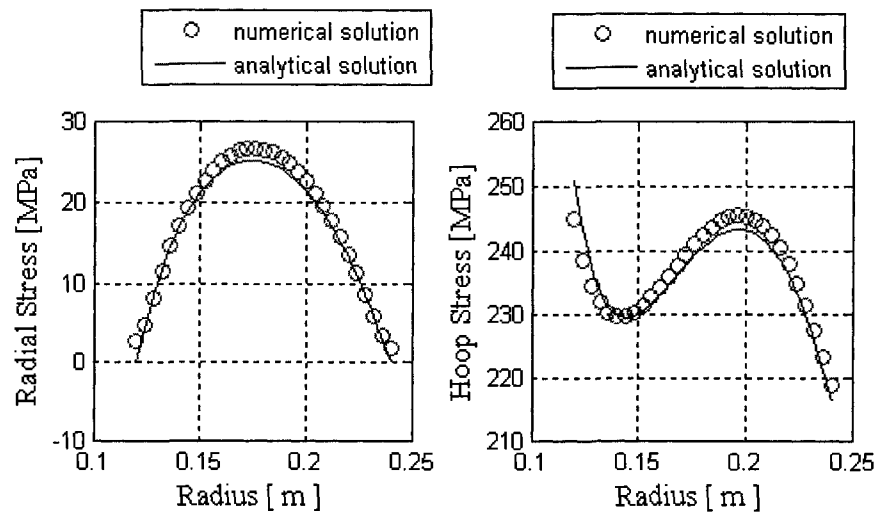
Figure 3.3.25: Comparison of numerical and analytical results of radial (left) and circumferential stresses (right) for a carbon/epoxy rotor model at 20,000 RPM.

3.3.6. Numerical Modeling of an Orthotropic Two-Material Hybrid Rotor

Even though stresses in the circumferential direction are dominant during flywheel rotor rotation, considerable radial tensile stresses develop due to the mismatch in rotor growth as well as Poisson's effects. Thick wound rims tend to fail at relatively low speeds due to low radial strength of composite materials. Since filament-wound composite rotors lack reinforcement in the radial direction the rotor usually fail by delamination prior to fiber breakage in the circumferential direction [Tzeng, 2005]. In addition, thermal residual stresses developed during curing also reduce radial strength of the composite rotor. Thus, radial stress reduction is the key factor in composite rim design. As mentioned in the previous chapter, high radial tensile stresses may be mitigated, or a compression radial stress may be maintained, using a multi-ring rim design instead of single rim. One of

themost effective methods for reducing high radial tensile stresses is to fabricate the rotor from multiple rims of various materials. Manufacturing a hybrid composite rotor is also easier than implementing other techniques for radial stress reduction, such as interference fits or elastic interlayers between composite rims. Multiple concentric rings for a hybrid composite rotor can usually be produced by conventional filament winding. Thus, a hybrid composite rotor design may cost-effectively reduce radial tensile stress, overcoming the problem of low strength in that direction without reduction of hoop strength [Ha et al., 1999a]. Another advantages of the hybrid rotor design is that material cost can usually be used, which was one of tasks for this thesis project.

3.3.6.1. Model Geometry for the Two-Material Hybrid Rotor

Figure 3.3.26 shows an one-eighth rotor section used for developing a multi-material (hybrid) rotor model. Similar to previous models only a section of the full rotor was modeled using aforementioned boundary conditions. For the hybrid material setup, inner and outer radii of the rotor were again 12 cm and 24 cm with a rotor height 12 cm. The thickness for both the inner glass/epoxy rim and the outer carbon/epoxy rim was 6 cm.
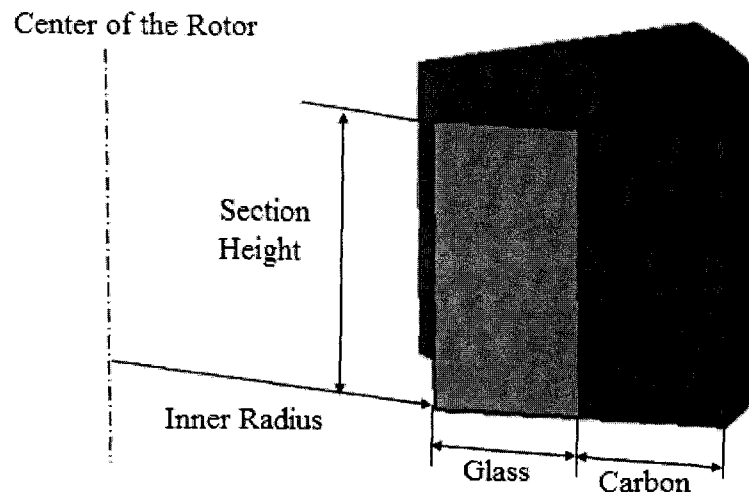
Figure 3.3.26: 45°-section multi-material flywheel rotor model.

3.3.6.2. Material Selection for the Two-Material Hybrid Rotor

For flywheel design, high strength and low density fibers are preferred [Grudkowski et al., 1995]. Unidirectional carbon/epoxy composite exhibits elastic response practically up to ultimate failure; it has high strength, low density and thermal deformation, and shows little creep or stress relaxation effects. Thus, high strength carbon fiber composites are usually the first choice for flywheel construction [Ranter et al., 2003]. Similar statements as for carbon/epoxy can generally made for properties of glass fiber/epoxy composites, however, overall glass/epoxy properties are inferior to carbon/epoxy composites. The exception is material cost that is usually significantly lower for glass fibers. Glass fibers are prone to strength degradation due to stress corrosion when subjected to moisture [DeTeresa and Groves, 2001]. But, this effect is of little concern in flywheel applications. In the present hybrid composite rotor model, the less stiff and denser glass/epoxy material was placed on the inside of the rotor to counteract the aforementioned growth mismatch. The stiffer and lighter carbon/epoxy was placed on the outside of the rotor to restrict circumferential and consequently radial deformation as much as possible.

3.3.6.3. Meshing and Boundary Conditions for the Two-Material Hybrid Rotor

As shown in Fig.3.3.27 the rotor was mapped meshed with SOLID46 elements. Initially eight elements (with a thickness of 0.75 cm per element) with six layers each were specified in the radial direction for each material rim. For each rim 512 elements with good aspect ratios were generated. Layers were oriented in the circumferential direction. The same loading and displacement boundary conditions as described in Section 3.3.3.5 were applied for the hybrid rotor model.

3.3.6.4. Results for Carbon-Glass/Epoxy Composite Hybrid Flywheel Rotor

Figure 3.3.28 shows the rotor mid-plane radial and circumferential stress distribution for the through-thickness direction. Stresses are given for a rotational speed of 20,000 RPM. Maximum tensile radial stresses for the glass/epoxy and carbon/epoxy rim were 5.2 MPa and 5.3 MPa respectively. The maximum compressive radial stress was 10.7 MPa which developed in the interface between the glass and carbon composite. Maximum hoop

stresses of 202 MPa and 395 MPa were found at the inner surface of the glass/epoxy and carbon/epoxy rim respectively. Contour plots showing radial and circumferential stress, circumferential strain and radial displacement fields are shown in Figs.3.3.29 to 3.3.32.
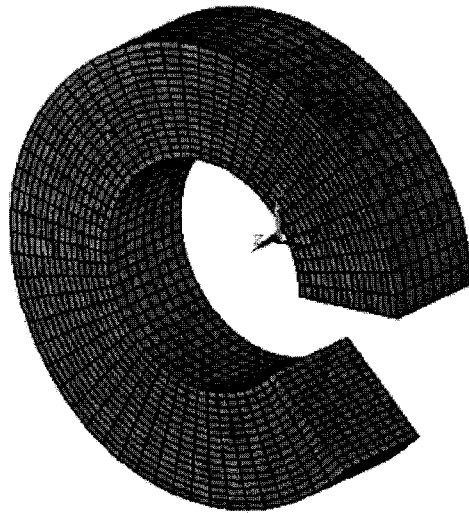
Figure 3.3.27: Mapped meshing of orthotropic multi-material flywheel rotor (45°-section with 1000 elements).
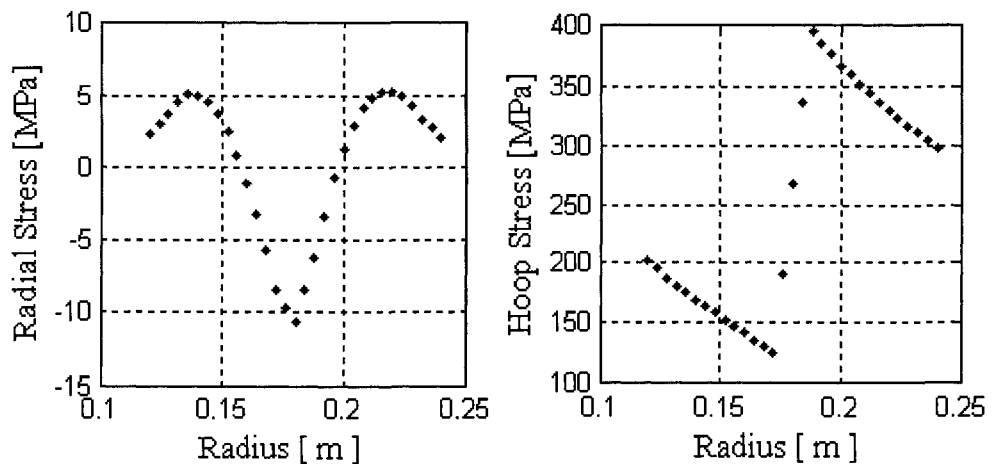
Figure 3.3.28: Mid-plane radial (left) and hoop stress profile (right) for a carbon-glass/epoxy hybrid rotor model with rotational speed of 20,000 RPM.

-.116E+08   -.762E+07   -.367E+07   284918   .424E+07
      -.959E+07   -.564E+07   -.169E+07   .226E+07   .621E+07
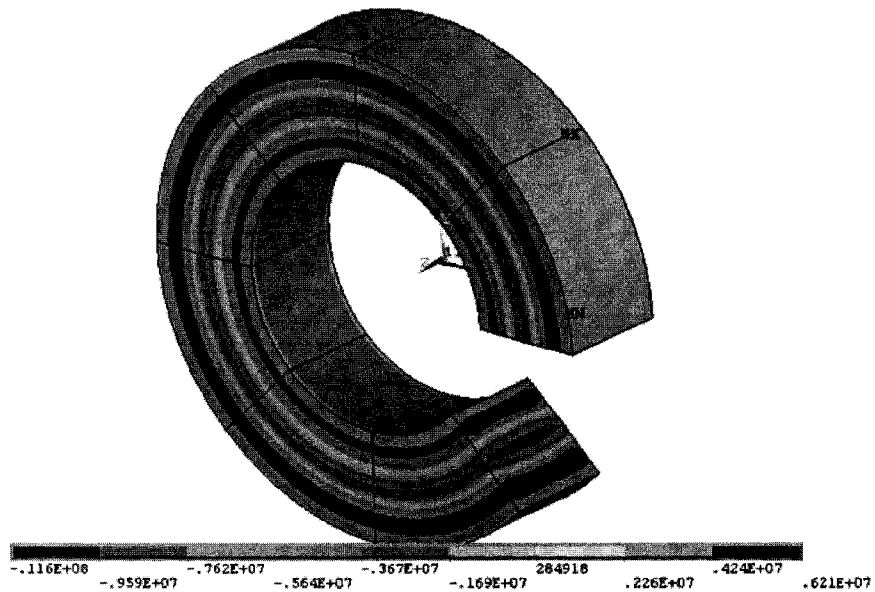
Figure 3.3.29: Radial stress field (Units: Pa) for a carbon-glass/epoxy hybrid rotor model with rotational speed of 20,000 RPM (expanded view of 45°-section with 1024 elements).

.115E+09   .182E+09   .250E+09   .318E+09   .385E+09
      .148E+09   .216E+09   .284E+09   .351E+09   .419E+09
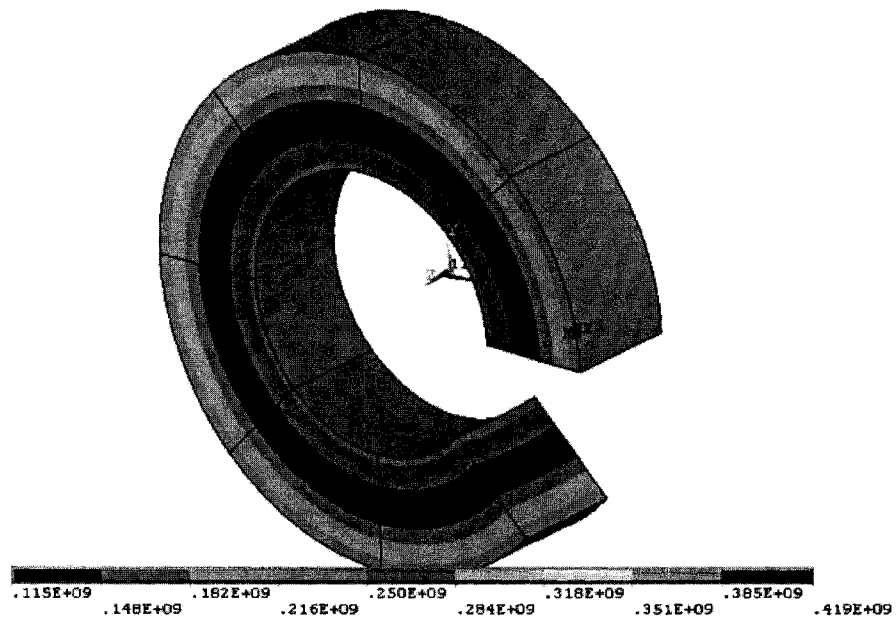
Figure 3.3.30: Hoop stresses (Units: Pa) for a carbon-glass/epoxy hybrid rotor model with rotational speed of 20,000 RPM (expanded view of 45°-section with 1024 elements).

```
.002025        .002668        .003311        .003954        .004596
      .002346        .002989        .003632        .004275        .004918
```
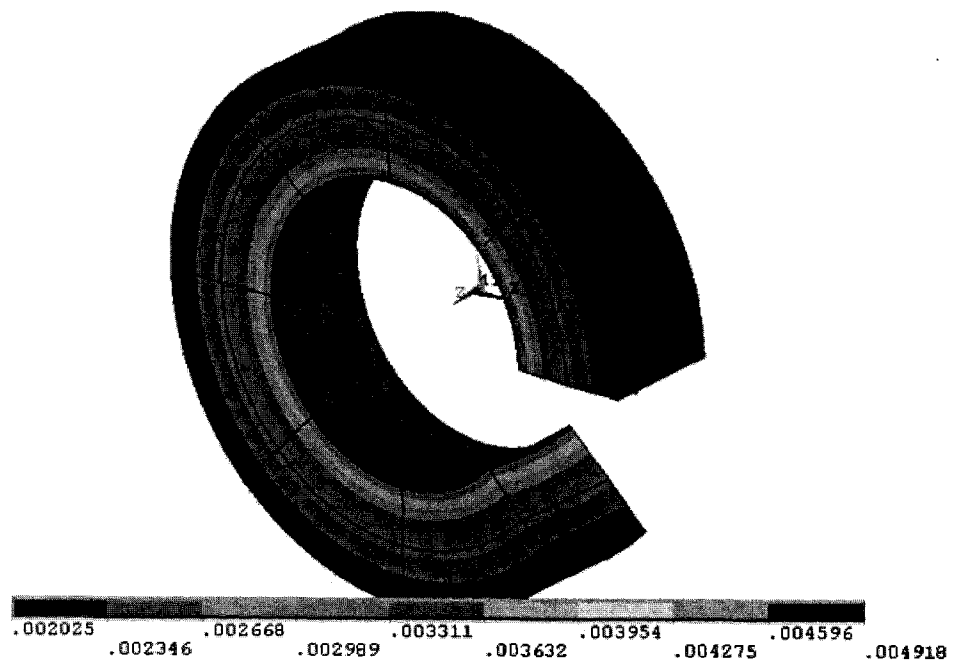
Figure 3.3.31: Hoop strains (Units: mm/mm) for a carbon-glass/epoxy rotor model with rotational speed of 20,000 RPM (expanded view of 45°-section with 1024 elements).


```
.487E-03      .511E-03      .534E-03      .557E-03      .580E-03
      .499E-03      .522E-03      .545E-03      .569E-03      .592E-03
```
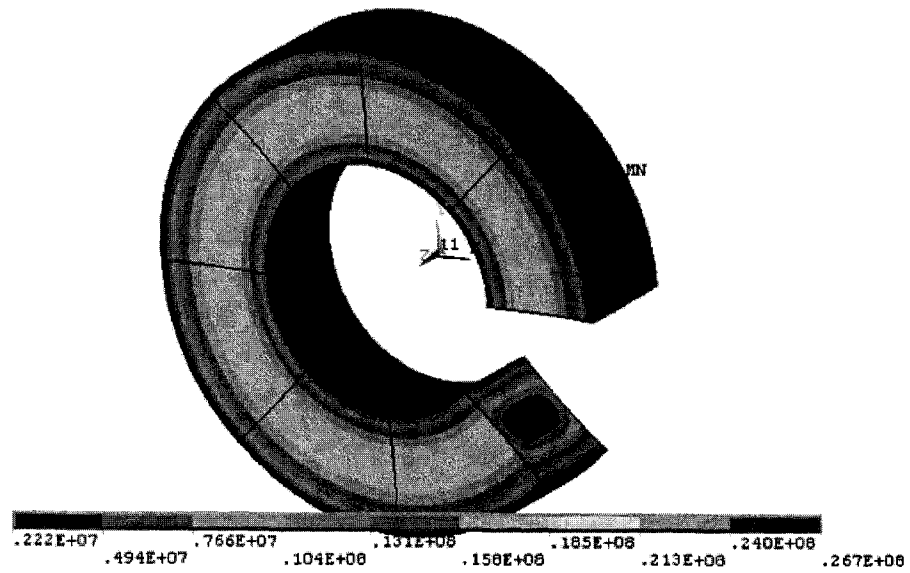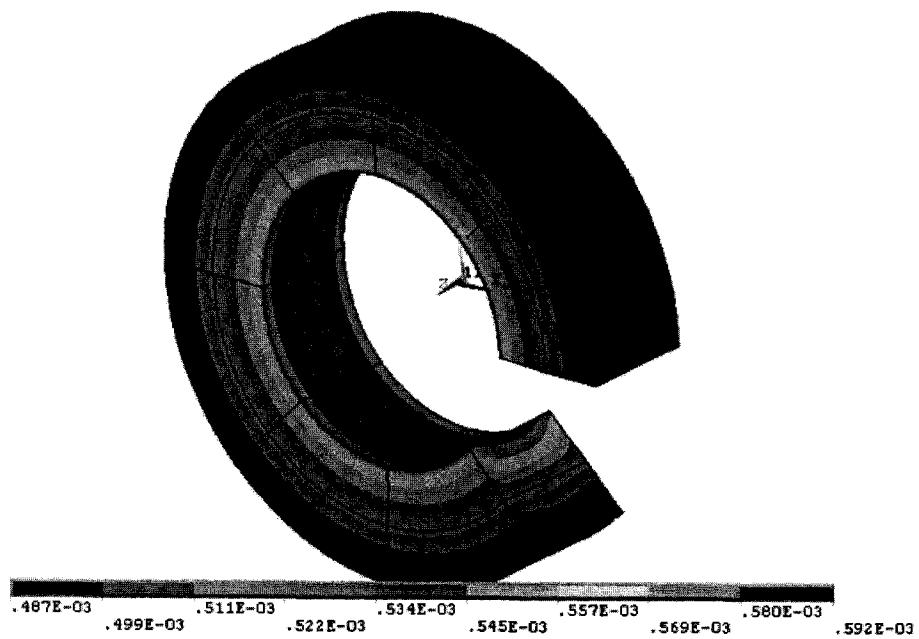
Figure 3.3.32: Radial displacement field (Units: m) for a carbon-glass/epoxy rotor with rotational speed of 20,000 RPM (expanded view of 45°-section with 1024 elements).
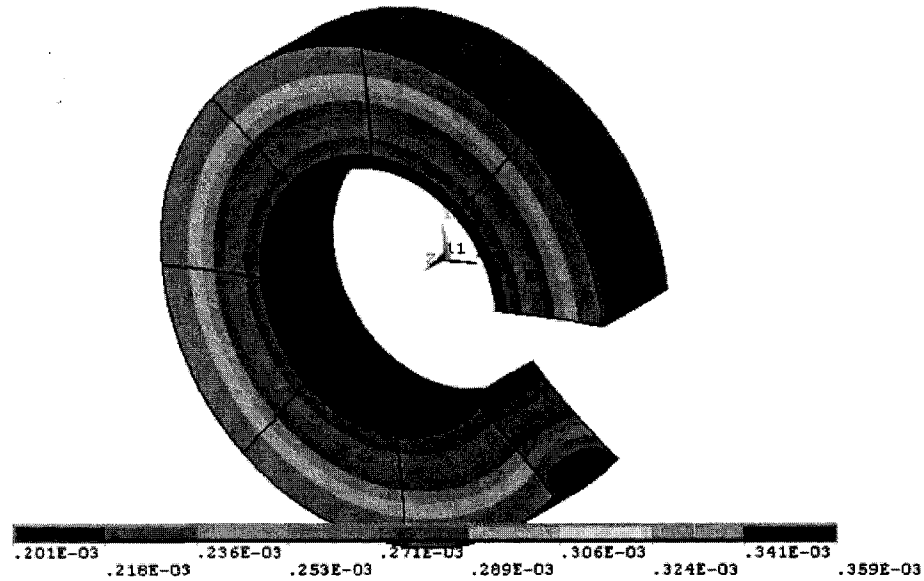
3.3.6.5. Mesh Sensitivity Analysis for the Two-Material Hybrid Rotor

A convergence test was conducted for this two-material hybrid flywheel rotor model to determine the suitable number of elements. The same FE model was analyzed with different types of mesh sizes from coarser to finer in order to determine the optimum mesh density that would yield an acceptable result in the shortest possible computational time (see Fig.3.3.33). Eleven different mesh sizes were investigated and mesh refinement continued until the variation of maximum radial stresses were less than 0.6 percent and circumferential stresses were less than 0.1 percent. It was again ascertained that radial stress was more sensitive to mesh refinement than circumferential stress. The refined mesh consisted of 3,456 elements per in 45°-section, see Fig.3.3.34.
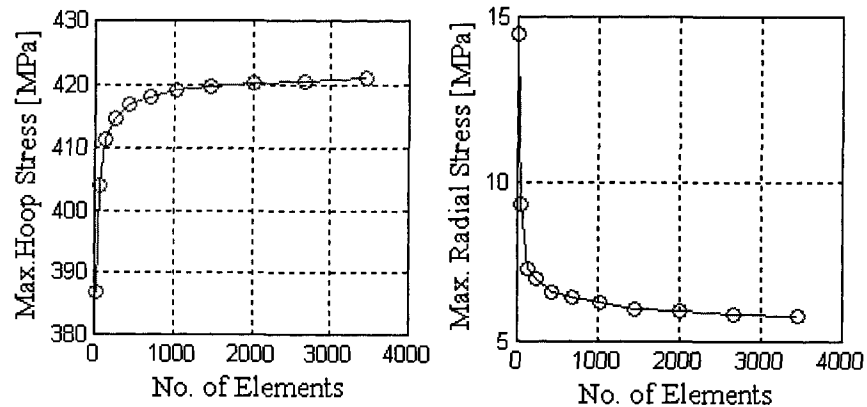
Figure 3.3.33: Variation of maximum hoop (left) and radial stresses (right) with respect to the number of elements in 45°-section under 20,000 RPM rotation
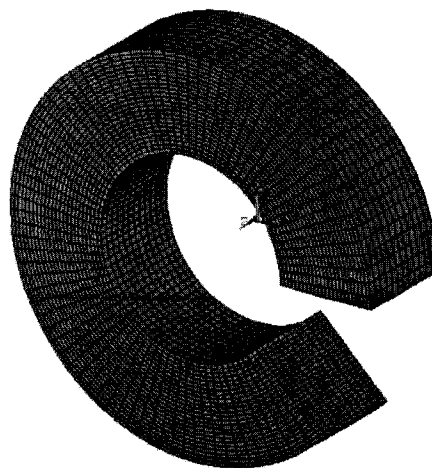
Figure 3.3.34.: Expanded view of finely meshed 45°-section model with 3,456 elements.

3.3.6.6. Model Validation for a Multi-Material Hybrid Flywheel Rotor

Previous comparisons between numerical and analytical results were limited to single-material systems. In the current section, to further validate the present modeling approach, numerical results for a multi-material hybrid material rotor model were computed and compared with corresponding results presented by Wagner (2007). In this study a specific geometry and material configuration was chosen for radial stress reduction and improved stress distribution. A five-rim hybrid composite rotor was constructed having a material sequence of glass and carbon fibers of E-glass/T300/T300/M40J/M40J with epoxy matrix. The rotor had an inner and outer radius of 125 mm and 200 mm respectively. The rim thicknesses were, from the inside outward: rim #1 (E-glass): 10mm; rim #2 (T300): 10mm; rim #3 (T300): 30mm; rim #4 (M40J): 10mm; and rim #5 (M40J): 15mm. The peripheral speed of the flywheel rotor was given as 1,250 m/sec corresponding to a rotational speed of 59,683 RPM. The kinetic energy storage capacity of the flywheel rotor was determined as 1,540 kJ corresponding to a specific kinetic energy of 418 kJ/kg.

The same rotor geometry was modeled in the present study, and data were compared to the published results. A 45°-section of the rotor geometry is shown in Fig.3.3.35. Approximate material properties were taken from the technical literature for the present model since exact properties were unknown; respective data are shown in Table 3.3.2.
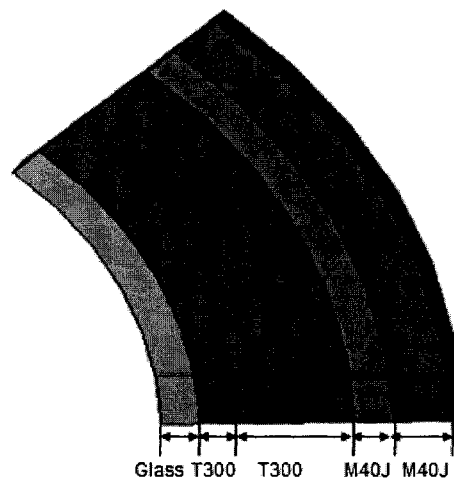
Figure 3.3.35: 45°-section model of five-ring hybrid composite flywheel rotor.

Table 3.3.2: Material properties for unidirectional fiber composites of E-glass, T300- and M40J -carbon [Daniel and Ishai, 2006; Ha and Kim, 1999a; Rupnowski et al., 2005].

	E-Glass/Epoxy Unidirectional	T300	M40J
ρ, g/cm^3	1.97	1.60	1.60
E_1, GPa	41	181	316
E_2, GPa	10.4	10.3	13.4
E_3, GPa	10.4	10.3	13.4
υ_{12}	0.28	0.28	0.22
υ_{23}	0.50	0.54	0.50
υ_{13}	0.28	0.28	0.22
G_{12}, GPa	4.3	7.17	20.8
G_{23}, GPa	3.5	3.7	3.9
G_{13}, GPa	4.3	7.17	20.8

3.3.6.7. Results and Data Comparison for Hybrid Composite Rotor Model

For the present numerical model and aforementioned study Fig.3.3.36 and 3.3.37 show radial and hoop stress distributions for the rotor through-thickness direction. The graphs indicate qualitatively good agreement between the two data sets. It is interesting to note that radial stresses remained predominately compressive for the applied rotational speed of 59,683 RPM. Even though accurate material data for the materials used was not given in [Wagner, 2007], it can be observed from Fig. 3.3.36 that radial stresses for the five composite rims were clearly below transverse strengths that are commonly reported for fiber composites, i.e. 30 to 50 MPa. From the present numerical model a maximum radial stress of 13.4 MPa was found in the T300-carbon composite rim. This value is actually higher than the value given in [Wagner, 2007], which was approximately 6 MPa. Radial stress differences were also noticeable for the M40J-composite rim. In the case of hoop stress, differences between the two data sets were less pronounced, relatively speaking.
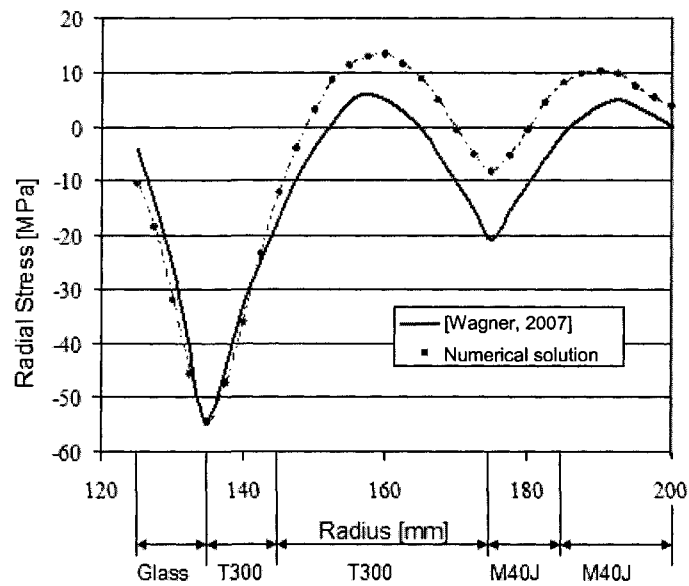
Figure 3.3.36: Radial stress distribution over radius for a 5-rim composite flywheel rotor
from numerical modeling and [Wagner, 2007].
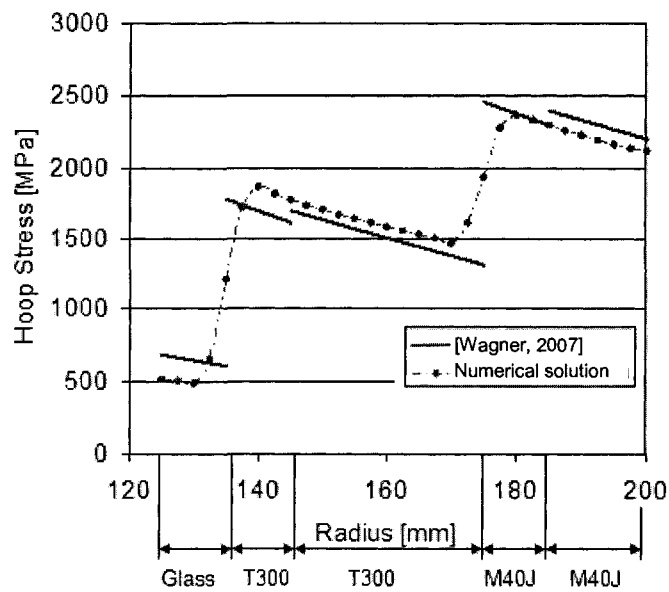
Figure 3.3.37: Hoop stress distribution over radius for a 5-rim composite flywheel rotor
from numerical modeling and [Wagner, 2007].

Differences between present numerical results and data given in [Wagner, 2007] may be due to deviations in material properties. As said above, material property for the various composite rims were not provided by Wagner (2007), and material properties for the present model were taken from various sources mentioned in Table 3.3.2. Furthermore, Fig.3.3.37 shows that hoop stresses from [Wagner, 2007] were discontinuous at the interfaces between rims of the same material; this effect was not predicted by the present model. It is unknown which method was used for determining the stress data presented in [Wagner, 2007]; yet, it reasonable to assume that stress discontinuities were caused by interference-fit effects, or by thin interface layers of a high-compliance material. Despite these differences, the specific energy for the five-rim composite flywheel model was computed as 417 kJ/kg which is almost identical to the specific energy of 418 kJ/kg given in [Wagner, 2007].

3.3.7.   Comparison of Hybrid and Single-Material Composite Rotors

To closely examine effects brought about by hybrid composite rim assemblies a comparative study was conducted applying identical loading conditions to three different rotor configurations (see Fig.3.3.38), i.e. a single-material rotor with either a glass/epoxy or carbon/epoxy rim, and a hybrid rotor with an inner glass/epoxy and outer carbon/epoxy rim. For the three models the inner rotor radius, total thickness and height all were 12 cm. Properties for circumferentially wound fiber composite materials from Table 3.3.1 and boundary conditions from Section 3.3.3.5 were applied. In the case of the hybrid rotor, glass/epoxy and carbon/epoxy composite were the materials for the inner and outer rim respectively. Both rims of the hybrid rotor had equal thickness of 6 cm.

Radial stress distributions for the three rotor configurations are shown in Fig.3.3.39. For an applied rotational speed of 10,000 RPM the peak radial stress for both single-rim rotors was located in the centre of the rotor cross-section (i.e. the plane with normal in hoop direction). Radial stresses were entirely tensile for both rotors with peak stresses of 11.8 MPa and 6.7 MPa for the glass/epoxy and carbon/epoxy rotor respectively. For the hybrid rotor, on the other hand, radial stresses were compressive for a greater part of the rotor cross-section. The maximum compressive radial stress with magnitude of 3.0 MPa

was located at the interface between the two rims of the hybrid rotor. The glass/epoxy material, having greater density and compliance than carbon/epoxy, caused compressive stresses due to relatively larger deformations. This example clearly demonstrated benefits of hybrid rotors with suitable material configuration. Compressive radial stresses that develop in hybrid rotors allow for greater rotational speeds and thus increased energy storage capacity of the flywheel rotor.
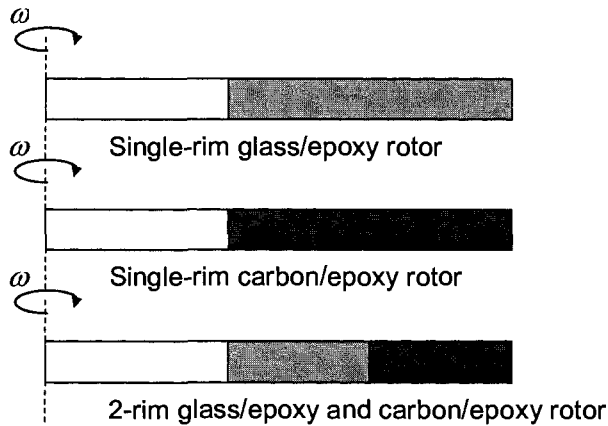
Figure 3.3.38: Schematic of single-material and two-material hybrid rotors.
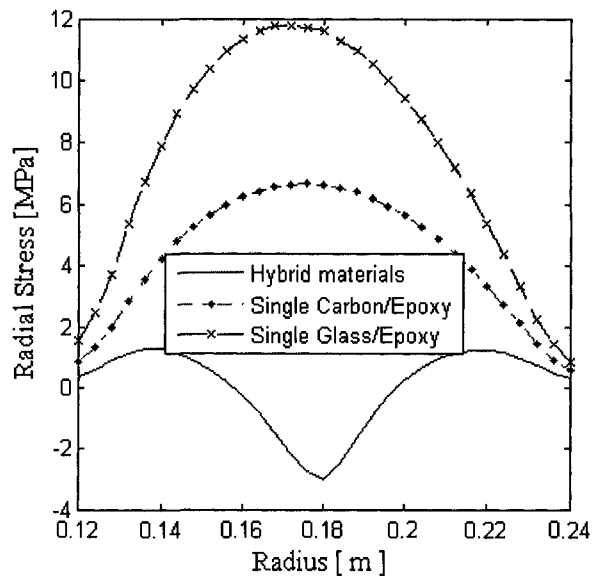
Figure 3.3.39: Comparison of radial stress distributions for single-rim glass/epoxy and carbon/epoxy rotors and a hybrid rotor with a glass/epoxy and carbon/epoxy rim for a rotational speed of 10,000 RPM.

3.4.   Interference-Fit Effect in Multi-Rim Composite Rotors

The interference-fit or press-fit joining is a mechanical retention mechanism which operates by interference of materials [Kim and Lee, 2006]. Joining between two parts is achieved by friction after the parts are mated, rather than by any other means of fastening. The friction that holds the parts together is greatly increased by compression of one part against the other. The level of compression depends on the tensile and compressive strengths of the materials that the parts are made from [Kim and Lee, 2006]. An interference-fit is generally produced by shaping the mating parts so that one or both slightly deviate in size from the nominal dimension, i.e. one part slightly 'interferes' with the space that the other is occupying. In flywheel rotor assemblies, this means that inner and outer diameters of ring components are specially dimensioned to have a slight overlap (or interference) at the interfaces (see schematic in Fig.3.4.1).
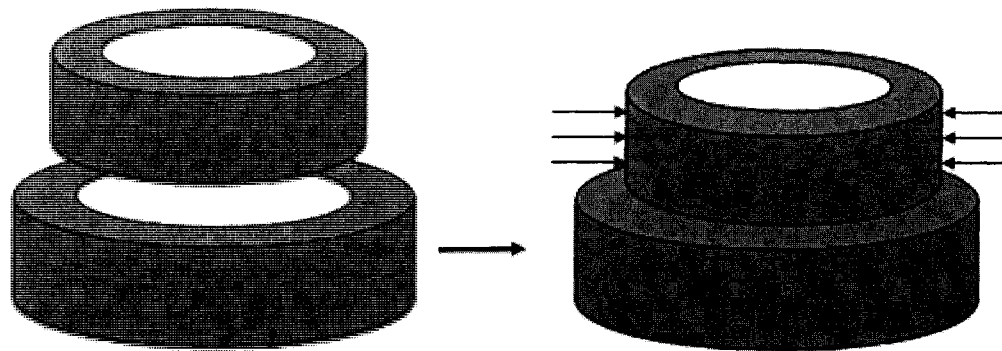
Figure 3.4.1: Schematic of interference-fit for a multi-rim flywheel rotor.

3.4.1.   Motivation for Interference-Fit Assembly of Multi-Rim Flywheel Rotors

Using interference-fit assembly for multi-rim rotors may be motivated by the following aspects. Compared to mechanical fastening and adhesive bonding, interference-fit assembly is more efficient from a weight savings view point since no fasteners and additives are required [Kim and Lee, 2006]. In addition, it is feasible to combine an interference-fit with other joining techniques, e.g. fastening and/or adhesive bonding, should Coulomb friction prevent relative motion between mating parts [Kim and Lee,

2006]. As described in the literature review in Chapter 2 an important task in composite rotor design is to maximize rotor performance by decreasing radial tensile stresses that developed due to centrifugal forces during flywheel operation. Interference-fit assembly of multi-rim rotors is among the many techniques to achieve this goal. An interference-fit may alleviate high radial tensile stresses in the rotor by superimposing compressive radial stress. In some instances compressive radial stress conditions may even be maintained up to maximum operating speed. Ranter et al. (2003) suggested assembling multi-rim rotors by press-fit, shrink-fit, or pressurizing adhesion to permit higher operating speeds. Another method for inducing residual compressive radial stresses is by pre-stressing fiber reinforcements in filament-wound rims. Fiber tension can furthermore be varied with radius or for multiple rims that can be mechanically or thermally press-fit in a nested manner [Arvin and Bakis, 2006].

3.4.2. Residual Thermal Stress Effects in Composite Rotors

Changes in temperature cause thermal effects in materials. When the thermal energy or temperature of a material increases, the vibration of its atoms and molecules increases, and this increased vibration stretches the molecular bonds thus causing the material to expand. On the other hand, if the thermal energy or the temperature of the material decreases, it will shrink or contract.

Residual stresses are stresses that remain even after the original cause of stress has been removed. In the context of composite laminates, the development of residual stresses is usually associated with laminate fabrication. On a micromechanical scale, residual stresses are introduced in unidirectional layers in and around individual fibers due to mismatches in thermal expansion properties of the constituents [Daniel and Ishai, 2006]. In addition, another kind of residual stresses called lamination residual stresses may exist on a macroscopic level, due to the thermal anisotropy of the layers and the heterogeneity of the laminate. During processing at elevated temperatures there is a certain temperature level at which the composite material is assumed to be stress free. This temperature level may be taken as the glass transition temperature of a polymer matrix, the melting temperature of a metal matrix, or the sintering temperature of a ceramic matrix. If the

thermally anisotropic plies are oriented along different directions, residual stresses develop in the initially stress-free laminate. Residual stresses are a function of many parameters, such as ply orientation and stacking sequence, curing process, fiber volume ratio, and other material and processing variables. The buildup of residual stresses and strains during the cure of composite parts can lead to cracking and dimensional tolerance problems [Gigliotti et al., 2003]. Arvin and Bakis (2006) stated that residual thermal stresses induced during the filament winding process may have a significant effect on radial tensile strength of the composite and must therefore be accounted for in the rotor design process. The mechanisms that contribute to the build up of residual stresses are mechanical, chemical, or physical in nature [Gigliotti et al., 2003]. An accurate knowledge of associated properties during the cure is therefore key to understanding the nature and development of residual stresses and strains.

In the context of interference-fit assembly of multi-rim composite rotors, residual thermal stress effects are employed to facilitate the mating of rims in a nested manner. By heating or cooling an inner or outer rim, a press-fit between the rims can be produced. The induced thermal stress depends on the coefficient of thermal expansion of the rim materials. However, many composites exhibit low thermal expansion, such as graphite fiber composites, and this method may therefore be insufficient for press-fitting [Ha et al., 2008].

3.4.3. Stress-Strain Relationship for Mechanical and Thermal Loadings

Using an analytical approach the effect of thermal loadings can be incorporated along mechanical loadings. The formulation starts with the two-dimensional stress-strain relationship under plane stress conditions for orthotropic material. Including strain terms caused by temperature change the equation for a single orthotropic ring can be written in matrix form for cylindrical coordinates as follows:

$$
\left\{ \begin{array}{c} \varepsilon_r \\ \varepsilon_\theta \end{array} \right\} = \begin{bmatrix} \dfrac{1}{E_r} & \dfrac{-v_\theta}{E_\theta} \\ \dfrac{-v_r}{E_r} & \dfrac{1}{E_\theta} \end{bmatrix} \left\{ \begin{array}{c} \sigma_r \\ \sigma_\theta \end{array} \right\} + \left\{ \begin{array}{c} \varepsilon_r \\ \varepsilon_\theta \end{array} \right\}_{\Delta T}
\qquad (3.4.1)
$$

Temperature change induces radial and hoop strains equal to:

$$\left\{ \begin{array}{c} \varepsilon_r \\ \varepsilon_\theta \end{array} \right\}_{\Delta T} = \left\{ \begin{array}{c} \alpha_r \\ \alpha_\theta \end{array} \right\} \Delta T \tag{3.4.2}$$

where α_r and α_θ are the coefficients of thermal expansion in radial and hoop directions of the orthotropic rim respectively. The change in temperature is represented by the variable ΔT.

Combining Eqs.(3.4.1) and (3.4.2) yields:

$$\left\{ \begin{array}{c} \varepsilon_r \\ \varepsilon_\theta \end{array} \right\} = \begin{bmatrix} \dfrac{1}{E_r} & \dfrac{-v_\theta}{E_\theta} \\ \dfrac{-v_r}{E_r} & \dfrac{1}{E_\theta} \end{bmatrix} \left\{ \begin{array}{c} \sigma_r \\ \sigma_\theta \end{array} \right\} + \left\{ \begin{array}{c} \alpha_r \\ \alpha_\theta \end{array} \right\} \Delta T \tag{3.4.3}$$

Equation (3.4.3) can be rearranged as follows:

$$\left\{ \begin{array}{c} \sigma_r \\ \sigma_\theta \end{array} \right\} = \begin{bmatrix} Q_{rr} & Q_{r\theta} \\ Q_{\theta r} & Q_{\theta\theta} \end{bmatrix} \left\{ \left\{ \begin{array}{c} \varepsilon_r \\ \varepsilon_\theta \end{array} \right\} - \left\{ \begin{array}{c} \alpha_r \\ \alpha_\theta \end{array} \right\} \Delta T \right\} \tag{3.4.4}$$

where Q-terms are stiffness matrix elements.

According to Eq.(3.4.4) thermal stresses arise when the flywheel rotor is exposed to change in temperature ΔT, i.e a rise or drop in temperature with respect to a reference temperature.

3.4.4.   Numerical Modeling for Composite Flywheel Rotors with Interference-Fit

3.4.4.1.   Configuration of Composite Flywheel Rotor with Interference-Fit

The same geometry and dimensions as for the hybrid two-rim composite rotor discussed in Section 3.3.6 were used to model a hybrid rotor with interference-fit. Inner rotor radius, total rotor thickness and height were all 12 cm. The inner rim and outer rim were of equal thickness (i.e. 6 cm). Two material configurations were analyzed. The first rotor model employed an inner glass/epoxy and an outer carbon/epoxy composite rim; the second model consisted of two glass/epoxy rims. Material properties were taken from Table 3.3.1; corresponding coefficients of thermal expansion are given in Table 3.4.1.

Table 3.4.1: Coefficients of thermal expansion for different composite materials [Daniel and Ishai, 2006]

Coefficient thermal expansion	E-Glass/epoxy unidirectional	Carbon/epoxy unidirectional (AS4/3501-6)
Longitudinal α_1 10^{-6}/K	7.0	-0.9
Transverse α_2 10^{-6}/K	26	27
Out of Plane α_3 10^{-6}/K	26	27

3.4.4.2. Loading Procedure

A two-stages loading procedure is usually employed for modeling interference-fit systems with thermally induced residual stress. First, a thermal analysis is performed in order to obtain initial thermal stresses. Later, the effect of temperature obtained from the thermal stress analysis is directly inputted as loading in the structural analysis to determine stresses and displacements caused by both temperature and structural loads. The initial thermal stress acts as residual stress. This is similar to coupled field analyses where the input of one field analysis depends on the results from another analysis. Coupled field analyses are a combination of analyses from different engineering disciplines that interact to solve a global engineering problem such as multi-physics analysis [ANSYS]. The ANSYS finite element software that was used for this thesis research provides two types of coupling methods. One is direct and another is the load transfer method. The direct method involves only one analysis that uses a coupled field element type containing all the necessary degrees of freedom. Coupling is handled by calculating element matrices or element load vectors that contain all the necessary terms. Load transfer methods, on the other hand, involve two or more analyses, each belonging to a different field. It is possible to couple two fields by applying the results from one analysis as loads in another analysis. However, in ANSYS there are limitations for these types of coupled field analyses, especially in terms of elements. For the composite flywheel rotor, residual thermal stresses can be applied by coupled structural-thermal analysis.

Coupling a thermal and structural analysis provides a convenient way to simulate thermal stress effects. Unfortunately, only some selected elements are available in ANSYS which allow for coupling a structural-thermal analysis. The 3-dimensional 8-node layered structural element (SOLID46) used for this model is only suited for structural fields and no such element is available for coupled structural-thermal analyses. Hence, instead of using coupled field analysis a single physics analysis, i.e. a structural analysis was performed. The element type used in this model is capable of assuming mechanical and temperature loadings simultaneously. Thus, it was possible to simulate interference-fit effects by applying temperature and inertia loads in the same structural analysis. Mechanical loads due to rotation were applied to the full solid model (solid model loads are independent of the finite element mesh). Thermal loading needed to be applied to the discrete finite element model. For reduced analysis it is recommended to directly apply loads to master nodes. After selecting nodes belonging to elements associated with a rim of a particular material, thermal load was applied. Note that thermal loading was not necessarily equal for each rim of the rotor model. In the following, a thermal load was applied in the form of a temperature change, ΔT, defined as the difference between an assumed element body temperature, T_{body}, and a global reference temperature, T_{ref}, i.e.

$$\Delta T = T_{body} - T_{ref} \qquad\qquad (3.4.5)$$

3.4.4.3. Results for a Hybrid Composite Rotor with Interference-Fit

In this section, results are presented for a hybrid composite rotor with an inner glass/epoxy and an outer carbon/epoxy composite rim. Circumferential and radial stress distributions obtained from present numerical model are shown in Fig.3.4.2. Stress data were taken along the thickness-direction from the rotor mid-plane. As described in the preceding section, a thermally induced press-fit was simulated by applying a thermal load to the model. This thermal load was applied in the form of a temperature change ΔT of 80 K that was applied to both rims (e.g. a body and reference temperature of 100°C and 20°C respectively). Contour plots presented in Figs.3.4.3 and 3.4.4 show the entire radial and circumferential stress field for this rotor model.
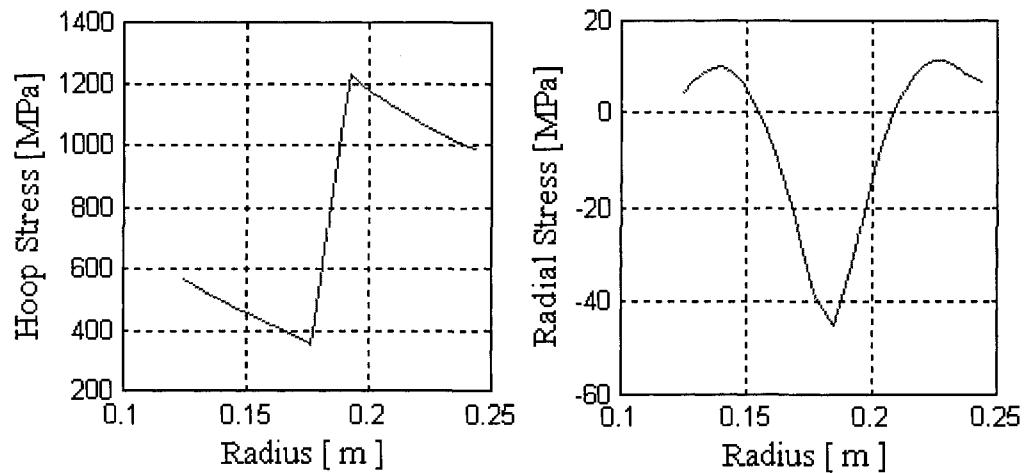
Figure 3.4.2: Mid-plane hoop stress (left) and radial stress profile (right) for a hybrid rotor with an inner glass/epoxy and an outer carbon/epoxy composite rim. A rotational speed of 35,000 RPM and temperature change in both rims of 80 K were applied as mechanical and thermal loading. (45°-section model with 1024 elements).

From Figs.3.4.2 to 3.4.4 it can be observed that radial stresses were largely compressive in this two-material hybrid rotor with press-fit. The magnitudes of maximum compressive and tensile radial stress were 45.0 MPa and 10.1 MPa respectively. Maximum compression stress developed in interface region between the two rims; maximum tensile stresses were located in the middle of each rim. A maximum hoop stress of 1126 MPa was found in the carbon/epoxy rim close to interface region of the two materials. For the glass/epoxy rim the maximum hoop stress of 565 MPa was at the rotor inner radius.

To clearly observe the effect press-fit assembly, the model was solved for two additional loading cases, and results in terms in radial and circumferential stress were compared. The three loading cases considered in the following are:

(a) No thermal loading to simulate press-fit. Rotational speed of 35,000 RPM;

(b) Equal thermal loading to both rims corresponding to a temperature change of 80 K to simulate press-fit. Rotational speed of 35,000 RPM (equal to model (a));

(c) Equal thermal loading to both rims corresponding to a temperature change of 80 K to simulate press-fit. No mechanical loading.

-.469E+08   -.334E+08   -.199E+08   -.641E+07   .709E+07
      -.402E+08   -.267E+08   -.132E+08   337772   .138E+08
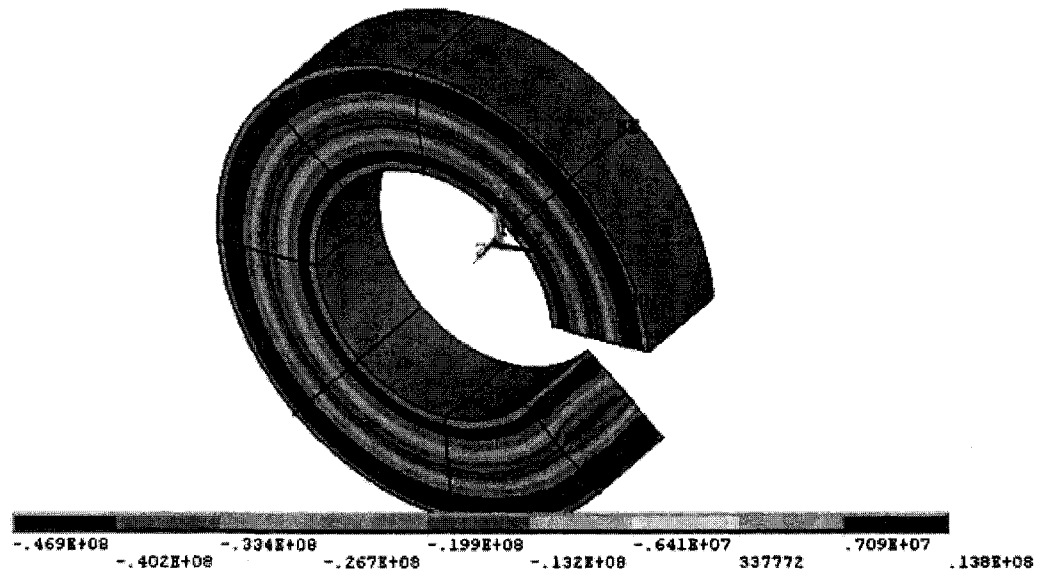
Figure 3.4.3: Radial stresses (Units: Pa) for a carbon-glass/epoxy hybrid rotor model.
A rotational speed of 35,000 RPM and temperature change in both rims of 80 K
were applied as mechanical and thermal loading. (expanded view of 45°-section
with 1024 elements).

.325E+09   .540E+09   .755E+09   .970E+09   .119E+10
      .433E+09   .648E+09   .863E+09   .108E+10   .129E+10
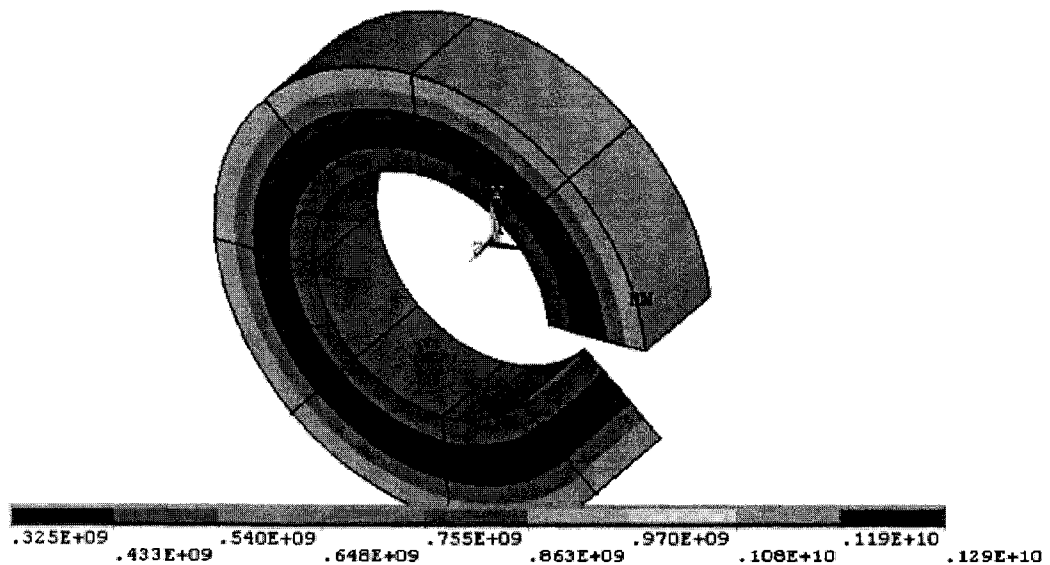
Figure 3.4.4: Hoop stress field (Units: Pa) for a carbon-glass/epoxy hybrid rotor model.
A rotational speed of 35,000 RPM and temperature change in both rims of 80 K
were applied as mechanical and thermal loading. (expanded view of 45°-section
with 1024 elements).

From Fig.3.4.5 it can be seen that for both rotor models with mechanical loading, radial stress maxima were located in the centre of the inner glass/epoxy rim and the outer carbon/epoxy rim. Peak values for the glass/epoxy and carbon/epoxy rim were 10.1 MPa and 11.4 MPa for the model with interference-fit, which is considerably less than corresponding peak radial stresses of 15.9 MPa and 16.1 MPa for the model without interference-fit. From the radial stress profile for the model without mechanical loading and interference-fit it was found that the magnitude of maximum compressive thermal stress was 12.2 MPa which developed in the interface between the two rims. At the location where peak radial stresses occurred in the glass/epoxy rims with mechanical loading, radial compressive stress that developed solely due to temperature effects was 5.8 MPa. (This value is equal to the difference between the peak radial stresses for the model with and without interference-fit at this location.) These results demonstrate the effectiveness of interference-fit assembly to significantly reduce radial stress. Figure.3.4.6 shows corresponding radial strain profiles for the three loading configurations. It can be observed that for all three cases radial strains were negative indicating the reduction of rim and total rotor thicknesses.

Hoop stress and strain profiles for the three loading cases are shown in Figs.3.4.7 and 3.4.8 respectively. From these figures it can be observed that for thermally induced hoop stresses and strains were compressive in the glass/epoxy rim and tensile in the carbon/epoxy rim. For the models subjected to mechanical loading, maximum hoop stresses for the glass/epoxy and the carbon/epoxy rim were located at the inner radius of each rim. Hoop stresses in the carbon/epoxy rim were overall greater in the model with interference-fit than in the model without. The opposite is true for the glass/epoxy rim. For example, the peak hoop stress in the glass/epoxy rim was 565 MPa with interference-fit, which was less than the maximum hoop stress of 620 MPa for the model without press-fit. These data demonstrate how the introduction of an interference-fit caused a reduction of circumferential stresses in the inner glass/epoxy rim while increased stresses resulted in the outer carbon/epoxy rim.
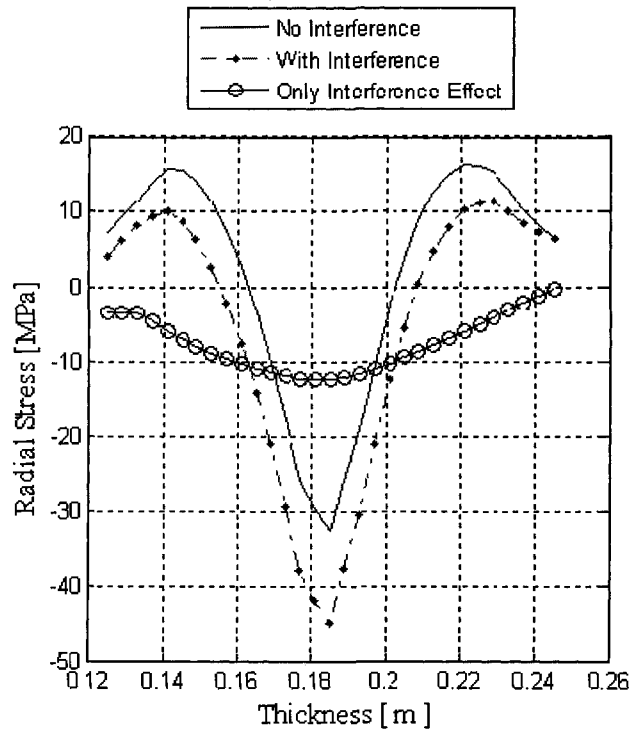
Figure 3.4.5: Interference-fit effect on radial stress for a hybrid composite rotor model.
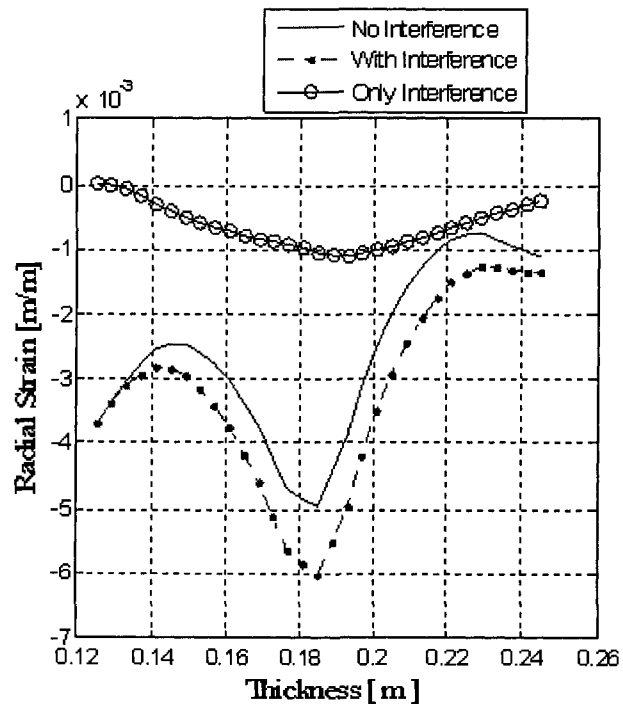
Figure 3.4.6: Interference-fit effect on radial strain for a hybrid composite rotor model.
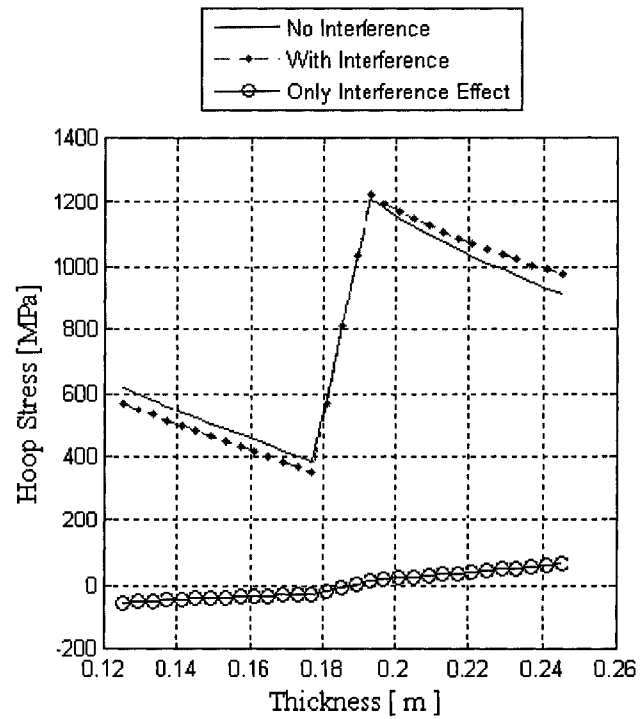
Figure 3.4.7: Interference-fit effect on hoop stress for a hybrid composite rotor model.
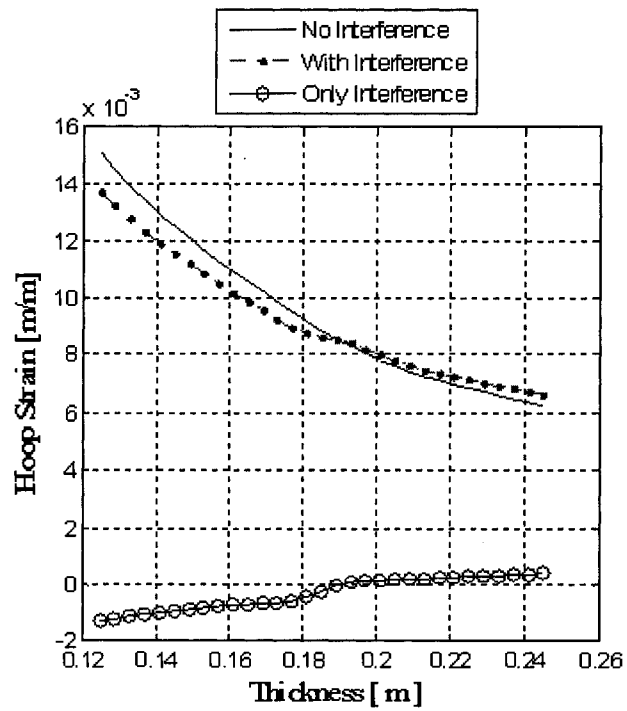
Figure 3.4.8: Interference-fit effect on hoop strain for a hybrid composite rotor model.

3.4.4.4. Results for a Two-Rim Glass/Epoxy Composite Rotor with Interference-Fit

To gain further insight into effects of interference-fit assembly on rotor performance, an additional two-rim model was investigated. In contrast to the previous analysis, both rims in the present model were of the same glass/epoxy composite material. The following loadings were applied:

(a) No thermal loading to simulate press-fit. Rotational speed of 15,000 RPM;

(b) Thermal loading to the inner rim corresponding to a temperature change of 80 K to simulate press-fit (outer rim maintained reference temperature). Rotational speed of 15,000 RPM (equal to model (a));

(c) Thermal loading to the inner rim corresponding to a temperature change of 80 K to simulate press-fit (outer rim maintained reference temperature). No mechanical loading.

Figure 3.4.9 shows that for the rotor with mechanical and thermal loading the maximum radial stress in this rotor was 21 MPa, which is considerably less than the corresponding stress of 26.8 MPa that developed when no thermal loading was applied. In both cases, peak radial stress was located near the interface between the tow rims. Hoop stresses reached their maximum at the inner rotor radius and their minimum at the outer rotor radius, irrespective of interference-fit effects, see Fig.3.4.10. Yet, the presence of a press-fit reduced the peak hoop stress since superimposed thermal stress for the circumferential direction was compressive for the inner rim and tensile for the outer rim.

3.4.5. Limitations of Interference-Fit Assembly

Interference-fit assembly of composite flywheel rotors using two or more rims of different materials may have detrimental effects [Gabrys, 2003]. Differences in coefficients of thermal expansion and elastic properties may cause rims to contract differently upon cooling. In addition, the resin matrix usually undergoes considerably larger shrinkage during cooling than the reinforcement phase. Hence, matrix cracking may occur caused by high residual stresses. Hence, the manufacture of interference-fit hybrid composite rotors requires careful analysis and planning to avoid crack development in the rotor.
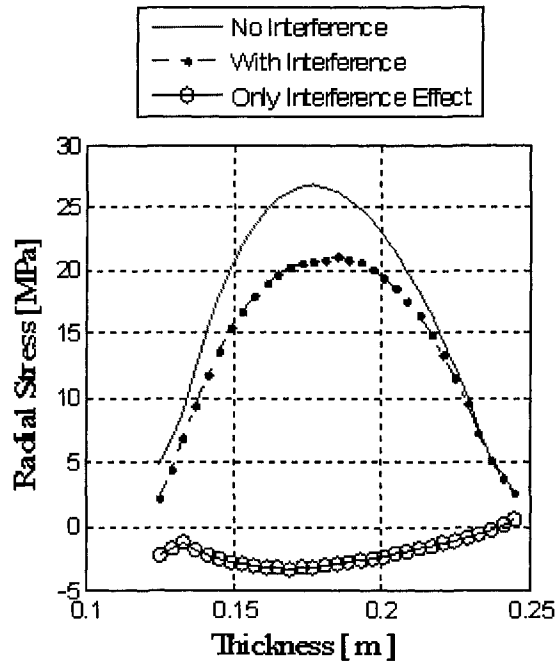
Figure 3.4.9: Press-fit effect on radial stress for a two-rim glass/epoxy composite rotor model.
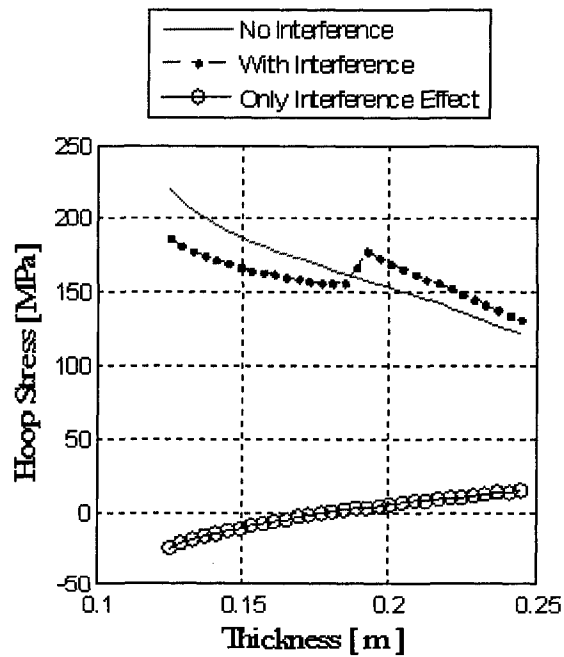
Figure 3.4.10: Interference-fit effect on hoop stress for a two-rim single-material composite rotor model.

3.5.   Design of a Hub for Composite Flywheel Rotors

3.5.1   Design Considerations for a Flywheel Rotor Hub

The rotor system of an energy-storage flywheel is usually supported by frictionless bearings such as magnetic bearings. A shaft attached to the bearings is connected to the rotor of composite materials via a hub. The hub also has the function to transmit torque between the rotor and the motor/generator unit that may be attached to either the shaft or the hub directly. Being of considerably greater diameter the rotor stores most of the kinetic energy. Thus, the hub needs to establish a connection between the large-diameter rotor and the smaller shaft and motor/generator unit. [Ha and Kim, 2006]. This is the main reason for the development of high stresses in the hub which may reduce the possible maximum speed and hence the energy storage capability of the flywheel [Gabrys, 2003]. Even though high strength, high stiffness and light-weight fiber-reinforced composite materials have predominately been used for high speed rotors, the rotor tends to detach from the metallic hub which is usually much stiffer than the composite rotor in its radial (transverse-to-fiber) direction [Ha and Kim, 2006]. Consequently, the attachment of hub and composite rotor has emerged as one of the main challenges in flywheel design.

During the design phase of a flywheel rotor hub, various factors have to be considered. One of them is radial incompatibility, i.e. during flywheel operation the rotor structure grows radially, potentially causing separation between the hub and the rotor structure if the latter consists of high-strength, yet moderately low modulus materials [Flanagan and Wong, 1989]. Thus, the hub should be designed in such a way as to always stay in contact with the rotor during high speed operation. To overcome this problem Flanagan and Wong (1989) suggested composing the rotor structure from a large number of thin rims interfaced with PTFE (Teflon®) membrane. However, this option is rather costly and results in poor volumetric efficiencies and therefore cannot be used for thick ring rotor designs [Flanagan and Wong, 1989]. In addition, since flywheels must operate at high speeds in order to obtain maximum kinetic energy, a high density hub material is prone to fail structurally under these loading conditions [Flanagan and Wong, 1989].

3.5.2. Geometry for Flywheel Rotor Hub Model

Using a particular hybrid composite rotor design with metallic (isotropic) hub, the effects of the hub during flywheel operation were investigated. The aim of the hub design was to allow for the integration of rotor, shaft and motor/generator unit, and safe operation during high speed rotation. Figure 3.5.1 shows the rotor/hub assembly. Due to the symmetric nature of loading and geometry, only a one-eighth (45°) section of the full rotor/hub assembly was modeled (shown in Fig.3.5.2) using appropriate boundary conditions. The hub body featured a center bore with radius $d_I = 2$ cm and 8 identical bores with radius $h = 1.5$ cm. The latter were equally spaced along the circumference of a circle with radius $d_2 = 7.5$ cm. The bores were incorporated into the hub design to allow for the attachment of a shaft and motor/generator unit to the hub. The outer radius of the hub was $a + a_I = 12$ cm where $a = 11$ cm. The hub web and total rotor height were $l_I = 4$ cm and $l_I + l_2 = 8$ cm respectively. Attached to the hub were two composite rims, both having a thickness of $t_I = t_2 = 6$ cm.
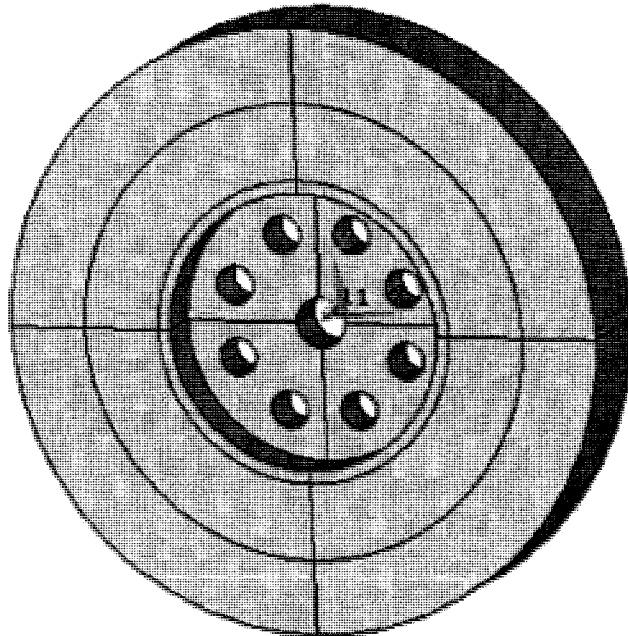
Figure 3.5.1: Model of two-rim flywheel rotor with hub.
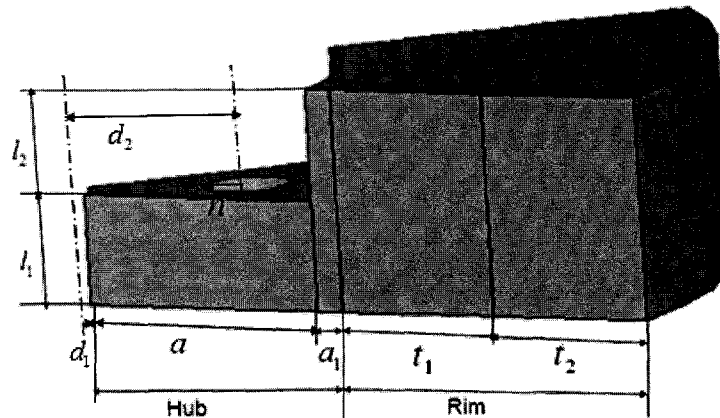
Figure 3.5.2: 45°-section of hybrid rotor and hub assembly

showing geometry parameters and coordinates.

3.5.3.   Material Selection for Flywheel Rotor Hub Model

During flywheel rotation the hub needs to expand according to the deformation of the composite rims, i.e. a compressive contact stress at the hub-rim interface is required to prevent separation [Takahashi et al., 2002]. Thus, for the selection a hub material consideration should be given to materials with the following characteristics: (a) high strain of failure, (b) low modulus of elasticity, and (c) stable deformation behavior up to high strain levels allowing for a precise prediction of the deformation field.

Glass fiber composites have high strain of failure and low moduli of elasticity facilitating hub expansion during high speed rotation. However, these materials are generally not used in rotor hub designs since they are easily damaged by delamination and fiber/matrix debonding even at low rotational speeds; the deformation behavior of glass fiber composite hubs is therefore unstable [Takahashi et al., 2002]. High strength aluminum alloys have adequate ultimate strength and low modulus. Deformation is stable and during high speed rotation strains within the aluminum alloy hub may grow beyond the elastic region. High strength aluminum alloys are therefore the first choice for hub materials [Takahashi et al., 2002]. In the present analysis an aluminum material was also selected for the rotor hub. Similar to previous analyses, the rotor's inner and outer rim were composed of glass/epoxy and carbon/epoxy composite material respectively. Associated material properties were presented in Table 3.3.1.

3.5.4. Finite Element Modeling of Flywheel Rotor Hub

A suitable finite element modeling strategy was required to efficiently model to the flywheel rotor assembly consisting of an isotropic hub and two hybrid composite rims. As described in Section 3.3.3.3, the 3-dimensional 8-node structural solid element SOLID45 was used for the modeling of the isotropic rotor components. A layered version of this element type, SOLID46, was employed for composite rotor components.

Mapped meshing was used for the rims and also for the outer section of the hub. However, meshing of the hub web posed some challenges since the bore features resulted in irregular shaped elements. To avoid model inaccuracies the hub web was divided into six sections around the bore enforcing regular shaped mapped meshing in that region (see Fig.3.5.3). A high mesh density was imposed on hub web, i.e. eight element divisions were specified for each of the hub web sections' boundary lines. This resulted in 4,096 elements for the hub web. Note that node connectivity was ensured for the described hub and rotor elements. A sensitivity analysis was performed to optimize mesh density for adequate accuracy and reasonable computing effort. Shown in Figs.3.5.4 and 3.5.5 the final finite element mesh for the 45°-section rotor model consisted of 13,312 elements.
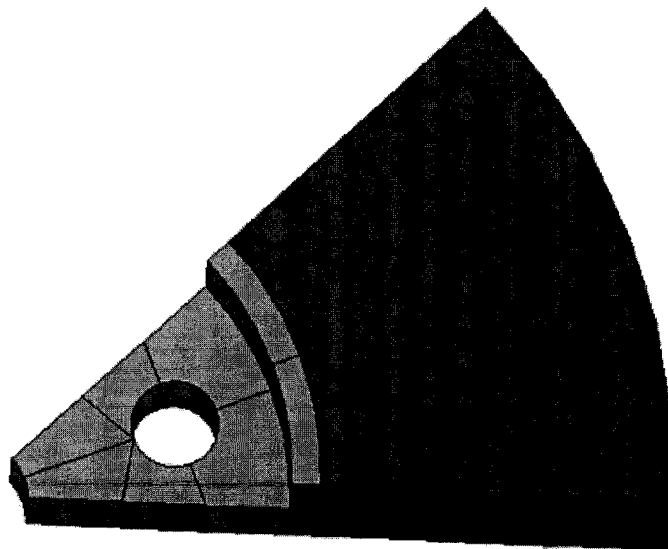
Figure 3.5.3: 45°-section model of flywheel rotor with hub showing 6 hub web sections for the enforcement of regular mapped meshing.
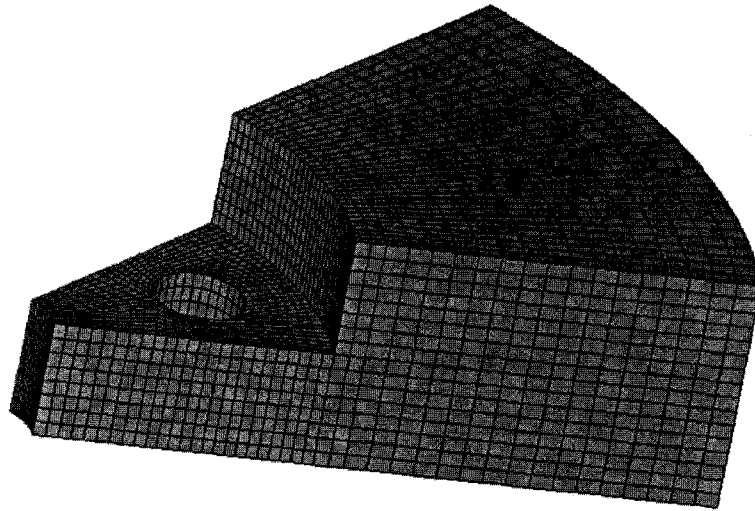
Figure 3.5.4: Finite element mesh for 45°-section model of flywheel rotor with hub.
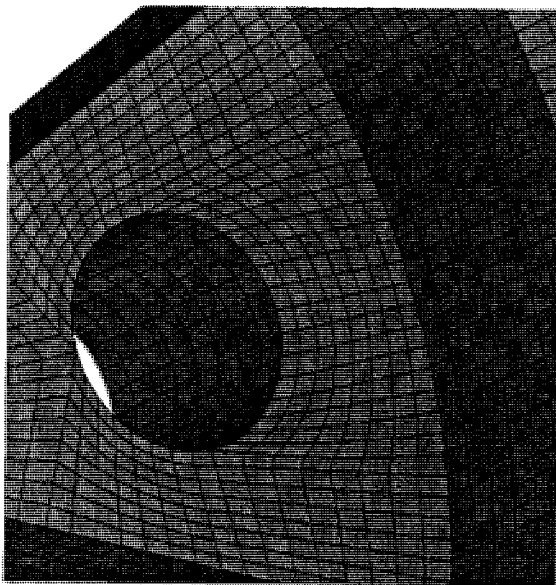
Figure 3.5.5: Close-up of finite element mesh for hub web.

3.5.5.   Result for Flywheel Rotor Model with Composite Rims and Metallic Hub

A rotational speed of 20,000 RPM was applied to the flywheel rotor model with composite rims and aluminum hub. Radial, hoop, and equivalent (von Mises) stress fields are shown in Figs.3.5.6 to 3.5.8 respectively. Radial stresses within the composite rims were almost entirely compressive. The exception is the region near the hub web indicating an insufficiently compliance of the aluminum hub. The maximum hoop stress in the composite rims was 357 MPa that developed in the carbon/epoxy rim adjacent to the glass/epoxy rim. In contrast to previous hybrid rotor models (see e.g. Fig.3.3.30) hoop stresses in the composite rims were not uniform along the axial direction. From Fig.3.5.9 it can be observed that due to the presence of the hub also radial displacements of the rotor were no longer uniform. In the hub a peak equivalent stress of 424 MPa was recorded, which occurred along the perimeter of the bores. This data indicates that the hub is likely to fail in that region should higher rotational speeds be applied.
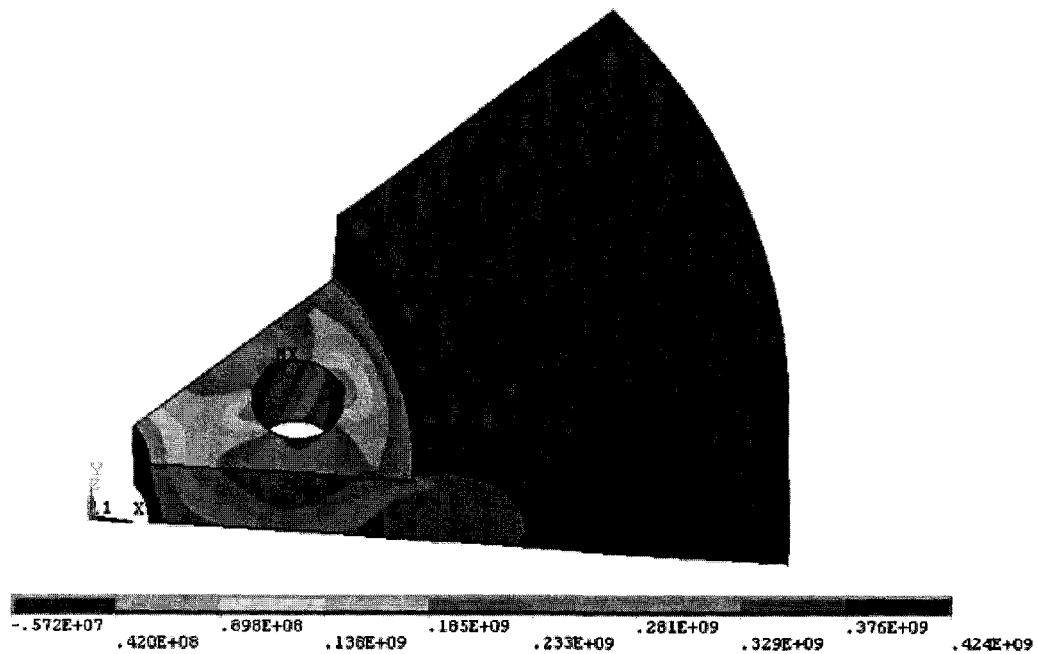
Figure 3.5.6: Radial stress distribution (Units: Pa) for a 45°-section model of a hybrid composite rotor with aluminum hub for a rotational speed of 20,000 RPM.

.723E+07   .107E+09   .207E+09   .307E+09   .407E+09
      .572E+08   .157E+09   .257E+09   .357E+09   .457E+09
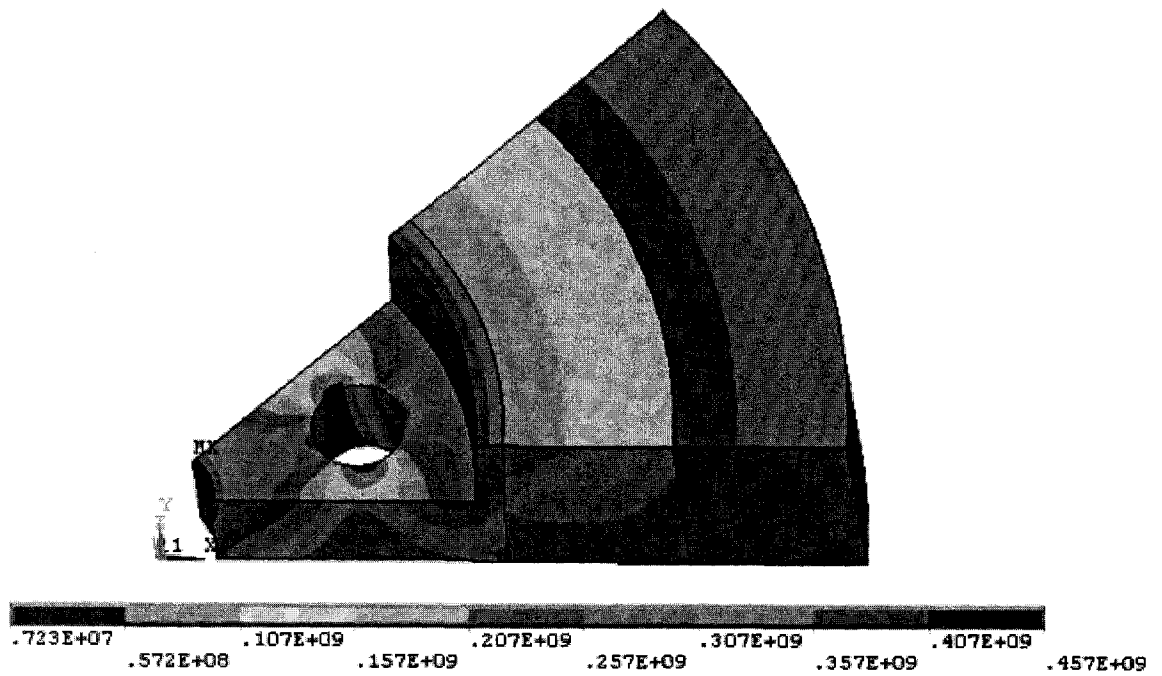
Figure 3.5.7: Hoop stress distribution (Units: Pa) for a 45°-section model of a hybrid

composite rotor with aluminum hub for a rotational speed of 20,000 RPM.

.452E+08   .131E+09   .218E+09   .304E+09   .390E+09
      .883E+08   .174E+09   .261E+09   .347E+09   .433E+09
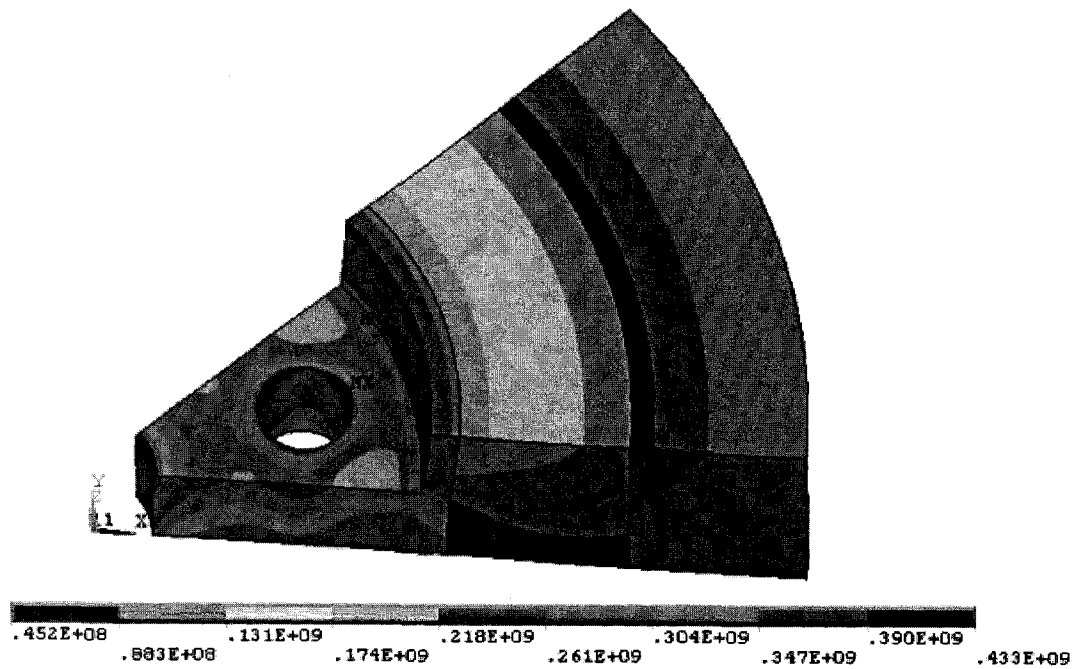
Figure 3.5.8: Von Mises stress distribution (Units: Pa) for a 45°-section model of a

hybrid composite rotor with aluminum hub for a rotational speed of 20,000 RPM.

```
.564E-04          .172E-03         .289E-03          .405E-03          .521E-03
       .114E-03          .230E-03          .347E-03          .463E-03          .579E-03
```
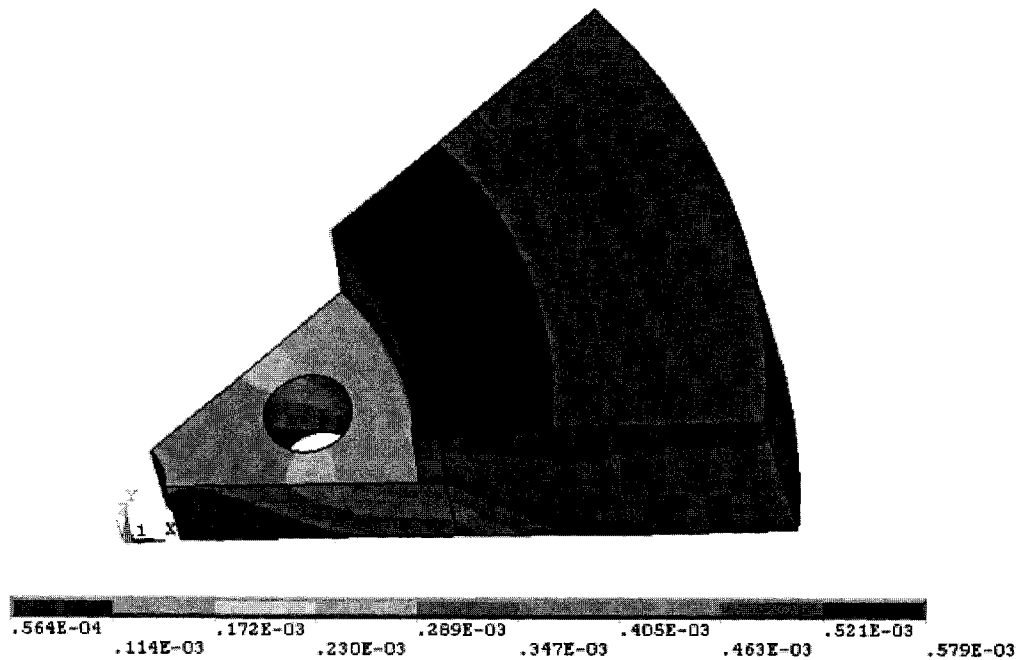
Figure 3.5.9: Radial displacements (Units: m) for a 45°-section model of a hybrid composite rotor with aluminum hub for a rotational speed of 20,000 RPM.

3.5.6.   Result for Flywheel Hub Model without Composite Rims

To better understand the effect of rotational loading on the aluminum hub an additional model was developed in which only the hub was subjected to a rotational speed of 20,000 RPM. Figure 3.5.10 shows the stress field for Von Mises equivalent stress for the aluminum hub. Quantitatively, a similar stress distribution can be observed as shown in Fig.3.5.8 for the full rotor consisting of composite rims and hub. However, overall equivalent stress levels were lower for the hub without rims. The maximum equivalent stress of 184 MPa developed along the perimeter of the centre bore, which was considerably less than the maximum equivalent stress of 424 MPa recorded for the hub with attached composite rims. Based on the data presented for the hub alone, failure of this component is unlikely for the given loading. Consequently, even though it is initially convenient to investigate and optimize rotor performance using the rotor rims only, the final design of the rotor assembly cannot be based on an analysis of its individual components alone; this is particularly the case for the hub.
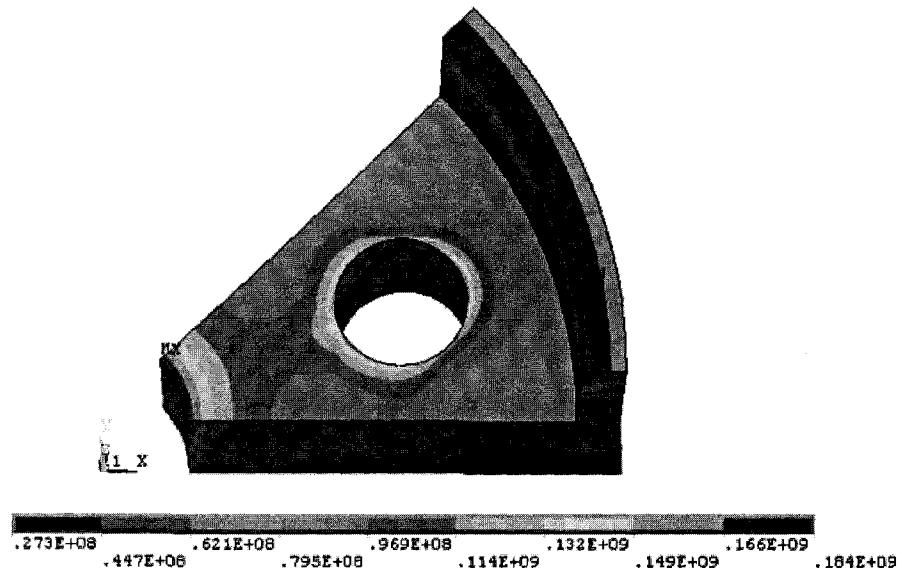
Figure 3.5.10: Von Mises stress distribution (Units: Pa) for a 45°-section model of an

aluminum hub for a rotational speed of 20,000 RPM

CHAPTER 4

OPTIMIZATION OF FLYWHEEL PERFORMANCE

4.1. Overview of Optimization Techniques

Optimization is concerned with achieving the best outcome for a given operation or process while satisfying certain restrictions. It involves making best decisions in solving a problem or arranging a system [Haftka, 1992]. Design optimization is the engineering process that delivers the highest performance of parts or assemblies with the least material weight, the smallest net volume, or the highest strength. Designs provided by this process constitute the extreme in performance or cost efficiency. Generally, engineering design optimization is an improvement of a proposed design that results in the best properties for minimum cost. Structural optimization is a relatively new field undergoing rapid changes in methods and focus. But, due to challenges in automotive, aerospace, civil and other engineering applications, research in structural optimization is increasingly been driven by real-life problems [Haftka, 1992].

4.1.1. Nonlinear Programming (NLP)

Most problems in structural optimization can usually be formulated as nonlinear constrained minimization problems. In nonlinear programming a system of equalities and inequalities, collectively termed constraints, is solved over a set of unknown real variables, along with an objective function which is to be maximized or minimized. In this process, some of the constraints or the objective functions are nonlinear [Winston, 2004]. From the following examples, a general idea about the process of nonlinear programming can be gathered.

Suppose an objective function $f(x,y)$ is to be maximized or minimized. This process is subject to the constraint $g(x,y) = c$, where $c = constant$. The contour of f can be visualized by $f(x,y) = d_n$ for various values of d_n. The contour of g is $g(x,y) = c$. At the maximum the gradient of f and gradient of g are parallel, i.e. $\nabla f(x,y) \parallel \nabla g(x,y)$, see Fig.4.1.
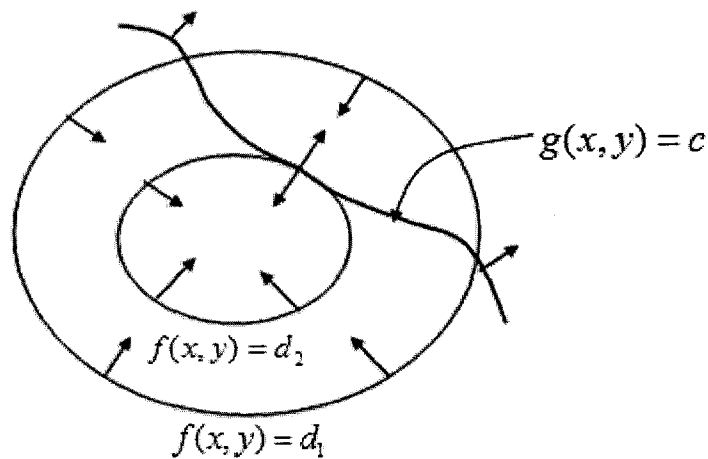
Figure 4.1: Illustration of nonlinear optimization procedure.

The maximum may then be found by solving $\nabla[f(x,y) - \lambda(g(x,y) - c)] = 0$ for $\lambda \neq 0$, where the new unconstrained function is $F(x,y,\lambda) = f(x,y) - \lambda(g(x,y) - c)$. $F(x,y,\lambda) = f(x,y)$ satisfies the constraint for all (x,y) because $g(x,y) - c$ is equal to zero on that constraint. So, the constrained optimization problem is reduced to an unconstrained optimization problem for the function $F(x,y,\lambda)$ where λ is a Lagrange multiplier. In mathematical optimization problems, the method of Lagrange multipliers is the method of finding the extrema of a function of several variables subject to one or more constraints, which is the basic tool in nonlinear constrained optimization [Arfken, 1985].

4.2.   Optimization in Finite Element Analysis

Optimization is more difficult in finite element analysis since each design variation requires a significant amount of time to evaluate, which generally makes brute-force iterative optimization prohibitively time consuming. The analysis usually involves nonlinear optimization under both equality and inequality constraints. Using suitable analysis software a design space is created based on a small set of design variations, to which curves are fit to the relationship between the degrees of freedom, and the properties of the optimization function and properties to be constrained. The design space

is subsequently searched for an optimal design point, which may act as a starting point for subsequent runs [Budgell, 1998]. Currently, various commercial finite element packages are available that have optimization capabilities built in. The finite element software ANSYS used in this numerical study has the capability of design optimization. In fact, any items that can be expressed in ANSYS in terms of parameters are candidates for design optimization parameters, e.g. weight, surface area and volume [ANSYS]. ANSYS optimization procedures are suitable for any analysis and simulation type. It has the capability to accept predefined variables with analytical constraints, and it is well suited for structural optimization since geometric dimension, loadings and boundary conditions may be expressed as parameterized design variables and objective functions.

4.3.   Numerical   Optimization   Scheme   Employed   for   Hybrid   Composite Flywheel Rotor Model

The objective of flywheel rotor optimization was to maximize specific kinetic energy, E_{kin}/M, or kinetic energy per unit cost, $E_{kin}/Cost$, within the constraints of material strengths. Maximum stress failure theory was used as failure criteria for the optimization process. To ensure rotor loading below material failure, strength factors SF calculated at any point of the rotor must satisfy the condition $SF \geq 1$. A strength factor SF is defined as the quotient of ultimate strength and applied stress [Kaw, 2006]. Various parameters pertaining to the operation of hybrid composite flywheel rotors may be taken into account for maximizing aforementioned energy-related parameters, e.g. rotational speed, thickness of individual rims, height of the flywheel structure, orientations of fiber reinforcements, and stacking sequence of rims of different materials. Since most design parameters are interactive, which makes their individual consideration generally impossible, implementation of a numerical optimization routine is critical for flywheel rotor optimization.

4.3.1.   Initial Parameters for Hybrid Composite Rotor Design Optimization

For the optimization procedure the initial rotor geometry was adapted from the model described in Chapter 3, Section 3.3.6.1, i.e. the rotor's inner radius and height were both

kept at 120 mm. The thickness of the inner glass/epoxy rim, t_1, and the outer carbon/epoxy rim, t_2, was changed to 40 mm each. Note that due to the greater computational effort required for optimization models, a smaller 5^0-section was modeled, which deviates from previous chapter where a 45^0-section was used (see Fig.4.2). Boundary conditions remained unchanged compared to the previous model. An initial rotational speed of 12,000 RPM was specified.

4.3.2.   Design Variables (*DV*)

Design variables are independent variables that directly affect the design objective. The thickness of the inner glass/epoxy rim, t_1, and the rotational speed of the flywheel rotor, *RPM*, were specified as design variables for this optimization model. To ensure meshing with elements of adequate aspect ratio, a minimum thickness for the inner rim was specified, i.e. $t_1 = 10$ mm.

4.3.3.   State Variables (*SV*)

State variables are dependent variables that change as a result of changing design variables. State variables are required to constrain the design. In the present model maximum radial and hoop stresses within the inner glass/epoxy rim and the outer carbon/epoxy rim were state variables. Constraint parameters were the radial and hoop strength of the glass/epoxy material, $\overline{(\sigma_r)}_1$, $\overline{(\sigma_\theta)}_1$, and the carbon/epoxy material, $\overline{(\sigma_r)}_2$ $\overline{(\sigma_\theta)}_2$, as well as rotor geometry parameters inner radius, a, total rotor thickness, t, and rotor height, l. The state (stress) variables were constrained based on maximum stress failure theory.
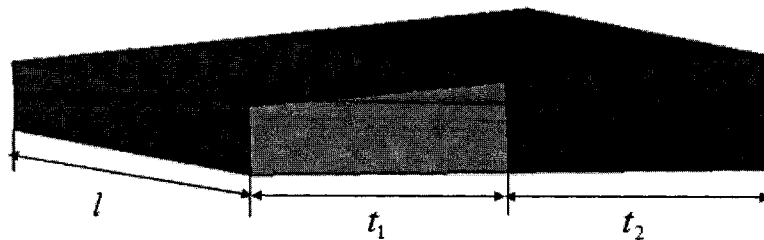
Figure 4.2: 5°-section of hybrid rotor model used for design optimization.

4.3.4.   Objective Function

The aim of the optimization process is to maximize or minimize an objective function, which is a function of one or more design variables. In the context of a numerical modeling routine, it may be more appropriate to speak of an 'objective variable' that is computed based on the various input variables and parameters. The objective function that was to be maximized in the present study was either specific kinetic energy, E_{kin} / M, or kinetic energy per unit cost, $E_{kin} / Cost$.

4.3.5.   Optimization Model

The objective functions that were applied to the current study can be formulated as follows:

$$\text{Case (1): Find } \max\left(\frac{E_{kin}}{M}\right) \text{ where } \frac{E_{kin}}{M} = f(t_1, RPM, M) \qquad (4.1a)$$

$$\text{Case (2): Find } \max\left(\frac{E_{kin}}{Cost}\right) \text{ where } \frac{E_{kin}}{Cost} = f(t_1, RPM, \$) \qquad (4.1b)$$

The objective functions were subject to the following constraints:

$$\underline{t_1} \le t_1 \le \overline{t_1} \qquad (4.2a)$$

$$\sum_j t_j = t \qquad (4.2b)$$

$$l = Const. \qquad (4.2c)$$

$$\underline{RPM} \le RPM \le \overline{RPM} \qquad (4.2d)$$

$$(\underline{\sigma_r})_j(t_j, RPM) \le (\sigma_r)_j(t_j, RPM) \le \overline{(\sigma_r)}_j(t_j, RPM) \quad \forall_j \qquad (4.2e)$$

$$(\underline{\sigma_\theta})_j(t_j, RPM) \le (\sigma_\theta)_j(t_j, RPM) \le \overline{(\sigma_\theta)}_j(t_j, RPM) \quad \forall_j \qquad (4.2f)$$

where j is the material index with $j = 1$ for the glass/epoxy and $j = 2$ for the carbon/epoxy material. Lower and upper bar symbols indicate correspondingly the minimum and maximum values for each parameter. Note that the model was solved separately for each objective function. A schematic outlining the design optimization procedure is shown in Fig.4.3.

Input Data:
- Material Properties
- Rotor geometry data

Initial Design Variables:
t_1, RPM

Finite Element Analysis

Update Design Variables:
t_1, RPM

Feasible Range (Maximum Stress Failure Theory)

Optimum Design:
Maximize E_{kin}/M or $E_{kin}/Cost$
Subject to
$$\sum_j t_j = t \quad SF_j > 1$$

No

Check for Convergence

Yes

Output Data
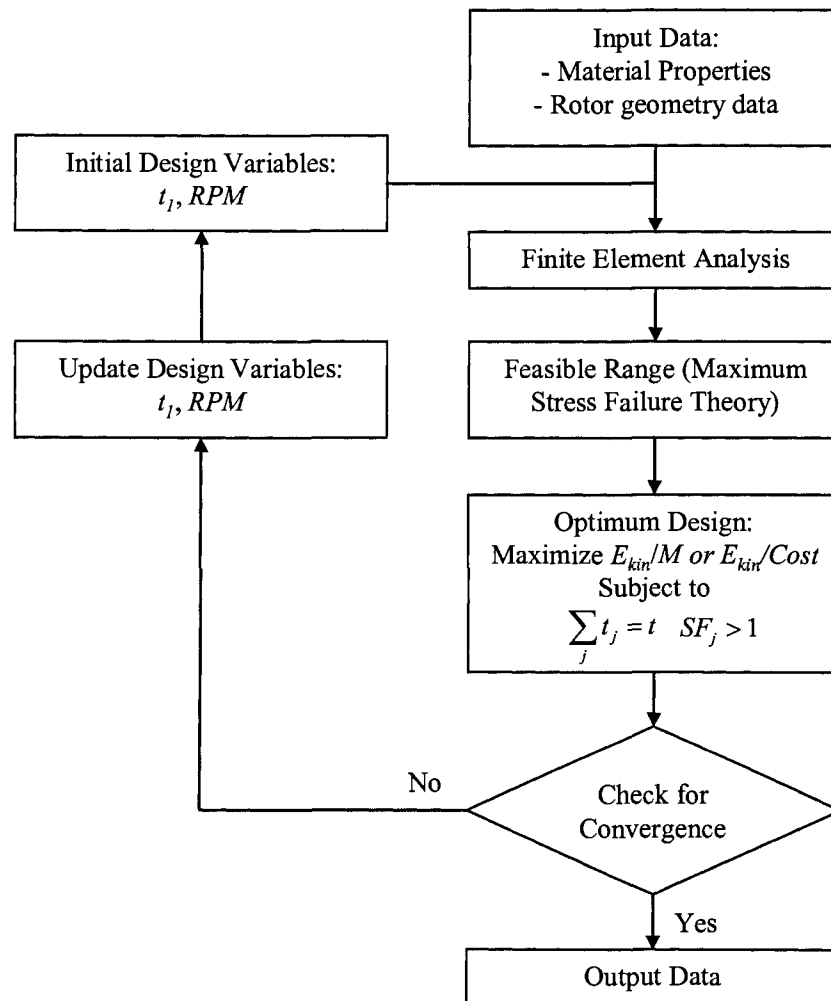
Figure 4.3 Schematic of design optimization procedure for hybrid rotor model.

4.3.6. Sub-Problem Approximation Method

Different methods for design optimization are implemented into the ANSYS software environment. From these methods, Sub-problem Approximation was chosen for the current analysis. Sub-problem Approximation is a general method that can be applied efficiently to a wide range of engineering problems [ANSYS]. Sub-problem Approximation is capable of handling equality and inequality constraints, which were both present in the current optimization model.

The Sub-problem Approximation method is an advanced zero-order method which uses approximations (curve fitting) to all dependent variables (state variables and the objective function). The approximation is a least squares fit (or a user specified method) of the

objective function for several design variables [Gowayed et al., 2002]. Since the Sub-problem Approximation method relies on approximation of the objective function and each state variable, the optimization process usually does not stay in the feasible region [Haftka and Gurdal, 1992]. Thus, an extended interior penalty function, which is a combination of exterior and interior penalty functions, is used to overcome that problem and deal with both equality and inequality constraints. Penalties are added to the objective function to convert the constrained to an unconstrained optimization. In every iteration step the approximation is minimized instead of the objective function until convergence is achieved or termination is indicated [ANSYS]. The approximate sub-problems are updated at each design loop to account for the additional information, and the process continues until convergence criteria are met [Mueller et al., 1994]. This procedure attempts to gain maximum information from each finite element solution while preserving the generality in the choice of design variables, constraints, and objective.

4.3.6.1. Convergence Criteria

In the Sub-problem Approximation method, iterations continue until either convergence is achieved or termination occurs. Convergence is achieved when all constraints on design variables and state variables are satisfied and changes in all design variables and the objective function meet certain criteria between loops. For this optimization problem, convergence was achieved when any of the following conditions was satisfied:

$$\left| (KE/M)^{(j)} - (KE/M)^{(j-1)} \right| \leq 0.5 \ \text{J/kg} \tag{4.3a}$$

$$\left| (KE/M)^{(j)} - (KE/M)^{(b)} \right| \leq 0.5 \ \text{J/kg} \tag{4.3b}$$

$$\left| t_1^{(j)} - t_1^{(j-1)} \right| \leq 0.1 \ \text{mm} \tag{4.3c}$$

$$\left| t_1^{(j)} - t_1^{(b)} \right| \leq 0.1 \ \text{mm} \tag{4.3d}$$

$$\left| RPM^{(j)} - RPM^{(j-1)} \right| \leq 100 \ \text{RPM} \tag{4.3e}$$

$$\left| RPM^{(j)} - RPM^{(b)} \right| \leq 100 \ \text{RPM} \tag{4.3f}$$

In Eqs.(4.3a-f) superscripts (j), $(j-1)$ and (b) indicate the current and previous iteration values and the best value respectively. For example, $(KE/M)^{(j)}$ and $(KE/M)^{(j-1)}$ are

correspondingly the current and previous iteration objective function values, and $(KE/M)^{(b)}$ is the best design objective function value. In addition to one of the preceding conditions being satisfied, the present design set, $t_1^{(j)}$, $(RPM)^{(j)}$, or the previous design set, $t_1^{(j-1)}$, $(RPM)^{(j-1)}$, or the best design set, $t_1^{(b)}$, $(RPM)^{(b)}$, had to be within the feasible range. Tolerances for the inner rim thickness and rotational speed were 10^{-4} m and 100 RPM respectively.

4.3.7.   Maximum Stress Failure Theory

Maximum stress failure theory states that a lamina will fail if any of the normal or shear stresses $\sigma_1, \sigma_2, \tau_{12}$ are equal to or exceed corresponding ultimate lamina strengths, where subscripts "1" and "2" indicate the in-fiber and transverse-to-fiber direction. This criterion does not consider any coupling effects between the stress components. In terms of mathematical expressions, lamina failure will occur when any of the following inequalities are violated [Kaw, 2006]:

$$-(\sigma_1^C)_{ult} < \sigma_1 < (\sigma_1^T)_{ult} \tag{4.4a}$$

$$-(\sigma_2^C)_{ult} < \sigma_2 < (\sigma_2^T)_{ult} \tag{4.4b}$$

$$-(\tau_{12})_{ult} < \tau_{12} < (\tau_{12})_{ult} \tag{4.4c}$$

where $(\sigma_1^T)_{ult}$ and $(\sigma_1^C)_{ult}$ are the ultimate longitudinal tensile and compressive strength; $(\sigma_2^T)_{ult}$ and $(\sigma_2^C)_{ult}$ are the ultimate transverse tensile and compressive strength; and $(\tau_{12})_{ult}$ is the ultimate in plane shear strength.

The maximum stress failure theory was employed in this optimization model to determine the feasible range, i.e. stresses in the fiber longitudinal and transverse directions developed during rotor rotation were compared with strength data of the corresponding material. Note that more advanced failure theories such as the Tsai-Wu failure criterion, could also be applied to this model. However, it is inherently difficult to obtain sets of failure parameters for such criteria. In contrast, implementation of the maximum stress failure criterion is relatively simply, and it is considered to yield results acceptable accuracy for present analyses.

4.4.   Results and Discussions for Optimal Specific Kinetic Energy

The optimization model for the hybrid composite flywheel rotor with one glass/epoxy rim and one carbon/epoxy rim yielded a specific kinetic energy of 0.312 MJ/kg. As shown in Fig.4.4, convergence was achieved after 15 iterations. Figure 4.5 shows that even though the initial thickness of both rims was 40 mm at the start of the optimization routine, an optimal thickness of 10 mm for the glass/epoxy rim and 70 mm for the carbon/epoxy rim was computed. Since the objective was to maximize kinetic energy per unit mass, and glass/epoxy has greater mass than carbon/epoxy, the thickness of the glass/epoxy rim was reduced to the minimum allowable value of 10 mm (accordingly, the thickness of the carbon/epoxy rim was 70 mm). The rotational speed reached a maximum of 46,000 RPM, see Fig. 4.6; for higher loadings the solution would no longer be in the feasible range.
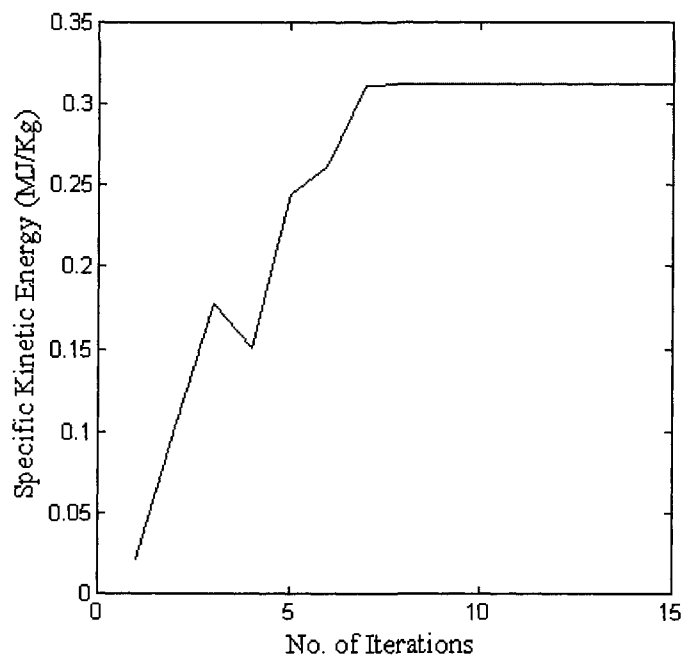
Figure 4.4: Specific kinetic energy with respect to iteration number for hybrid rotor model with glass/epoxy and carbon/epoxy composite rims.
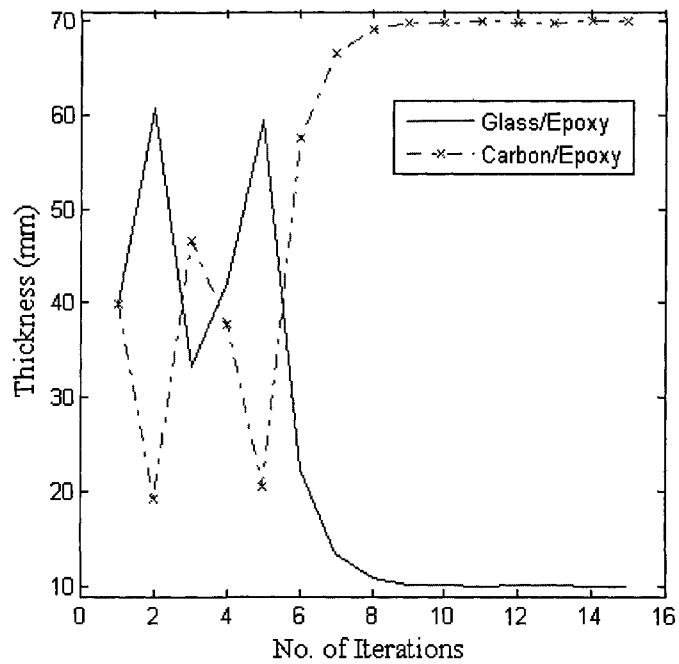
Figure 4.5: Thickness of inner glass/epoxy rim and outer carbon/epoxy rim with respect to iteration number from specific kinetic energy optimization.
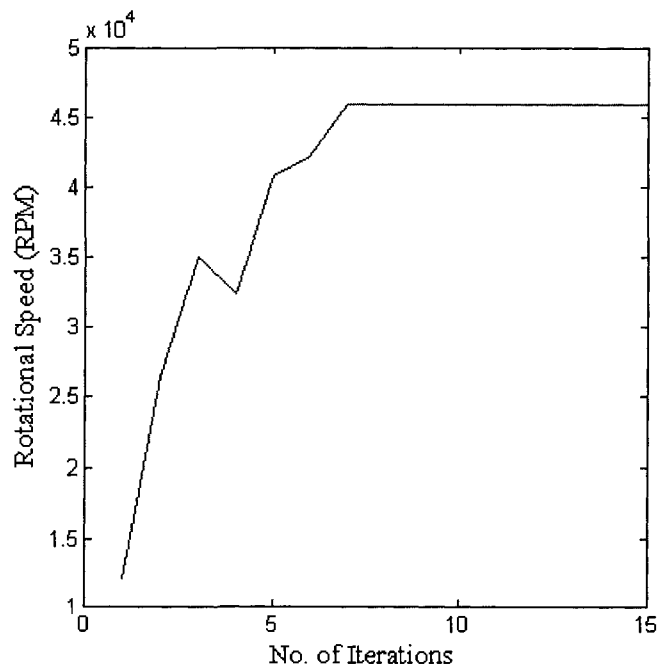
Figure 4.6: Rotational speed with respect to iteration number for hybrid rotor model with glass/epoxy and carbon/epoxy rims from specific kinetic energy optimization.

4.5.   Model Validation for Specific Kinetic Energy Optimization

Results obtained from the numerical optimization model were validated using an analytical approach (see Chapter 3 for details). For the same basic rotor geometry the change in specific kinetic energy with respect to rotational speed and the thickness of the outer material carbon/epoxy rim are shown in Fig.4.7. From this figure it can be observed that specific kinetic energy increases with rotational speed as well as with increasing thickness of the carbon/epoxy rim. Note that data presented in Fig.4.7 is in good agreement with those shown in Figs.4.4 to 4.6, e.g. a maximum specific kinetic energy of 0.312 MJ/kg was obtained from both the numerical optimization and the analytical model.
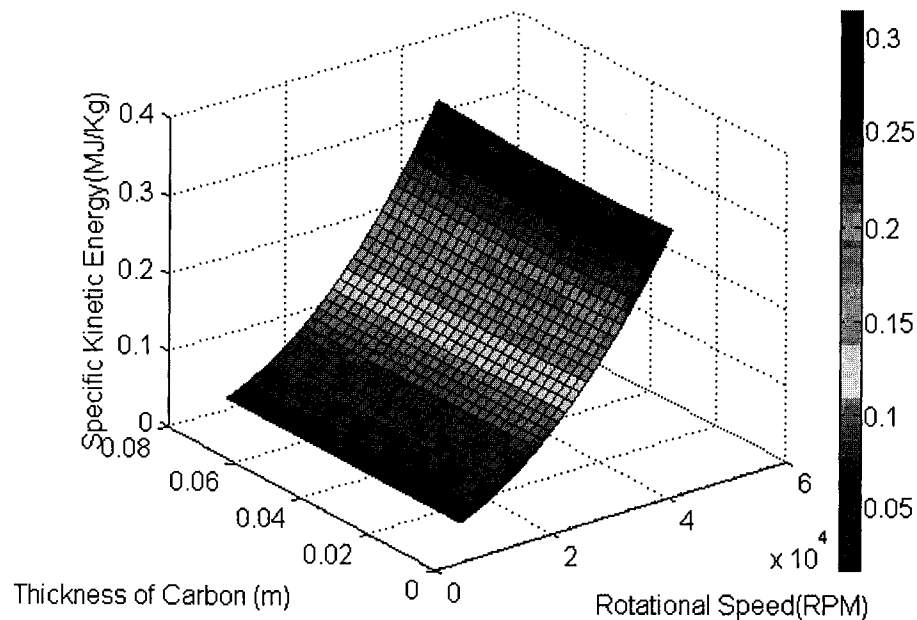
Figure 4.7: Effect of rotational speed and carbon/epoxy composite rim thickness on specific kinetic energy obtained from analytical analysis.

4.6. Evolution of Rotor Stresses for Specific Kinetic Energy Optimization.

The analytical model does not provide sufficient information on rotor stress distribution. From the numerical model, on the other hand, the entire stress field can be studied, and the stress distribution at the optimal state, including locations of stresses nearing ultimate values, can be examined. This information can be used to further validate the employed optimization scheme. Shown in Table 4.1 are rotational speed, rim thicknesses and specific kinetic energy that were computed for the first, 6th, and final (15th) iteration during the specific kinetic energy optimization. In addition, radial and hoop stress profiles for the three iterations are shown in Figs.4.8 and 4.9. These stress data were taken along the through-thickness direction in the rotor mid-plane. For the initial iteration step (i.e. initial design variables were a thickness of 40 mm for both rims and an rotational speed of 12,000 RPM), rotor specific kinetic energy was 0.0209 MJ/kg with maximum radial stresses of 0.14 MPa and 0.324 MPa within the glass/epoxy and carbon/epoxy rim respectivley. At the 6th iteration when rotational speed was increased to 42,227 RPM, radial stresses were fully compressive within the glass/epoxy rim with a maximum of -0.82 MPa; the maximum radial stress in the carbon/epoxy rim was 26.45MPa. Corresponding hoop stresses were 456 MPa and 1259 MPa. At this point the thickness of the carbon/epoxy rim had increased to 57.7 mm (consequently the thickness of glass/epoxy rim had decreased to 22.3 mm). Specific kinetic energy was now 0.261 MJ/kg. Convergence was attained at the 15th iteration. As mentioned previously, the final specific kinetic energy was 0.312 MJ/kg for a rotational speed of 46,000 RPM, and thicknesses of the carbon/epoxy and glass/epoxy rims were 70 mm and 10 mm respectively. Maximum radial stresses within the glass/epoxy and carbon/epoxy rims were correspondingly -3.65 MPa and 56.04MPa. As required, the latter value remained below the ultimate radial tensile strength of carbon/epoxy, and hence the strength factor (*SF*) for this material remained greater than 1. Maximum hoop stresses for the glass/epoxy (413 MPa) and carbon/epoxy rim (1312 MPa) also remained below material allowables. It is interesting to note significant differences between results for the hybrid rotor and the single-material carbon/epoxy rotor that was discussed in Chapter 3,

Section 3.3.5.3. In the single-material case, radial stresses were tensile for the entire rotor whereas the addition on the glass/epoxy rim produced a zone of compressive radial stress. In conclusion, this analysis showed that the numerical optimization routine worked properly, satisfied all of the constraints and produced sensible results.

Table 4.1: Values for design variables and objective function recorded at three different iterations during the optimization routine for specific kinetic energy.

Iteration No.	Rotational speed (RPM)	Rim thickness (mm)		Specific kinetic energy (MJ/kg)
		Glass/epoxy	Carbon/epoxy	
1	12,000	40.0	40.0	0.021
6	42,227	22.3	57.7	0.261
15	46,000	10.0	70.0	0.312
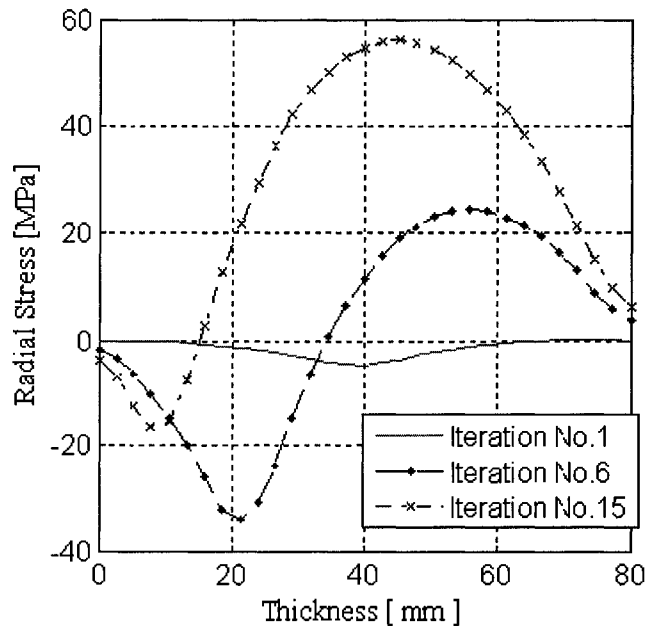
Figure 4.8: Radial stress with respect to (radial) thickness position for the hybrid rotor model with glass/epoxy and carbon/epoxy rims from specific kinetic energy optimization.
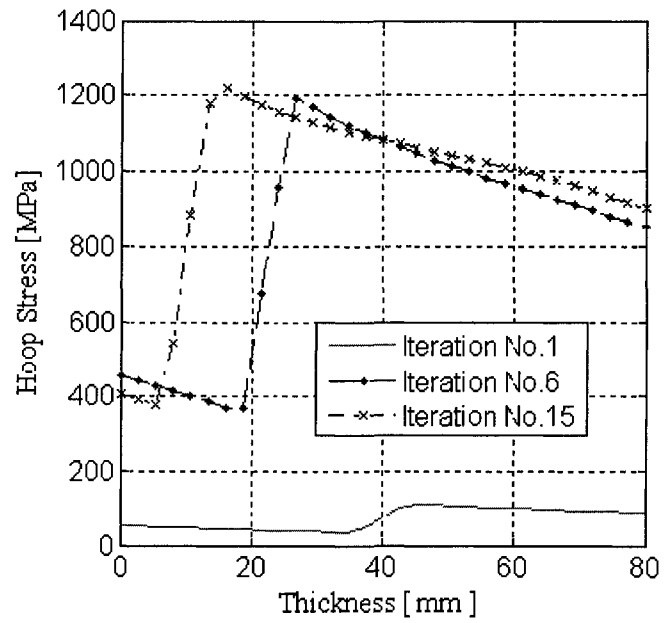
Figure 4.9: Hoop stress with respect to (radial) thickness position for the hybrid rotor model with glass/epoxy and carbon/epoxy rims from specific kinetic energy optimization.

CHAPTER 5

DESIGN OPTIMIZATION CASE STUDIES FOR HYBRID COMPOSITE FLYWHEEL ROTORS

In preceding chapters the development of 3-dimensional finite element models for hybrid composite flywheel rotors, their validation, and the implementation of a numerical design optimization routine was described. Good agreement between results from the numerical modeling scheme and analytical studies indicates that the developed modeling approach can be utilized for studying the behavior of various hybrid composite flywheel rotor configurations. One goal of this thesis project was to assess differences between rotor designs that were optimized either for specific kinetic energy or for kinetic energy per unit cost. Accordingly, effects of material density and cost on the performance of hybrid composite flywheel rotors were examined in the present chapter. This investigation was conducted in the form of case studies. In the first case study, the two-material hybrid composite rotor previously described in Chapter 4 was now optimized for maximum kinetic energy per unit cost. In the second case study, design optimization was performed for a hybrid composite rotor subject to press fit or residual thermal stress effects. In the third case study, design optimization for a flywheel rotor with three rims of different materials was performed. In all three case studies, differences between optimizing a rotor either for maximum specific kinetic energy or kinetic energy per unit cost were investigated.

5.1.   Case Study #1

In this case study the same optimization model as described in Chapter 4, i.e. a model for a two-material hybrid rotor with E-glass/epoxy and carbon/epoxy composite rims, was used to maximize kinetic energy per unit cost. Cost is directly related to the amount of fiber-reinforced polymer materials used to construct the hybrid composite flywheel rotor. For the glass/epoxy and carbon/epoxy materials specific cost 10$/kg and 90$/kg were assumed respectively. Results in terms of rim thicknesses and kinetic energy storage were compared to results from Chapter 4 obtained for specific kinetic energy optimization. The

basic rotor geometry (height and total thickness) were adopted from the preceding optimization, and fiber orientations were again in the circumferential direction. The same design variables were used as in Chapter 4 for optimizing specific kinetic energy, i.e. the thickness of the inner rim, t_I, and the rotational speed of the flywheel rotor, *RPM*. Boundary conditions were applied as described in Chapter 3. A 1/72 section of the rotor was modeled. Convergence criteria as given in Chapter 4, Section 4.3.6.1 were applied. The exception were criteria given in Eqs.(4.3a-b) which needed to be adapted for optimizing kinetic energy per unit cost, i.e.

$$\left|(KE/\$)^{(j)} - (KE/\$)^{(j-1)}\right| \leq 0.5 \, \text{J}/\$ \tag{5.1a}$$

$$\left|(KE/\$)^{(j)} - (KE/\$)^{(b)}\right| \leq 0.5 \, \text{J}/\$ \tag{5.1b}$$

where $(KE/\$)^{(j)}$ and $(KE/\$)^{(j-1)}$ are correspondingly the current and previous iteration objective function values, and $(KE/M)^{(b)}$ is the best design objective function value.

5.1.1.   Results and Discussions for Optimization of Kinetic Energy per Unit Cost

The maximum kinetic energy per unit cost was 9.90 kJ/$ for the two-material hybrid composite flywheel rotor. Convergence was obtained after 11 iterations, see Fig.5.1. In this figure the variation of the objective function with iteration number is presented. Figure 5.2 shows that rim thicknesses changed from their initial value of 40 mm to 69.8 mm for the glass/epoxy rim and 10.2 mm for the carbon/epoxy rim. The majority of the flywheel rotor is hence composed of less expensive glass/epoxy material which is a plausible outcome of the optimization for kinetic energy per unit cost. The thickness of the rim of costlier carbon/epoxy material nearly reached the limit of 10 mm (this limit was set to ensure acceptable element aspect ratios during meshing). The maximum rotational speed was 36,943 RPM; beyond this loading, rotor stresses were no longer in the feasible range. A graph showing rotational speed over iteration number is shown in Fig.5.3.
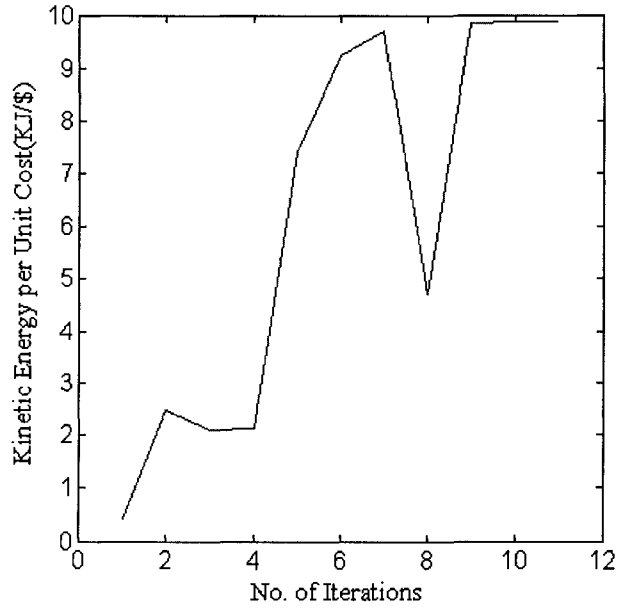
Figure 5.1: Kinetic energy per unit cost with respect to iteration number for hybrid rotor

model with glass/epoxy and carbon/epoxy composite rims.
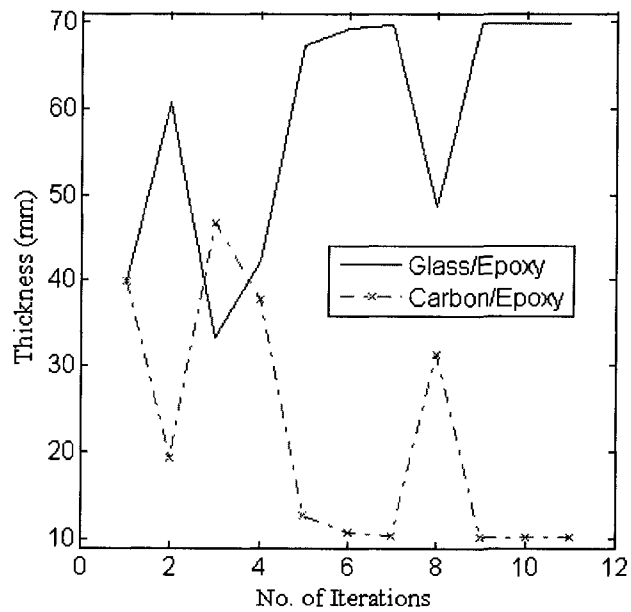
Figure 5.2: Thickness of inner glass/epoxy rim and outer carbon/epoxy rim with respect

to iteration number from optimization of kinetic energy per unit cost.
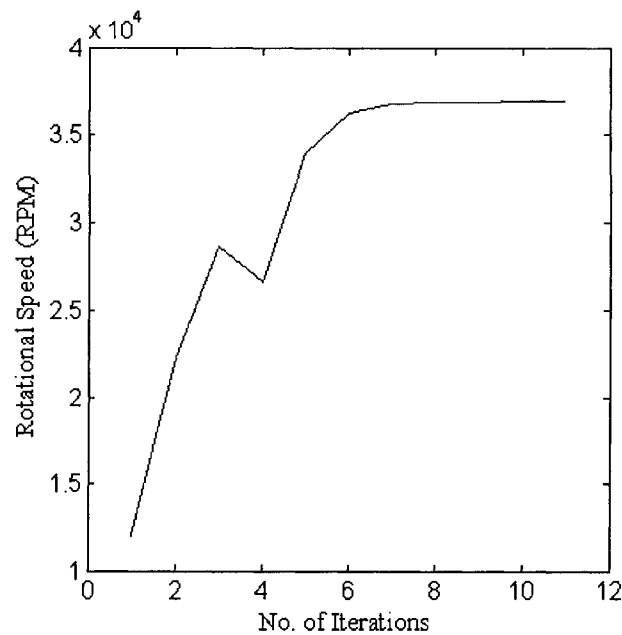
Figure 5.3: Rotational speed with respect to iteration number for hybrid rotor model with glass/epoxy and carbon/epoxy rims from optimization of kinetic energy per unit cost.

5.1.2. Model Validation for Optimization of Kinetic Energy per Unit Cost

The change of kinetic energy per unit cost with rotational speed and thickness of the inner glass/epoxy composite rim are shown in Fig.5.4. This figure shows that kinetic energy per unit cost increased with rotational speed and the thickness of the rim made from glass/epoxy material, which is denser and has a lower modulus than the carbon/epoxy composite. Data from the numerical model were again validated using results from analytical analysis using a model with identical geometry and loading conditions. Figure 5.4 shows analytical results, which compare favorably with numerical data shown in Figs.5.1 to 5.3. For both the numerical and analytical case a maximum kinetic energy per unit cost of 9.9 kJ/kg was found. The corresponding thicknesses of the glass/epoxy and carbon/epoxy rim were 69.8 mm and 10.2 mm respectively.
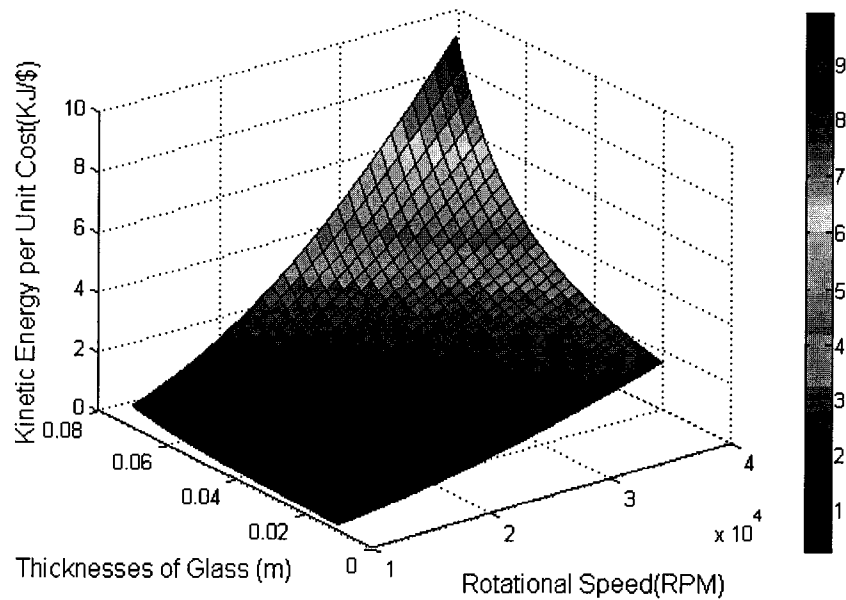
Figure 5.4: Effect of rotational speed and glass/epoxy composite rim thickness on specific kinetic energy obtained from analytical analysis.

5.1.3. Evolution of Rotor Stresses for Optimization of Kinetic Energy per Unit Cost

It is not possible to assess the stress distribution and peak stresses within the flywheel rotor from the analytical approach employed in the preceding section. This assessment was done using radial and circumferential stress data from the numerical model, which allowed for further validation of the developed optimization routine.

Radial and hoop stress data for the first, 8th and final (11) iteration are shown in Fig.5.5 and Fig.5.6 respectively. For the first iteration the initial thickness of the glass/epoxy and carbon/epoxy rims was 40 mm; the rotational speed was 12,000 RPM. A maximum radial stress 0.14 MPa for the glass/epoxy rim and 0.32 MPa for the carbon/epoxy rim was computed. The kinetic energy per unit cost was 0.41 kJ/$. In the 8th iteration, rotational speed increased to 36,926 RPM, causing a maximum radial stress in the glass/epoxy rim of 6.0 MPa and in the carbon/epoxy rim of 0.004 MPa. Corresponding values for hoop stress were 804 MPa and 1658 MPa. At this point the thickness of the carbon/epoxy had decreased to 31.3 mm, and the thickness of glass/epoxy rim had increased to 48.7 mm.

Kinetic energy per unit cost was 7.42 kJ/$. As mentioned previously, the solution converged in the 11[th] iteration, when a maximum kinetic energy per unit cost of 9.9 kJ/$ was reached for a rotational speed of 36,943 RPM. The thickness of the glass/epoxy rim had further increased to 69.8 mm, leaving a thickness of the carbon/epoxy rim of only 10.2 mm. The optimization of kinetic energy per unit cost resulted in a considerable reduction of the amount of costlier carbon/epoxy material. Maximum radial stresses were 37.2 MPa in the glass/epoxy and -3.76 MPa in the carbon/epoxy material. In other words, the highest tensile radial stress was found in the thick rim of glass/epoxy material that has greater density and lower modulus than the carbon/epoxy material of the thinner outer rim. The latter exhibited compressive radial stresses. Note that the maximum radial stress in the glass/epoxy rim of 37.2 MPa remained below the material's ultimate transverse strength of 39 MPa, i.e. the solution was in the feasible region. Also the corresponding maximum hoop stresses in the glass/epoxy and carbon/epoxy rims of 814MPa and 1679MPa were below corresponding circumferential strengths of the materials. These values confirm that the numerical optimization routine for maximizing kinetic energy per unit cost satisfied imposed constraints and produced sensible results. From above results it could again be inferred that radial loads are more critical than stresses in the hoop direction, confirming the notion that considerable attention must be given to radial stress reduction when designing hybrid composite rotors.

Table 5.1: Values for design variables and objective function recorded at three different iterations during the optimization routine for kinetic energy per unit cost.

Iteration No.	Rotational speed (RPM)	Rim thickness (mm)		Kinetic energy per unit cost (kJ/$)
		Glass/epoxy	Carbon/epoxy	
1	12,000	40.0	40.0	0.41
8	36,926	48.7	31.2	7.42
11	36,943	69.8	10.2	9.90
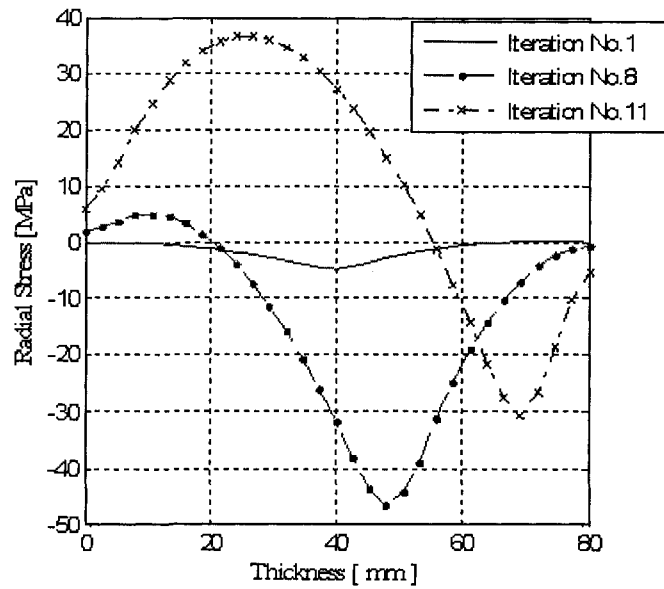
Figure 5.5: Radial stress with respect to (radial) thickness position for rotor model with glass/epoxy and carbon/epoxy rims from optimization of kinetic energy per unit cost.
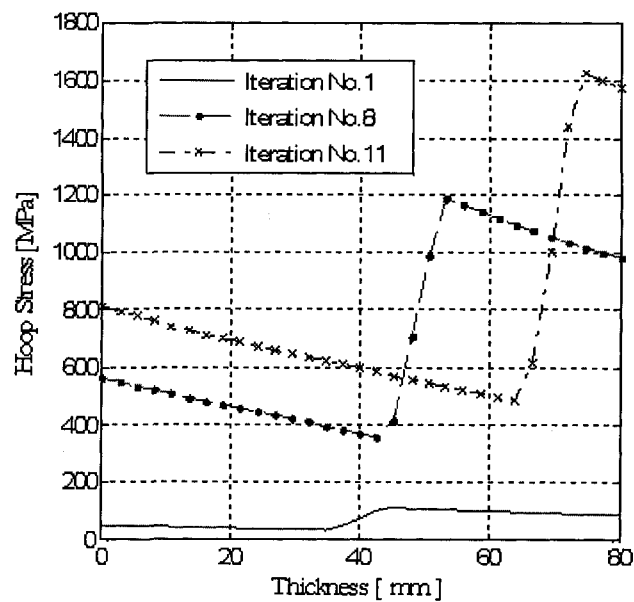
Figure 5.6: Hoop stress with respect to (radial) thickness position for rotor model with glass/epoxy and carbon/epoxy rims from optimization of kinetic energy per unit cost.

5.1.4.   Comparison with Single-Material Glass/Epoxy Composite Rotor

To examine the effect of the outer carbon/epoxy rim, the optimization model for kinetic energy per unit cost was solved only for a single-material glass/epoxy composite rotor. Thickness of the glass/epoxy rim was kept constant at 80 mm during the optimization while all other geometric parameters and boundary conditions remained the same as for the two-material hybrid rotor with glass/epoxy and carbon/epoxy rims. Hence, the only design variable in this case was rotational speed.

Results obtained from this optimization were compared with the two-material hybrid composite rotor. The evolution of the objective function with iteration number is presented in Fig. 5.7. For the single-material case convergence was achieved after 7 iterations, and the maximum kinetic energy per unit cost is shown to be 10.44 kJ/$ (compared to 9.9 kJ/$ for the two-material case). Maximum rotational speed was 26,456 RPM, which is considerably less than the value for the hybrid composite rotor of 36,943 RPM. Correspondingly, the maximum in kinetic energy for the glass/epoxy rotor was only 1.98 MJ; with 3.71 MJ the maximum kinetic energy was significantly higher for the carbon/epoxy and glass/epoxy composite rotor (see Fig.5.8).

Data for total kinetic energy, kinetic energy per unit cost and specific kinetic energy from optimization of kinetic energy per unit cost for both rotor configurations are summarized in Table 5.2. This table shows that even though cost savings of 5.2% were achieved for the single-material rotor, the hybrid rotor offers a 46.6% greater energy storage capacity. The hybrid rotor is also superior in terms of specific kinetic energy which is 50% greater than for the single-material rotor. Clearly, compressive radial stresses that developed in the hybrid composite rotor during rotation operation allowed for much higher rotational speed. Hence, considering other costs associated with the flywheel device such as for bearings, vacuum housing and power electronics, the cost savings for a single-material glass/epoxy rotor are insignificant.
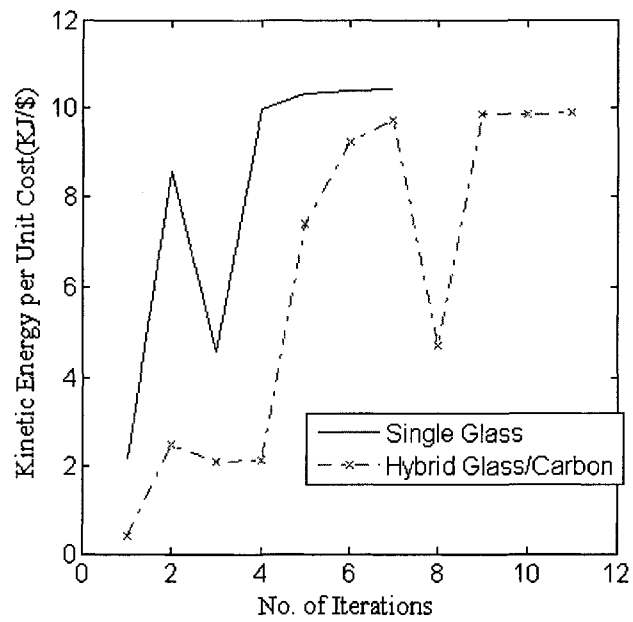
Figure 5.7: Objective function values of kinetic energy per unit cost over iteration number for single-material glass/epoxy and two-material hybrid composite rotor with carbon/epoxy and glass/epoxy rims.
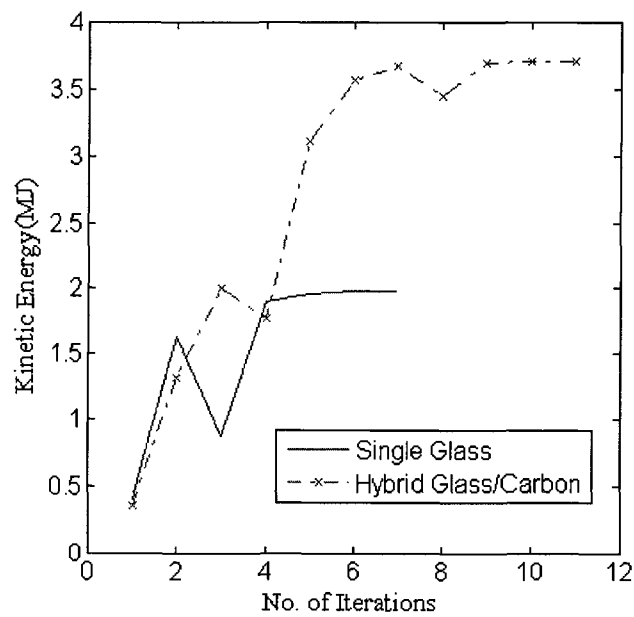
Figure 5.8: Total kinetic energy from optimization of optimal kinetic energy per unit cost over iteration number for single-material glass/epoxy and two-material hybrid composite rotor with carbon/epoxy and glass/epoxy rims.

Table 5.2: Maximum total kinetic energy, kinetic energy per unit cost and specific kinetic energy from optimization of kinetic energy per unit cost for single-material glass/epoxy and two-material hybrid composite rotor with carbon/epoxy and glass/epoxy rims.

	Single-material glass/epoxy rotor	Two-material glass/epoxy and carbon/epoxy rotor
Absolute Kinetic Energy	1.98 MJ	3.71 MJ
Kinetic energy per unit cost	10.4 kJ/$	9.9 kJ/$
Specific Kinetic Energy	0.10 MJ/kg	0.20 MJ/kg

5.1.5.   Comparison of Results from Optimization of Specific Kinetic Energy and Kinetic Energy per Unit Cost

For the presently considered rotor geometry, optimization for specific kinetic energy yielded a maximum rotational speed of 46,000 RPM resulting in a kinetic energy storage of 4.93 MJ; equivalent specific energy terms were 0.31 MJ/kg and 3.88 kJ/$. Final thicknesses of the glass/epoxy and carbon/epoxy composite rims were 10 mm and 70 mm respectively. In contrast, optimization of kinetic energy per unit cost yielding a maximum rotational speed of 36,943 RPM corresponding to a kinetic energy of 3.71 MJ and specific kinetic energy terms of 0.2 MJ/kg and 9.9 kJ/$. Thicknesses for the glass/epoxy and carbon/epoxy rims were 69.8 mm and 10.2 mm respectively. Evidently, due to the effect of either cost or material density, rim thicknesses for the individual materials were considerably different for the two objective functions. It is interesting to note that optimization for kinetic energy per unit cost produced a rotor geometry that provides 70% cost savings while having only 25% less energy storage capacity than the rotor geometry optimized for specific kinetic energy. Clearly, an optimization routine employing cost data is beneficial for designing utility-grade flywheel systems, since in these devices cost is a much more decisive design factor than mass.

5.2.   Case Study #2

The principal task in designing flywheel composite rotors is to maximize either specific kinetic energy or kinetic energy per unit cost. As shown previously, for both objectives it

is of great importance to specifically minimize radial tensile stresses (caused by expansion mismatch during curing in the manufacturing process and by centrifugal forces during flywheel operation). Interference-fit (press-fit) assembly of composite rims is one of the many techniques to achieve this goal (see Chapter 3, Section 3.4). An interference fit serves to mitigating high radial tensile stresses in the rotor by superimposing a compressive radial stress, allowing an increase in rotational speed and energy storage capacity. In the present case study, design optimization was performed to maximize specific kinetic energy or kinetic energy per unit cost for a two-material hybrid rotor with interference-fit rims. The effect of interference-fit on rotor performance was investigated using the modeling approach described in Chapter 3, Section 3.4, i.e. thermally induced residual stresses were simulated by imposing a fictitious temperature load unto the model. The two-material hybrid rotor consisted again of an inner glass/epoxy rim and an outer carbon/epoxy rim. Design variables were the thickness of the inner rim and rotational speed. The optimization routine along with the rotor dimensions described in Chapter 4 were employed again in the present analysis (specifically, initial thickness of 40 mm was assumed for both rims). Model loads were applied in terms of an initial rotational speed of 12,000 RPM and thermally induced stresses corresponding to a temperature rise of 80 K.

5.2.1. Results and Discussions for an Interference-Fit Hybrid Composite Rotor from Optimization of Specific Kinetic Energy

As shown in Figs.5.9 and 5.10, optimization of specific kinetic energy for the interference-fit hybrid rotor produced a maximum specific kinetic energy of 0.35 MJ/kg and thicknesses of the glass/epoxy and carbon/epoxy rims of 10 mm and 70 mm respectively. The latter are identical to the thickness values obtained from the model without interference-fit. The maximum rotational speed of 49,000 RPM, however, was considerably higher than for the model without interference-fit (i.e. 46,000 RPM, see Chapter 4). Clearly, reducing overall radial stress by superimposing compressive stresses from thermal loading allowed for greater rotational speed. As a consequence, specific

kinetic energy was increased for the interference-fit model as well, which was 0.35 MJ/kg compared to 0.31 MJ/kg for the model without interference-fit.

Figure 5.9: Objective function values of specific kinetic energy over iteration number for hybrid composite rotor with thermally induced interference-fit.

Figure 5.10: Thickness of inner glass/epoxy rim and outer carbon/epoxy rim over iteration number from optimization of specific kinetic energy for a hybrid composite rotor with thermally induced interference-fit.

5.2.2. Results and Discussions for an Interference-Fit Hybrid Composite Rotor from Optimization of Kinetic Energy per Unit Cost

Optimizing the two-material hybrid composite rotor with interference-fit for kinetic energy per unit cost yielded an objective function maximum of 11.28 kJ/$, and thicknesses for the glass/epoxy and carbon/epoxy rim of 69.9 mm and 10.1 mm respectively. The evolution of preceding values with respect to iteration is shown in Figs.5.11 and 5.12. For this model the same cost parameters were used as given in Section 5.1 of this chapter. Rim thicknesses produced by the present analysis were identical to those found from the model without interference-fit (see Section 5.1.1). Maximum rotational speed, however, was considerably higher, i.e. for the model with and without interference-fit, 39,438 RPM and 36,943 RPM were computed respectively. Evidently, thermally induced residual stresses allowed for higher loading resulting in a higher maximum kinetic energy per unit cost of 11.3 kJ/$ (compared to 9.9 kJ/$ for the model without thermal stress effect).

5.2.3. Comparison of the Optimization Results for Specific Kinetic Energy and Kinetic Energy per Unit Cost for a Press-Fit Hybrid Composite Rotor

For specific kinetic energy, the maximum rotational speed of 49,000 rpm and absolute kinetic energy, E_{kin}, of 5.60 MJ was found. This corresponds to specific energy terms of 0.354MJ/Kg and 4.40KJ/$. The final thickness of glass/epoxy and carbon/epoxy composite rings was 10 mm and 70 mm. In contrast, optimizing kinetic energy per unit cost yielded a rotational speed of 39438 RPM and absolute kinetic energy, E_{kin}, of 4.23MJ, corresponding to 0.229MJ/Kg and 11.28 KJ/$. Respective ring thinness for glass/epoxy and carbon/epoxy was 69.90 mm and 10.10 mm. Due to the effect of cost and density, the thickness of individual materials for both optimization cases were different. It can be inferred that in case of kinetic energy per unit cost for this press fitted hybrid composite flywheel the rotor geometry would yield 71% cost savings while only providing 24% less total energy stored than the rotor geometry optimized for maximum kinetic energy per unit mass, which was also same for the non press fitted (only inertia loading) two material hybrid composite flywheel rotor.
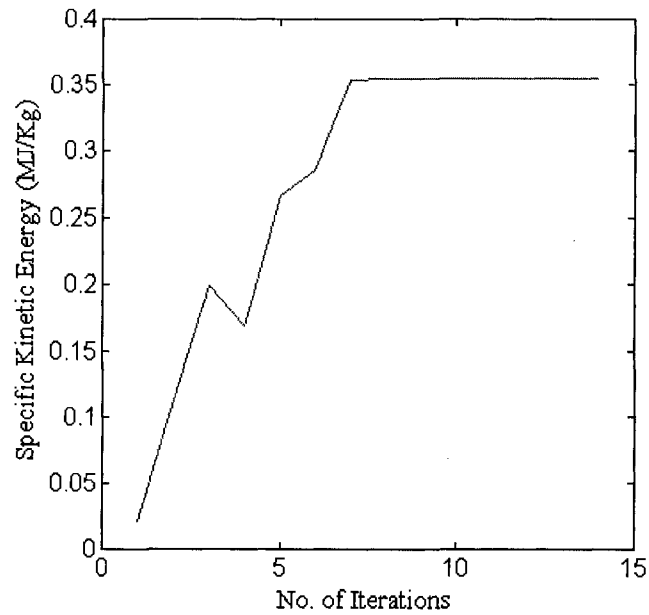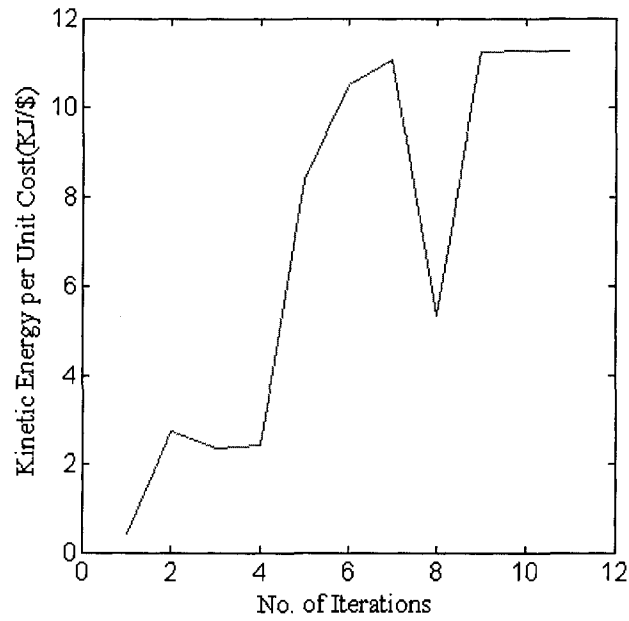
Figure 5.11: Objective function values of kinetic energy per unit cost over iteration number for hybrid composite rotor with thermally induced interference-fit.

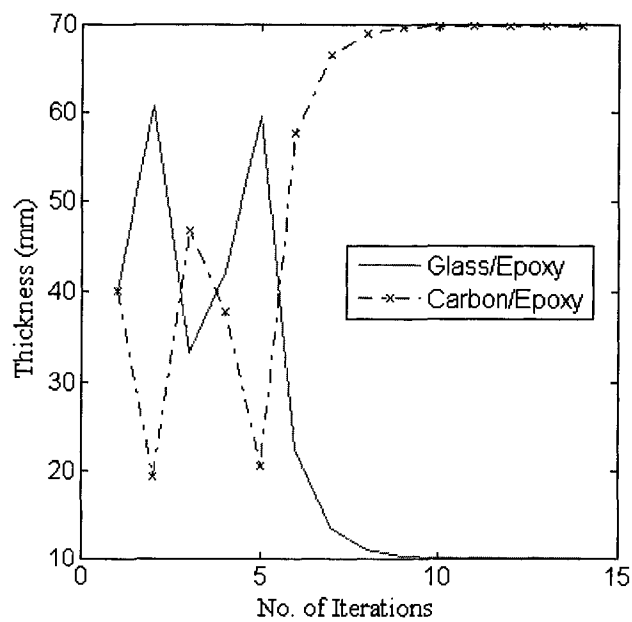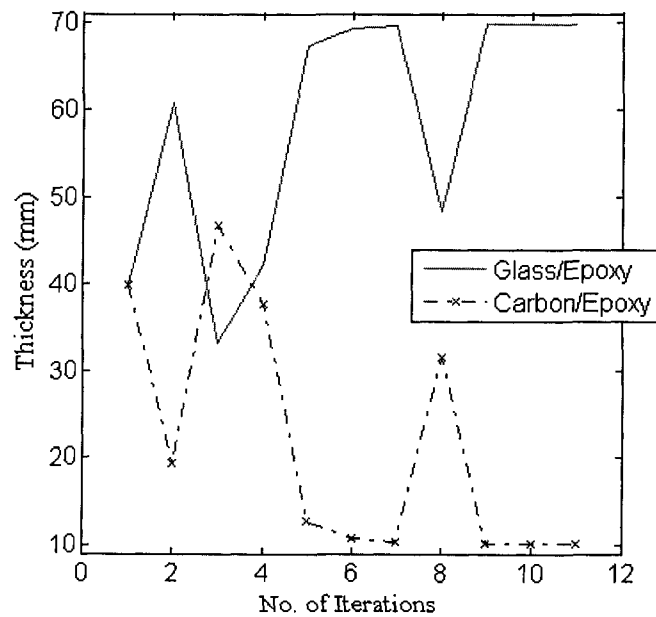
Figure 5.12: Thickness of inner glass/epoxy rim and outer carbon/epoxy rim over iteration number from optimization of kinetic energy per unit cost for a hybrid composite rotor with thermally induced interference-fit.

5.3.   Case Study #3

In this final case study, optimization was performed combining three different composite material rims. Corresponding results were compared to data from the two-material hybrid composite rotor that was the subject of the preceding two case studies.

The geometry for the three-material rotor was adopted from the two-material rotor (i.e. the rotor's inner radius, total thickness and height were 12 cm, 8 cm and 12 cm respectively). As stated previously, number and sequence of rims of different materials are critical design considerations for achieving maximum performance. For a hybrid rotor, an optimal configuration provides a rim sequence so that material density and compliance decrease with increasing radius. That way, aforementioned rotor growth mismatch is counteracted by the radial expansion of inner rims that press against higher-modulus (i.e. less expanding) rims on the outside of the rotor [Ha and Kim, 1999a].

In this optimization model E-glass/epoxy, AS4-carbon/epoxy and IM6-carbon/epoxy were the materials the inner, middle and outer rim respectively. Corresponding initial thicknesses of the three rims (t_1, t_2, t_3) were respectively for design Case A: 35 mm, 35 mm and 10 mm; and for design Case B: 25 mm, 25 mm and 30 mm. The orientation of the fiber reinforcement phase was again in circumferential direction. Material properties for unidirectional IM6-carbon/epoxy are given in Table 5.3. Specific cost of 10$/kg, 90$/kg and 100$/kg were assumed for the E-glass/epoxy, AS4-carbon/epoxy and IM6-carbon/epoxy composite materials.

As in the previous case studies, only a 1/72-section of the full flywheel rotor was modeled. Optimization was performed for both design cases applying the Sub-problem Approximation method described in Chapter 4. Design variables were the same as those used for the two-material hybrid rotor, i.e. thickness of the inner rim and the rotational speed. Also the same constraints were applied. Note that for the three-material rotor,

$$\sum_j t_j = t_1 + t_2 + t_3 = 80 \text{ mm} \qquad (5.2)$$
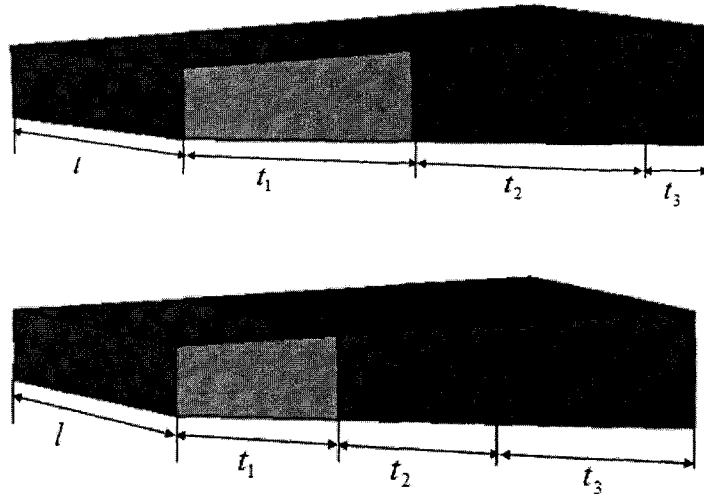
Figure 5.13: Initial configuration of 1/72-section of three-material hybrid rotor for design Case A (top) and Case B (bottom).

5.3.1.   Results and Discussions for the Three-Material Hybrid Composite Rotor

Optimization of specific kinetic energy for the three-material hybrid composite rotor provided maximum specific kinetic energies of 0.37 MJ/kg and 0.57 MJ/ kg for Case A and Case B respectively (see Fig.5.14 and Table 5.5). Figure 5.15 shows corresponding rotational speeds which reached maximum values of 50,000 RPM and 62,500 RPM. Final rim thicknesses provided by the optimization routine are given in Table 5.4. In both cases, the mass-based optimization favored the lighter carbon materials. Hence, the thickness of the E-glass/epoxy rim reached the pre-set lower limit of 10 mm, and the thickness of the AS4-carbon/epoxy rim reached the maximum allowable value of 60 mm for Case A, and 40 mm for Case B. The thickness of the outer rim with the high-modulus carbon composite was greatest for Case B. Consequently, greater rotational speed could be applied before rotor stresses reached material allowables, and energy storage capacity was higher for Case B than for Case A.

Table 5.3: Properties for unidirectional IM6-carbon/epoxy composite [Ha et al., 1999b]

Property	IM6 carbon/epoxy
Density, ρ, g/cm^3	1.60
Longitudinal modulus, E_1, GPa	203
Transverse modulus, E_2, GPa	11.2
Major in-plane Poisson's ratio, υ_{12}	0.32
Out-of-plane Poisson's ratio, υ_{23}	0.54
Out-of-plane Poisson's ratio, υ_{13}	0.32
In-plane shear modulus, G_{12}, GPa	8.4
Out-of-plane shear modulus, G_{23}, GPa	8.4
Out-of-plane shear modulus, G_{13}, GPa	8.4
Longitudinal tensile strength, σ_1^T, MPa	3500
Transverse tensile strength, σ_2^T, MPa	56
Longitudinal compressive strength, σ_1^C, MPa	1540
Transverse compressive strength, σ_2^C, MPa	150

Table 5.4: Rim thicknesses from optimization of the three-material hybrid rotor.

	Rim thickness (mm)					
	Optimization of specific kinetic energy			Optimization of kinetic energy per unit cost		
	E-glass epoxy	AS4-carbon epoxy	IM6-carbon epoxy	E-glass epoxy	AS4-carbon epoxy	IM6-carbon epoxy
Case A	10.1	59.9	10	59.91	10.09	10
Case B	10.1	39.9	30	39.93	10.07	30

Figure 5.14: Objective function values of specific kinetic energy over iteration number
for a three-material hybrid composite rotor for design cases A and B.

Figure 5.15: Rotational speed over iteration number for a three-material hybrid composite
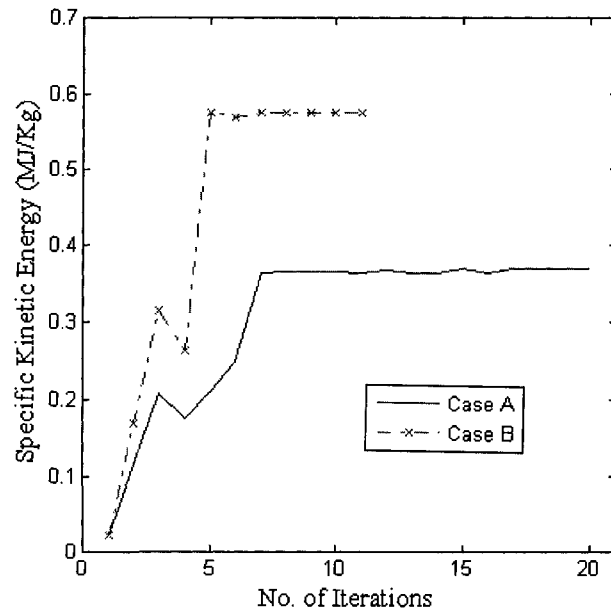rotor for design cases A and case B, from optimization of specific kinetic energy.

Table 5.5: Optimization results for the three-material hybrid composite rotor.

	Optimization of specific kinetic energy		Optimization of kinetic energy per unit cost	
	Rotational speed (RPM)	Specific kinetic energy (MJ/kg)	Rotational speed (RPM)	Kinetic energy per unit cost (kJ/$)
Case A	50,000	0.37	63,407	19.22
Case B	62,500	0.57	65,090	11.48

Choosing kinetic energy per unit cost as the objective function yielded different optimization results for the three-material hybrid composite rotor, see Table 5.5. The evolution of kinetic energy per unit cost and rotational speed with respect to iteration number are shown in Figs.5.16 and 5.17. For design Case A and Case B maximum kinetic energy per unit cost was 19.22 kJ/$ and 11.48 kJ/$ respectively. Corresponding rotational speeds were 63,407 RPM and 65,090 RPM. The final thickness of the AS4-carbon/epoxy rim was 10.1 mm for both design cases, which is close to the minimum limit of 10 mm; the less expensive E-glass/epoxy composite rim of reached a thickness of 59.9 mm and 39.9 mm for design Case A and Case B respectively. This outcome is consistent with the objective of this model (maximizing kinetic energy on a basis of cost). Rotational speeds do not differ dramatically for the two design cases. Yet, due to the greater amount of expensive IM6-carbon/epoxy composite in design Case B, kinetic energy per unit cost was less in this case, i.e. 11.48 kJ/$ compared to 19.22 KJ/$ for Case A. This led to the conclusion that even though cost parameters were merely based on assumption in this study, the optimization model can provide important design information should real material costs be implemented.

It is interesting to note that the outcome of the optimization routine strongly depends on the chosen objective function. For the present three-material rotor the carbon rims reached their maximum thickness when optimizing for specific kinetic energy, whereas the E-glass/epoxy rim reached its maximum allowable thickness when kinetic energy per

unit cost was selected as objective function. When optimizing for specific kinetic energy, best results were obtained for design Case B. The final rotational speed and total kinetic energy were 62,500 RPM and 9.1 MJ respectively. This corresponds to specific energy terms of 0.57 MJ/kg and 7.19 kJ/$. In contrast, design Case A was superior when optimizing for kinetic energy per unit cost. The analysis yielded a higher rotational speed and kinetic energy of 63,407 RPM and 10.55 MJ, corresponding to 0.59 MJ/kg and 19.22 kJ/$. It is particularly interesting that the latter rotor geometry obtained from optimizing kinetic energy per unit cost did not only provide 57% cost savings but also provided 16% more total energy storage capacity than the best rotor geometry obtained from specific kinetic energy optimization. It may be interesting to note that in terms of absolute cost, the optimal rotor configuration represents an absolute cost of $550. Results presented in this section once more confirm that an optimization routine employing cost data may be of great benefit when designing utility-grade flywheel systems.
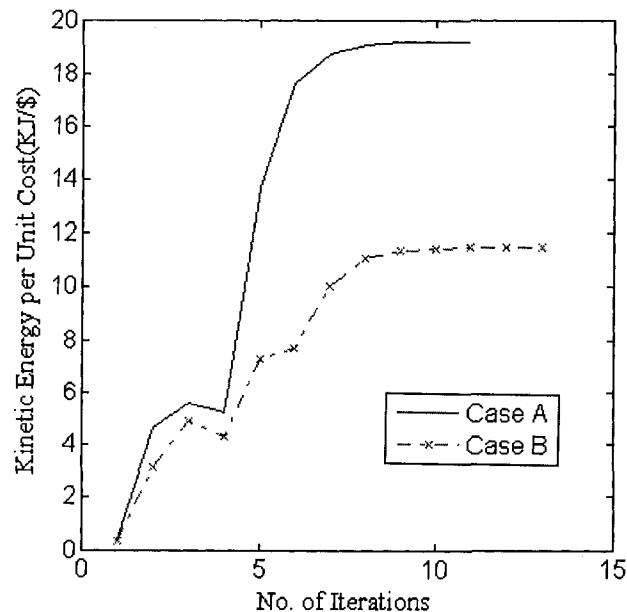
Figure 5.16: Objective function values of kinetic energy per unit cost over iteration number for a three-material hybrid composite rotor for design cases A and B.
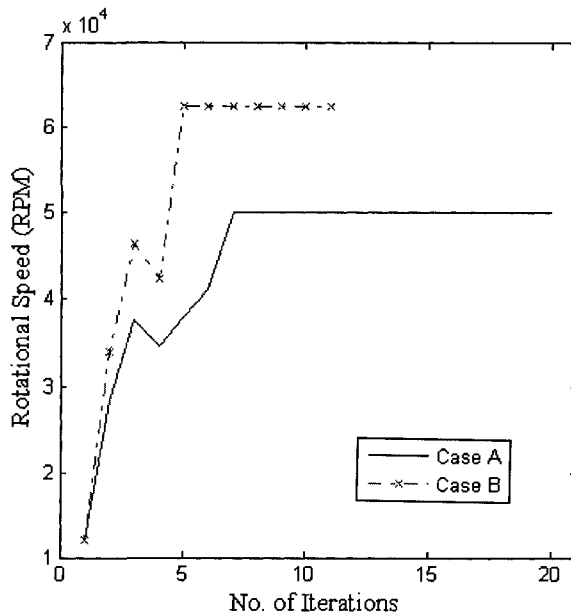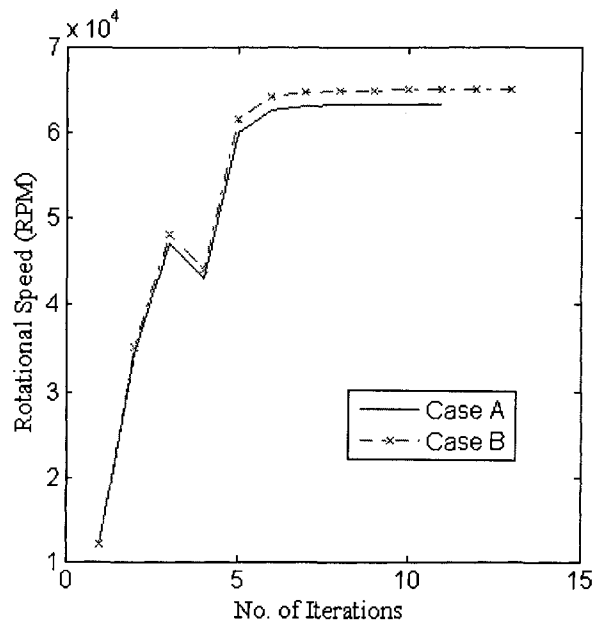
Figure 5.17: Rotational speed over iteration number for a three-material hybrid composite rotor for design cases A and case B, from optimization of kinetic energy per unit cost.

5.4. Comparison of Optimization Results from Three Case Studies

The difference between the best values for specific kinetic energy and kinetic energy per unit cost for the two-materials hybrid rotor (Case Study #1), the two-materials hybrid rotor with interference-fit (Case Study #2), and the three-materials hybrid rotor (Case Study #3) are given in Table 5.6. This table shows that both optimal specific kinetic energy and kinetic energy per unit cost were higher for the two-material hybrid composite rotor with interference-fit assembly than corresponding values for the rotor without press-fit. However, specific kinetic energy as well as kinetic energy per unit cost were significant greater for the three-material hybrid rotor than for the two-material rotors. Using several rims with material of different density and modulus allowed for tailoring the flywheel rotor as to produce less tensile radial stresses during high speed rotation.

Results from preceding case studies show that present numerical optimization routine delivers highly useful information for designing high performance energy storage flywheel rotors. For future analyses the optimization routine may easily be extended to include additional design variables such fiber orientation and rotor and hub diameters.

Table 5.6: Best values for energy-related parameters from Case Studies #1 to #3.

Case Descriptions	Specific kinetic energy (MJ/kg)	Kinetic energy per unit cost (kJ/$)
Two-material hybrid rotor	0.31	9.90
Two-material hybrid rotor with interference-fit	0.35	11.28
Three-material hybrid rotor	0.58	19.22

CHAPTER 6

CONCLUSIONS AND FUTURE WORK

6.1. Conclusions

In the present dissertation the performance of hybrid composite flywheel rotors for energy storage purposes was investigated. The goal of the investigation was to provide a methodology for designing suitable long-term solutions for flywheel rotors for electrical utility applications (e.g. frequency regulation on the electricity grid). The investigation included numerical modeling of single material and hybrid composite flywheel rotors, model validation, and the development of a numerical optimization routine based on the validated models. The objective of the optimization routine was to maximize specific kinetic energy or kinetic energy per unit cost based on a maximum stress criterion.

This thesis also contains a review of the technical literature on composite flywheel rotors, stresses associated with the operation of a flywheel rotor, and different techniques for the reduction of these stresses. Of particular interest in this regard are radial stresses since rotor failure generally occurs due to delamination prior to fiber breakage in the circumferential direction.

A numerical 3-dimensional model was developed for a single isotropic and orthotropic material rotor, and results were compared with the corresponding results from elasticity theory. For both cases, radial and circumferential stresses in the rotor mid plane along the through-thickness direction were compared and found to be in good agreement. Hybrid composite flywheel rotors were subsequently modeled based on the validated single material model. To further corroborate the modeling approach, a five-ring (E-glass/T300/T300/M40J/M40J epoxy matrix composite) flywheel rotor model was developed, and radial and circumferential stresses were compared to corresponding results taken from the literature. Again, good agreement was found for both stress components.

A press fit or thermal residual stress effect was incorporated into the validated hybrid rotor model. It was shown that this may result in significant stress reductions depending

on thermal strains, i.e. the coefficients of thermal expansion of the inner and the outer materials of the flywheel rotor.

A rotor hub from an isotropic material (aluminum) was incorporated into the two-material composite rotor for the performance investigation of a complete flywheel rotor. In addition to the hybrid rim, a hub devoid of any rotor rim was analyzed to observe the behavior of a rotating hub more clearly. In both instances maximum stresses developed adjacent to attachment bores in the hub. Stresses at this location were found to be much higher for the hub and hybrid composite rim assembly. It was concluded that attachment bores in the hub may be critical to safe flywheel operation since failure is likely to originate at these features. Consequently, special attention needs to be given to such features during hub design or manufacture.

Due to the many possible design variables and complex material behavior of FRPC rotors in advanced flywheel systems, numerical analysis was considered a suitable tool for determining optimal geometry and operating conditions. A nonlinear optimization routine was developed based on validated rotor models. The sub-problem approximation method in ANSYS was used to maximize specific kinetic energy or kinetic energy per unit cost, taking into account the geometry of the flywheel rotor and its individual rings, properties and orientations of orthotropic materials, as well as the angular velocity of the flywheel rotor. This numerical optimization routine was run for several test cases.

For two-material rotors with and without press fitted rims it was found that rotor geometries optimized for kinetic energy per unit cost yielded 71% cost savings, while only providing 24% less total energy stored, than rotor geometries optimized for specific kinetic energy. For comparison, the analysis for a single rim glass/epoxy rotor yielded cost savings of only about 5% while providing 47% less energy stored compared to a hybrid glass/carbon flywheel rotor.

By using three-material hybrid flywheel rotors, much higher energy storage capacity was achieved than for two-material rotors. When optimizing for kinetic energy per unit cost the rotor geometry yielded 57% cost savings, while also providing 16% more total energy stored than the rotor geometry optimized for maximum kinetic energy per unit mass. Stresses in the rotor, especially radial stress, can significantly be reduced by fabricating

the rotor from multiple rings. Even though cost data were taken by assumption in this study, the usefulness of this optimization model was clearly demonstrated.

At present, flywheel energy storage systems are challenged to compete on a cost basis with chemical battery systems in part due to the high cost of advanced materials. The goal of this thesis was to evaluate the presented modeling and optimization approach. It was ascertained that such a methodology may help flywheel manufacturers to produce more cost effective and reliable flywheel rotors for energy storage and power conditioning applications. The work demonstrated that by using hybrid composite flywheel rotors, energy storage capacity can be increased while material cost can be decreased for utility grade applications.

6.2. Future Work

The work presented in this thesis offers areas of continuing research in the field of design and analysis of composite flywheel rotors for energy storage purposes. Some possible areas of future work are listed below:

- The present optimization model considered only linear elastic material behaviour. Incorporating aspects of material non-linearities such as visco-elasticy may be an important aspect for further research. Creep may adversely affect long-term performance of polymer-based composite rotors, and hence it is necessary to investigate creep effects on the performance of the hybrid composite rotors.

- The effect of delamination or fracture in composite rotors was not investigated in this research. It would be desirable to investigate crack propagation behavior in flywheel rotors to establish procedures for safe operation.

- Only two design variables were considered at any given case in this optimization model, which was developed using the ANSYS sub-problem approximation method. Further investigations can be performed with this optimization model allowing for more design variables. This will enable the optimization of rotors with more than three rims, which may maximize kinetic energy or decrease cost even further.

- Design optimization should be performed incorporating an appropriate hub geometry with the rim. To investigate the performance of a full flywheel rotor, greater

attention must be paid to the hub design. As shown above, improper hub design may result in hub failure or adverse effects on the composite rim due to high bending stresses.

BIBILIOGRAPHY

1. ANSYS, Documentation, Release 11.0, ANSYS Inc.

2. Arfken, G. (1985). Mathematical Methods for Physicists, Third edition. Orlando, Fl: Academic Press

3. Arnold, S.M., Saleeb, A.F., Al-Zoubi, N.R. (2002). Deformation and life analysis of composite flywheel disk systems. Composites: Part B, Vol. 33, 433-459.

4. Arvin, A.C., Bakis, C.E. (2006). Optimal design of press-fitted filament wound composite flywheel rotors. Composite Structures, Vol. 72, 47-57.

5. Aziz, A.A., Baaklini, G.Y., Trudell, J. (2001). An integrated NDE and FEM characterization of composite rotors. NASA Report No. TM 2001-210473.

6. Bitterly, J.G. (1998). Flywheel technology: past, present, and 21st century projections. IEEE Aerospace and Electronic Systems Magazine, Vol. 13, No. 8, 13-16.

7. Budgell, P. (1998). Finite Element Analysis and Optimization Introduction. Retrieved July 8, 2008, from www3.sympatico.ca/peter_budgell/FEA_intro.html.

8. Cook, R.D. (1995). Finite Element Modeling for Stress Analysis. John Wiley & Sons, New York.

9. Daniel, I.M., Ishai, O. (2006). Engineering Mechanics of Composite Materials. Oxford University Press, New York.

10. DeTeresa, S.J., Groves, S.E. (2001). Properties of Fiber Composites for Advanced Flywheel Energy Storage Devices. Proc. 46th International SAMPE Symposium and Exhibition, Vol.46, 1643-1656.

11. Eby, D., Averill, R.C., Punch, W.F., Goodman, E.D. (1999). Optimal design of flywheels using an injection island genetic algorithm. Artificial Intelligence for Engineering Design, Analysis and Manufacturing, Vol. 13, No. 5, 327-340.

12. Flanagan, R.C., Wong, J.J. (1989). Energy storage rotor with flexible rim hub. United States Patent, No. 4,860,611.

13. Gabrys, C.W. (2003). Press-fit multi-ring composite flywheel rim. United States Patent, No. 6,508,145.

14. Geneta, G. (1985). Kinetic Energy Storage - Theory and Practice of Advanced Flywheel Systems. Butterworths & Co., London, UK.

15. Gigliotti, M., Wisnom, M.R., Potter, K.D. (2003). Development of curvature during the cure of AS4/8552[0/90] unsymmetric composite plates. Composites Science and Technology, Vol. 63, 187-197.

16. Gowayed, Y., Hady, F.A., Flowers, G.T., Trudell, J.J. (2002). Optimal design of multi-direction composite flywheel rotors. Polymer Composites, Vol. 23, No. 3.

17. Grudkowski, T.W., Dennis, A.J., Meyer, T.G., Wawrzonek, P.H. (1995). Flywheels for energy storage. Proc. 27th International SAMPE Technical Conference, Vol.27, 760-768.

18. Ha, S.K., Kim, D.J. (1999a). Optimal design of hybrid composite flywheel rotor using finite element methods. In: Proc. 44th International SAMPE Symposium, Vol.2, 2119-2132.

19. Ha, S.K., Yang, H.I., Kim, D.J. (1999b). Optimal design of a hybrid composite flywheel with a permanent magnet rotor. Journal of Composite Materials, Vol. 33, No. 16.

20. Ha, S.K., Kim, D.J., Sung, T.H. (2001). Optimal design of multi-ring composite flywheel rotor using a modified generalized plane strain assumption. International Journal of Mechanical Sciences, Vol. 43, 993-1007.

21. Ha, S.K., Han, H.H., Han, Y.H. (2008). Design and manufacture of a composite flywheel press-fit multi-rim rotor. Journal of Reinforced Plastics and Composites, Vol. 27, No. 9. 953-965.

22. Haftka, R.T., Gurdal, Z. (1992). Elements of Structural Optimization. 3rd Edition. Kluwer Academic Publishers.

23. Hebner, R., Beno, J., Walls, A. (2002). Flywheel batteries come around again. IEEE Spectrum, April 2002, 46-51.

24. Hellmold, A. (2001). Potter's Wheel, Egypt, 2400 BCE. Smith College Museum of Ancient Inventions. Retrieved June 20, 2008, from www.smith.edu/hsc/museum/ancient_inventions/potterwheel2.html.

25. Huang, B.C. (1999). Polar woven flywheel rim design. Proc. Of International SAMPE Symposium, Vol. 44, No. 2, 2133-2144.

26. Huang, J., Fadel, G.M. (2000). Heterogeneous flywheel modeling and optimization. Materials and Designs, Vol. 21, 111-125.

27. Kaw, A.K. (2005). Mechanics of composite materials. CRC Press, Boca Raton.

28. Kim, S.S., Lee, D.G. (2006). Design of the hybrid composite journal bearing assembled by interference fit. Composite Structures, Vol. 75, 222-230.

29. Lazarewicz, M.L., Rojas, A., (2006). Grid frequency regulation by recycling electrical energy in flywheels, Proc. IEEE PES General Meeting, Denver (CO), USA, June 6-9, 2006.

30. Lekhnitskii, S.G. (1968). Anisotropic Plates. Gordon & Breach Science Publishing, New York.

31. Logan, D.L. (1993). A first course in the finite element method. PWS Publishing Company, Boston.

32. Mueller, G., Tiefenthaler, P., Imgrund, M. (1994). Design optimization with the finite element program ANSYS. International Journal of Computer Applications in Technology, Vol. 7, No. 3-6, 271-277.

33. Pelletier, J.L., Vel, S.S. (2006). Multi-objective optimization of fiber reinforced composite laminates for strength, stiffness and minimal mass. Computer and Structures, Vol. 84, 2065-2080.

34. Pentadyne Voltage Support Solution (2007). Theory of operation. Retrieved June 20, 2008, from www.pentadyne.com/uploads/18/File/Theory-of-Operation.pdf

35. Ranter, J.K.H., Chang, J.B., Christopher, D.A. (2003). Composite flywheel rotor technology. In: A Review. Composite Materials: Testing and Design, Vol. 14, ASTM STP 1436 (Bakis, C.E., Ed.), ASTM International, West Conshohocken, PA.

36. Reedy, E.D., Street, H.K. (1979). Composite-rim flywheels: spin tests. SAMPE Quarterly, Vol. 10, No. 3, 36-41.

37. Rupnowski, P., Gentz, M., Sutter, J.K., Kumosa, M. (2005). An evaluation of the elastic properties and thermal expansion coefficients of medium and high modulus graphite fibers. Composites: Part A 36, 327-338.

38. Saleeb, A.F., Arnold, S.M., Al-Zoubi, N.R. (2003). A Study of time-dependent and anisotropic effects on the deformation response of two flywheel designs. NASA/TM-2003-212091.

39. Takahashi, K., Kitade, S., Morita, H. (2002). Advanced Composite Materials, Vol.11, No. 1, 41-50.

40. Tzeng, J.T. (2003). Viscoelastic analysis of composite rotor for pulsed power applications. IEEE Transactions on Magnets, Vol. 39, No.1.

41. Tzeng, J., Emerson, R., Moy, P. (2005). Composite flywheel development for energy storage. Army Research Laboratory, ARL-TR-3388.

42. Ugural, A.C., Fenster, S.K. (1995). Advanced Strength and Applied Elasticity, 3rd Edition. Prentice Hall, Upper Saddle River, New Jersey.

43. Wagner, H.D. (2007). Retrieved July 14, 2008, from Lectures on composite materials. http://www.weizmann.ac.il/wagner/COURSES/.

44. Winston, L.W. (2004). Operation Research: Applications and Algorithms. Fourth Edition, Thomson Learning, Belmont, CA.